UNIVERSITY OF SOUTHAMPTON

FACULTY OF PHYSICAL SCIENCES AND ENGINEERING

School of Electronics and Computer Science

A 2-D micro-magnetic neuro-stimulation platform

by

Maria Eleni Rizou

Thesis for the degree of Doctor of Philosophy

November 2018

UNIVERSITY OF SOUTHAMPTON

ABSTRACT

FACULTY OF PHYSICAL SCIENCES AND ENGINEERING

School of Electronics and Computer Science

Thesis for the degree of Doctor of Philosophy

A 2-D MICRO-MAGNETIC NEURO-STIMULATION PLATFORM

Maria Eleni Rizou

The aim of this thesis is the development of a novel in-vitro neuro-stimulation tool based on the micro-scale implementation of the transcranial magnetic stimulation (TMS) principle. The project involves the design, fabrication and testing of single coil geometries and a two dimensional array of micro-coils for establishing spatio-temporal magnetic flux profiles. The proposed device can induce a localised electric field in the vicinity of the coils that can instigate the stimulation of single or multiple neurons in vitro. The first steps of this project covered the investigation of all the parameters that affect the efficiency of a micro-coil structure, in an attempt to achieve an induced electric field above the stimulation threshold of a neuron (e.g. spatial derivative electric field intensity: $\partial E_x/\partial x > 11kV/m^2$ [1]). The investigation is based on a parametric study with COMSOL Multiphysics simulation software, while for the design of the structure further experimental limitations were taken into account. The fabrication steps for the development of the micro-coils include two photolithographic steps while the further increase of micro-coils' thickness was achieved with electroplating. The packaging, the bio-compatible encapsulation with Parylene-C and the functionalization of the material, in terms of hydrophilicity, are also presented and complete the platform prototyping. The micro-coils are characterized electrically with an impedance frequency sweep while a further monitoring of their electromagnetic behaviour was performed with magnetic nanoparticles trapping and inductive measurements between different coils in the same array. Their ability to stimulate magnetically neural cells was evaluated firstly with a phantom gel with electric properties (electrical permittivity and conductivity) similar to neural tissue, with the use of bio-oriented simulations with NEURON software + COMSOL and with biological validation in vitro. Finally, the main challenge of this method is to define the limits of safe operation of the micro-inductors prior to their failure due to Joule heating and electromigration phenomena. In this direction, an electrothermal study was performed to define the maximum current capacity that could safely hold.

Table of Contents

List of Figures

List of Tables

Declaration of Authorship

I, Maria Eleni Rizou declare that this thesis and the work presented in it are my own and has been generated by me as the result of my own original research.

A 2-D micro-magnetic neuro-stimulation platform

I confirm that:

1. This work was done wholly or mainly while in candidature for a research degree at this University;

2. Where any part of this thesis has previously been submitted for a degree or any other qualification at this University or any other institution, this has been clearly stated;

3. Where I have consulted the published work of others, this is always clearly attributed;

4. Where I have quoted from the work of others, the source is always given. With the exception of such quotations, this thesis is entirely my own work;

5. I have acknowledged all main sources of help;

6. Where the thesis is based on work done by myself jointly with others, I have made clear exactly what was done by others and what I have contributed myself;
   - The PCB for the biasing of each micro-inductor in a packaged device (presented in figure 5.9) was designed in collaboration with Dr. K. Papadimitriou.
   - The biocompatibility of the devices and the biological experiments were performed in collaboration with biologists from the NeuroChip Laboratory in the University of Padova. In more detail, samples fabricated by me in University of Southampton were posted to NeuroChip Laboratory of Professor S. Vassanelli, where Dr. M. Maschietto observed the viability of hippocampi neural cell cultures in order to assess the biocompatibility of the samples. The biological experiments were also performed in the University of Padova. Prior to the start of the experiment, samples were cultured with hippocampi neural cells by Dr. M. Maschietto. Dr. C.Cecchetto performed the patch clamping of the neural cells. I joined the biological experiment to control the electronic part of the

setup. We all participated in discussions, together with Professor Vassanelli, related to important parameters of the biological experiment and decided on the activation protocols which had to be tested for the specific type of cells. A more detailed description of the biological experiment is presented in chapter 8.

7. Parts of this work have been published as listed in Appendix 1.

Signed: ....

Date: ....

Acknowledgments

I would like to thank all the people who supported this work. My supervisor Themis Prodromakis for giving me the opportunity to work on this inspiring topic. Many thanks to Dr. Ali Khiat for all his useful advice on the fabrication procedure, Dr. Tatiana Trantidou and Ilaria Sanzari for giving me useful information on the biological parameters of the project at the beginning of this research study. Dr. Kostas Papadimitriou for helping me in the design of the PCB packages. A big thank you to the members of the group (present or past) for the fruitful discussions which improved the quality of my work. I would also like to acknowledge the work of Mike Perry in the Cleanroom. His immediate action on technical issues I faced and his efficiency in finding solutions improved significantly our quality of life in the lab! I am grateful to the University of Southampton for giving me the opportunity to interact with undergraduate students through lab sessions and demonstrating work, which improved my scientific understanding and teaching skills through the years.

Regarding our collaborations, special thanks to Prof. Stefano Vassanelli (NeuroChip Lab, University of Padova), Dr. Marta Maschietto for performing the cell culturing of neural cells on the samples and Dr. Claudia Cecchetto for her expertise in patch clamping the cells during the bio-experiment. I am thankful for the very good collaboration and interaction we had, despite the difficulties we faced. I would also like to thank Prof. Cesare Terracciano (Faculty of Medicine, Hammersmith Hospital, Imperial College London) for his encouraging attitude in our short collaboration.

I would like to gratefully acknowledge the financial support of A.G.Leventis foundation.

Finally, I would like to express my gratitude to my family and friends for their support and encouragement. My sister for her willingness to help on all the difficulties I faced, despite her totally different field of knowledge, and Artemis for being there at all times to share all this experience.

List of Acronyms

CMOS	Complementary metal-oxide semiconductor
DIV	Days in vitro
DUT	Device under test
FEM	Finite element method
GUI	Graphical user interface
ICP	Inductively coupled plasma (etching)
LOC	Lab on a chip
MEA	Micro-electrode array
MEMS	Microelectromechanical systems
MMW	Millimetre wave
MRI	Magnetic resonance imaging
MTF	Median time to fail
NMR	Nuclear magnetic resonance
NRVM	Neonatal rat ventricular myocytes
PCB	Printed circuit board
PDMS	Polydimethylsiloxane
PNS	Peripheral nervous system
RF	Radiofrequency
RIE	Reactive ion etching
SEM	Scanning electron microscope
TMS	Transcranial magnetic stimulation
VLSI	Very-large-scale integration

Chapter 1

Introduction

1.1 Background and motivation

Neural stimulation has been proposed in literature through a number of different methods both for in vitro and in vivo purposes. The most well established and straightforward method of neural stimulation is the electrical stimulation, where an electrode has to be in direct contact with the neural tissue or cell medium. The main disadvantage of electrical stimulation has to do with degradation phenomena which appear in the electrode-electrolyte interface. Similarly, other methods of neural cell stimulation have been proposed, amongst which is the optical and thermal stimulation, each of which with specific advantages and disadvantages discussed in more detail in chapter 2.

Magnetic stimulation, which is the main interest of this study, has recently attracted significant attention, as it could serve as an alternative method for exciting neural activity both in vitro [2], [3] and in vivo [4], [5]. Magnetic stimulation has been used macroscopically in the brain to elicit neuronal activity in a contactless manner. The method is known as transcranial magnetic stimulation (TMS) and is nowadays used clinically to treat specific medical conditions [6], [7]. The basic principle of method is based on Faraday's law of induction. A time evolving current flows through an inductor and induces an electrical field, which stimulates the brain tissue of interest. This electric field induced and not the magnetic field, is the actual stimulus and this is why this method could be more accurately described as an indirect electrical stimulation. As it is clear, magnetic stimulation now overcomes the main disadvantage of electrical stimulation, namely the need of direct contact between the electrode and the neural tissue.

Recently the need of scaling down the size of the electromagnets is coming rapidly into the foreground in the field of magnetic stimulation applications. In vitro, decreasing the size of the inductors is translated into high spatial resolution and selectivity. At the same time, similar devices transferred to flexible substrates, could be used in vivo, serving the constantly growing need for devices implanted into living tissue. The miniaturisation of TMS in vivo could overcome a series of problems, such as the electrode corrosion, biofouling phenomena and electrode electrolyte interface problems. At the same time it could broaden the limits of existing stimulation techniques and medical knowledge. The idea of this project is not only to adopt the neuro-stimulating method of TMS to the micro-meter scale, but also to develop a planar array of micro-coils to achieve spatio-temporal control of magnetic flux profiles and demonstrate cell stimulation in vitro.

In brief,

- The proposed approach intends to address issues such as biocompatibility, electrode corrosion, non-specific stimulation and low penetration depth in tissue that existing techniques of neural stimulations are suffering from.
- A possible implantable future application of this method could be used, bringing the idea of electroceuticals [8] one step closer to reality. The proposed idea could enable the non-invasive stimulation and observation of neural networks making connections between brain activity and certain diseases and behaviours. This could be translated into a 'dictionary of patterns' which associates a specific health/disease state to its treatment.
- In a future extension, applications in the same direction as the one proposed here would lead to the broadening of our medical knowledge on the underlying mechanisms of neurological diseases, such as Parkinson, Alzheimer, Schizophrenia and depression. In other words, there is also a long term impact on the society since health and quality of life could be improved in an increasing number of people suffering from these diseases.

To achieve this vision, several challenges have been addressed. From the engineering point of view, an increase in the amplitude of the current forced through an inductor leads to a stronger induced electric field in the vicinity of the cell which could make magnetic stimulation of neural cells easier. On the other hand, an unreasonable increase of the applied current through the micro-coils might lead to their failure, due to both Joule heating and electromigration phenomena. Therefore, there must be a balance between the dimensions of the micro-coils and the applied current, in order to achieve neural stimulation by the less possible micro-coil dimensions. From the biological point of view, the question is whether the micro-coil would be able to excite a neural cell. Biology related challenges range from bio-compatibility and cell viability issues of the proposed device, to the identification of successful protocols of cell activation, which is an almost totally unexplored area for micro-magnetic stimulation.

1.2 Aim

The aim of this thesis is the development of a novel in-vitro neuro-stimulation tool based on the micro-scale implementation of the TMS principle. The final device could serve as the magnetic equivalent of microelectrode arrays. The design, fabrication and characterization of a micro-scale array of electromagnets for biomedical application is presented from the engineering perspective. Final goal of this thesis is the use pf the final prototype for the biological validation of magnetic stimulation in vitro.

1.3 Thesis objectives

The main research objectives of this project include the following stages:

1) Design and fabrication of micro-inductors in a wafer level using standard micro-fabrication techniques. This step includes the electrical benchmarking of the prototypes with through electromagnetic characterisation and simulation studies.
2) Development of micro-coil arrays for the magnetic stimulation of neural populations. This stage involves the bio-compatible packaging required for the biological testing. This step includes the design of control electronics for the activation of the device and finally the validation of magnetic stimulation in neurons based on bio-oriented simulations, biorelistic testing and the actual bioexperiment.
3) Testing and characterization of the samples to produce a reliable prototype and overcome arising limitations. This step includes the choice of fabrication methods (e.g. need for electroplating), the choice of the appropriate bio-inert materials for a bio-compatible packaging. In this direction, the identification of limitations related to thermal deterioration phenomena and electromigration is important and leads to further electrothermal studies, which define a non-destructive operating regime for the fabricated prototypes.

1.4 Structure of thesis

The structure of this thesis is detailed below.

Chapter 1: Introduction

This chapter presents the motivation behind the development of a planar micro-magnetic array for neural stimulation. It also contains the aim and the objectives of the project.

Chapter 2: Biological overview and neural stimulation techniques

This chapter introduces the fundamental biology related to cell activation and gives a clear framework of the bio-physical problem. At a second level, it gives the background on alternative neural stimulation techniques (electrical, optical, thermal).

Chapter 3: Magnetic stimulation and state-of-the-art technologies

This chapter focuses on magnetic stimulation starting from the macroscopical TMS clinical method. The miniaturization of TMS is further presented by highlighting the work of different scientific groups, in order to give all the important to-date knowledge on micro-magnetic stimulation. It finally includes the state-of-the-art technologies and fabrication methods of micro-scale inductors on wafers.

Chapter 4: Simulations and design

This chapter focuses on simulations with COMSOL Multiphysics software in order to study the expected electromagnetic behaviour of the inductors. A parametric and an electrthermal model are developed to observe how different parameters (geometric and experimental) affect the efficiency of the proposed geometries. Finally, design considerations and the preparation of the photolithographic mask are also discussed.

Chapter 5: Microfabrication of inductors and platform prototyping

This chapter presents is detail the fabrication procedure of the micro-inductor arrays. It also contains the steps towards the completion of the final bio-compatible neuro-stimulating platform.

Chapter 6: Electromagnetic and electrothermal benchmarking

The electrical characterization of the fabricated devices is the main focus of this chapter, supported by FEM simulations with COMSOL Multiphysics software [9]. In addition, an electrothermal study is performed to identify the deterioration of the devices due to Joule heating and electromigration phenomena.

Chapter 7: Biorealistic simulations and testing

This chapter focuses on bio-realistic methods used to validate the efficiency of the devices. Firstly, a combination of an open code simulation environment (NEURON simulation environment [10]) and COMSOL Multiphysics is used to perform numerical simulations in an simplified cell geometry. Secondly, the idea of using a phantom solution to imitate the electrical properties of neural tissue is introduced. Description of the composed phantom gel, its electric characterisation and finally its use in an experimental setup to measure inductive current due to the micro-coils' activation are presented.

Chapter 8: Functionality of the micro-fabricated arrays

In this chapter, applications testing the functionality of the fabricated prototypes are presented. Magnetic nanoparticle trapping is initially used to demonstrate the successful magnetic behaviour of the micro-arrays. The observations from the magnetic nanoparticles experiment are further supported with inductive measurements in order to quantify the interaction between adjacent micro-coils in an array. Finally a full description of all stages of the bio-experiment is presented, starting from the cell culturing to the actual attempts of magnetic stimulation in vitro.

Chapter 9: Conclusions and future work

The final chapter of the thesis gives a brief summary of the accomplished work, highlights the contributions of this thesis and mentions the possible future directions of this study.

Chapter 2

Biological overview and neural stimulation techniques

The starting point of this thesis is the shaping of a clear framework regarding the biological phenomenon of cell stimulation. A deep understanding on the electrophysiological problem is crucial due to the interdisciplinary nature of the work. This chapter provides a basic introduction to the aspects of neural physiology, emphasising on the functionality of a nerve cell and on important structural properties at the cellular level. Furthermore, a thorough discussion about neural stimulation methods and techniques is presented, highlighting the state-of-the-art methodologies (apart from magnetic stimulation which is described in detail in chapter 3) to achieve stimulation of neural populations both in vitro and in vivo.

2.1 The biology of nerve cell

This section is an introduction to the basic biological principles and function of a nerve cell. As shown in figure 2.1, the main parts of the nerve cell could be synoptically divided on three main parts:

- The cell body, the *soma* which includes the nucleus of the cell.
- The short processes of the soma, the *dendrides* which receive signal from other cells and transfer it to the cell body.
- The single long nerve fibre, the *axon* which transfers the signal from the cell body to another cell or a muscle. The axon might be covered with an insulating layer called *myelin sheath*, which guarantees the faster propagation of the electric signal.

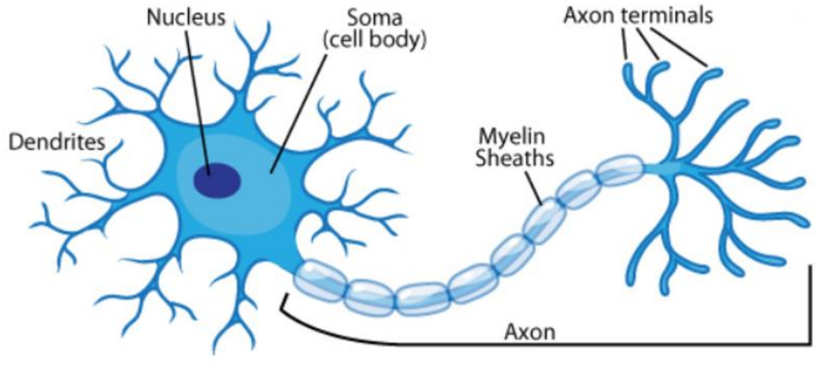

Fig. 2. 1 The main parts of a nerve cell [11]

The nerve cell is enclosed by a *cell membrane* with a thickness of 7.5-10nm. On this membrane there are some macromolecular pores, the *ionic channels*, through which sodium, potassium and chloride ions are flowing inside-out the cell. The flow of these ions forms the basis of all the bioelectric phenomena.

The membrane voltage V_m, is defined by the presence of sodium and potassium ions on the outside space of the cell and inside it. $V_m = V_i - V_o$, where the V_i is the potential of the inner membrane surface and V_o the potential of the outer membrane surface. Fluctuations of membrane potential could be classified according to Theodore Holmes Bullock [12] into a *resting potential* and potential fluctuation due to activity. The membrane voltage changes connected to activity could be further divided to three different types [13]:

1. *Pacemaker potentials*, which describe all the intrinsic activity of the neuron cell which occur without external activation.
2. *Transducer potential* across the membrane, due to external events. These include both *generator potentials*, caused by receptors and *synaptic potentials*, caused by synapses and are either inhibitor or excitatory.
3. The resulting potentials of a transducer potential. If the magnitude of the excitation does not exceed a threshold, the respond will be non-propagating. If the response is higher than the threshold, an *action potential* impulse will be propagating unattenuated along the axon fibre.

The existence of a resting potential in a membrane could be equivalently described by saying that the membrane is *polarized*. By reducing the membrane potential, then the membrane becomes *depolarized* (excitatory potential), while if by increasing it (i.e. by making it more negative), then the membrane becomes *hyperpolarized* (inhibitory potential).

2.2 Excitability of the nerve cell

The membrane of the cell is the most basic element that regulates the signalling of excitable cells, important for the propagation of information along the cell and the communication between the cells. Charge separation is used by the cells to store energy in a system. There are numerous mechanisms which control and establish charge separation across the membrane.

The value of the transmembrane potential depends on the constant movement of the ion populations and could be disrupted due to an electrical, chemical or mechanical stimulus.

From a physical point of view there is an analogy between a bio-physical system and an electric equivalent circuit. The idea is that the combined electrochemical properties of the lipid bilayer, pumps and channels can be described as an equivalent system comprising of voltage-dependent resistors, batteries and capacitors.

2.2.1 The membrane at equilibrium - Nernst equation

There are two types of forces acting on every ion, which determine their movements across the membrane. The one is the electric force, F_{φ}, due to the potential difference between the intracellular and extracellular areas. The other is the chemical force, F_c, due to differences in the ionic concentrations across the membrane. The diffusion of the ions down to their concentration gradient can be though as a response to the driving form which maximizes the entropy of the system. The electric force is acting on every charged ion, while the chemical force is acting only on a single type of ions. The ionic current I_{ion}, as shown in equation (2.1) is written as a summation two current components, each of which arises from the two different mechanisms [14], where I_{φ} is given by Ohm's law in equation (2.2) and I_c by Fick's law in equation (2.3). In equation (2.3), D is the diffusion coefficient and C the ionic concentration. Equilibrium is reached, when these two effects balance and I_{ion}=0.

$$I_{ion} = I_{\varphi} + I_c \tag{2.1}$$

$$I_{\varphi} = \frac{V_m}{R_m} = \frac{V_i - V_e}{R_m} \tag{2.2}$$

$$I_c = -D\frac{\partial C}{\partial x} \tag{2.3}$$

Assuming a case where an ion has to move between two areas, one in voltage V_1 and concentration c_1 and the other in voltage V_2 and concentration c_2. Areas 1 and 2 represent the extracellular and intracellular space. In equilibrium one could calculate the probability p_i of finding the ion in each area by applying the Boltzmann distribution, and then further calculate the ratio of the two probabilities as in equation (2.4). The ratio of the two probabilities represents the ratio of ionic concentrations c_i in the two areas. In equation (2.4), the energy is the electrical energy felt by the ion because of the voltage V_i in each area, k is the Boltzmann constant, Z the ion valence and T the temperature.

$$\frac{p_1}{p_2} = \frac{c_1}{c_2} = \frac{e^{-\frac{ZeV_1}{kT}}}{e^{-\frac{ZeV_2}{kT}}} \tag{2.4}$$

This equation relates the difference of the electrical potential to the ratio of concentration of ions and is known as the Nernst equation, while is usually written in the form of equation (2.5), where e the charge of an electron.

$$V_m = V_2 - V_1 = \frac{kT}{Ze} \ln\left(\frac{c_1}{c_2}\right) \tag{2.5}$$

In terms of an electric equivalent circuit, the membrane could be considered as a capacitor in parallel with a resistor and a battery, as illustrated in figure 2.2. The difference between the membrane potential and the Nernst potential for the ionic population, leads to a current across the cell membrane, described by equation (2.6).

$$I_{ion} = \frac{1}{R_m}(V_m - V_{Nerst}) = G_m(V_m - V_{Nernst}) \tag{2.6}$$

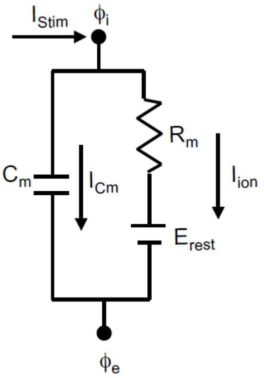

Fig. 2. 2 The electric equivalent of a section of the cell membrane [14].

In reality, the cell functionality is determined by more than one type of ions, each of which with different ability to cross the membrane. A better approximation of the equilibrium potential is given by the Goldman-Hodgkin-Katz equation (2.7) and includes the three major ions involved in the phenomenon: sodium Na^+, potassium K^+ and chlorine Cl^-. P_i terms describe the relative permeability of each ion. In the following sections it will be demonstrated that cells use mechanisms in order to maintain a non-equilibrium charge state and that ions dynamically move across the membrane.

$$V_m^{eq} = \frac{kT}{e} \ln\left(\frac{P_K[K^+]_e + P_{Na}[Na^+]_e + P_{Cl}[Cl^-]_i}{P_K[K^+]_i + P_{Na}[Na^+]_i + P_{Cl}[Cl^-]_e} \right) \tag{2.7}$$

2.2.2 Hodgkin and Huxley channels

The first physiologically accurate nonlinear model of ionic current was published in 1952 by Hodgkin and Huxley and despite its relative simplicity, based on a number of assumptions, it remains a well-known standard model for membrane excitability [15]. Their first assumption was that the ionic current consists of a set of different currents, as expressed in equation (2.8).

$$I_{ion} = I_{cm} + I_{Na} + I_K + I_L \tag{2.8}$$

Where I_{cm} represents the capacitive current resulting from the natural capacitance of the cell membrane and is described by equation (2.9). I_{Na} and I_K are the currents of sodium and potassium ions respectively, while I_L is a leakage current. Experiments showed that I_L is a linear leakage current in contrast to I_{Na} and I_K that are non-linear. Equation (2.10) describes the electric equivalent relation for the leakage current, with G_L representing the leakage conductance and V_L^{Nernst} the Nernst potential.

$$I_{cm} = C_m \frac{dV_m}{dt} \tag{2.9}$$

$$I_L = G_L \left[V_m - V_L^{Nernst} \right] \tag{2.10}$$

Similarly, the non-linear current is described by the non-linear version of equation (2.11).

$$I_{nl} = G_{nl}(V_m)\left[V_m - V_{nl}^{Nernst} \right] \tag{2.11}$$

The conductivity of the cell membrane shows a dependence on the transmembrane potential, denoting the natural feedback loop governing the relationship between I_{ion} and V_m. The electric equivalent circuit is presented in figure 2.3.

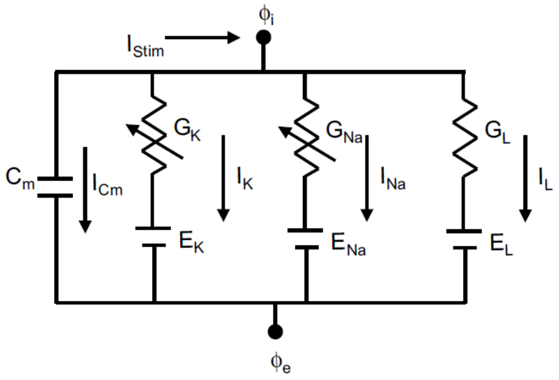

Fig. 2. 3 The Hodgkin-Huxley electric circuit equivalent [14]**.**

To complete the full picture of how signal propagates along a cell, the model needs to employ some statistics regarding the gating of ions through the channels, since in every part of the membrane there are millions of channels. Each channel has three possible states: open, closed or inactive. The probability of each state changes with time and depends on the voltage conditions on the membrane. If a charge stimulus applied to the cell membrane raises the membrane voltage above a threshold of around -40mV, the membrane potential rapidly goes up to a value roughly given by the Nernst potential of sodium at +40mV. Just as quickly the potential drops and overshoots to -90mV and finally the resting potential value of -70mV is re-established. This sharp increase of the membrane potential of a patch of membrane raises the membrane potential of a nearby patch above threshold, leading to its depolarization, which in turn depolarizes the next patch, and so on, leading to the action potential propagation. The resulting propagating electric signal is usually described as a Hodgkin-Huxley action potential, or simply an action potential. Figure 2.4 summarises the formation of an action potential, while the different phases of cell activation are clearly illustrated:

- Phase 1: Rest
- Phase 2-3: Activation and Depolarisation
- Phase 4: Repolarisation and Hyperpolarisation

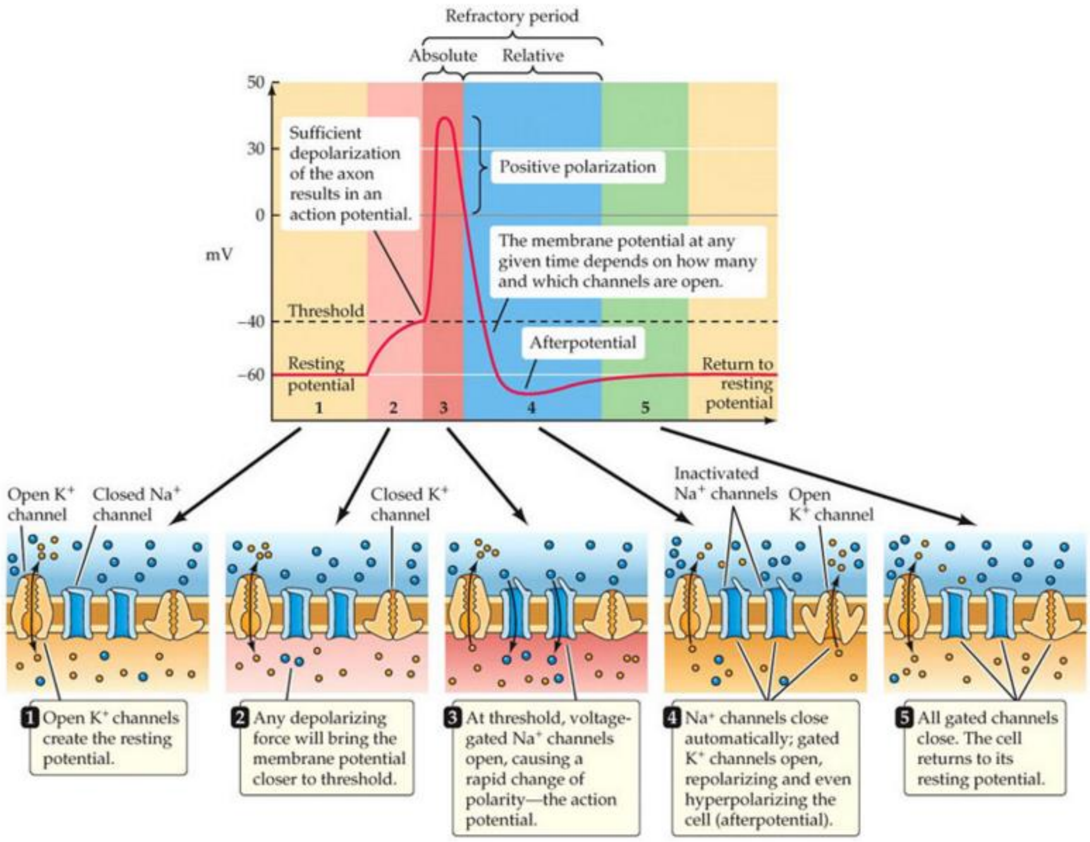

Fig. 2. 4 Illustration of the formation of an action potential after stimulation, along with the behaviour of the selectively permeable ion channels in a patch of a membrane [16]**.**

2.2.3 Strength-duration relationship

An important aspect of the excitability of a cell is related to the characteristics of the stimulus. Activation of a cell is achieved when sufficient amount of energy is offered to the system and the transmembrane potential reaches a specific threshold value V_m^{th}. More specifically, electrophysiological experiments on different cell types show that there is an interplay between the strength and the duration of the stimulus, which could be graphically represented by the well-known strength-duration plot [6]. Figure 2.5a shows examples of cellular response to various stimuli, while 2.5b gives an example of the strength-duration plot, through which one can extract useful information for the excitability of a cell. If the stimulus current is relatively small and the transmembrane voltage reaches a steady state (V_∞) at a value below the threshold, then the membrane charges but an action potential is not produced. Increasing further the I_s, would result in quicker reaching of the threshold voltage V_m^{th}. However even if $V_\infty > V_m^{th}$, the stimulus might be on for such a short time that the membrane would not have time to reach the threshold and this explains the asymptotic behaviour on the I_s axon.

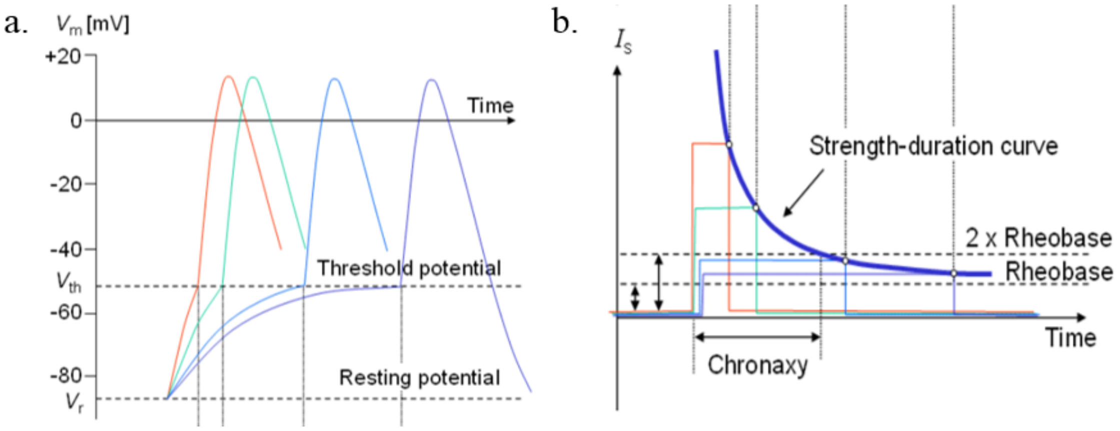

Fig. 2. 5 Examples of (a) response of the membrane to various stimuli of changing strength. (b) strength-duration curve [6].

Important characteristics of cell excitability, defined by the strength-duration graph are the rheobase and the chronaxie of a cell. Rheobase is defined as the minimum current amplitude (I_s) which is required to bring the membrane to the threshold of activation. The strength-duration relation shows that this is expected to happen for a very long or infinite stimulus duration (d). The limit of rheobase (I_{rhe}) is described by the asymptote on the time axis on the strength-duration graph. Mathematically rheobase is described by equations (2.12) and (2.13).

$$V_m^{th}(t) = I_s R_m \left(1\text{-}e^{-d/\tau_m}\right) \tag{2.12}$$

$$\text{For } d \rightarrow \infty : V_m^{th}(t) = I_s R_m \Rightarrow I_s = I_{rhe} = \frac{V_m^{th}}{R_m} \tag{2.13}$$

The chronaxie of the cell is defined as the time needed for the membrane to reach threshold, while the stimulus applied is 2 times the rheobase. Equations (2.14) and (2.15) describe the calculation of the chronaxie (d_{chron}).

$$V_m^{th}(t) = 2I_{rhe}R_m\left(1-e^{-d_{chron}/\tau_m}\right) \tag{2.14}$$

$$d_{chron} = -\tau_m \ln\left(1-\frac{V_m^{th}}{2I_{rhe}R_m}\right) = -\tau_m \ln\left(1-\frac{1}{2}\right) = \ln 2\ \tau_m \tag{2.15}$$

This relation is used for predicting the appropriate current threshold for stimulation, depending on the duration of the pulses used in the experiment and has indeed been used in electrophysiological experiments for the characterisation of specific nerves and axons. In Rattay's study a neural cell is triggered by a point source electrode placed at several distances near the cell [17]. The results are summarised in figure 2.6 and show that the range of stimulation depends on membrane constants, pulse polarity and the diameter of the axon. In another study, strength-duration relation was used for the characterisation of neural and cardiac cells. The results, summarized in figure 2.7 show different cases of cellular activation and how the amplitude of stimuli current decreases as the duration of the stimulus pulse increases [18]. A rough reading of the graph shows that neural cells could be excited over a current density range of 10-10^4 μA/cm^2.

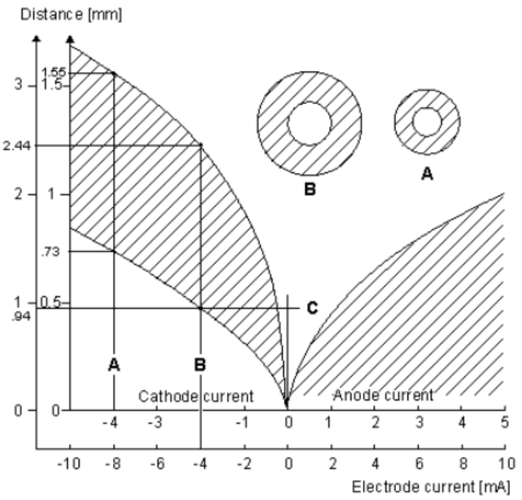

Fig. 2. 6 Current-distance relationship for unmyelinated fibres. Excitation occurs for points lying in the shaded region. For cathodal stimulation, a minimum distance arises at the point where anodal block prevents the escape of the action impulse. For anodal stimulation, block does not occur; thus there is no lower limit on the source−fibre distance. The inner scales are for a fibre diameter of 9.6µm, and the outer for a diameter of 38.4 µm [26].

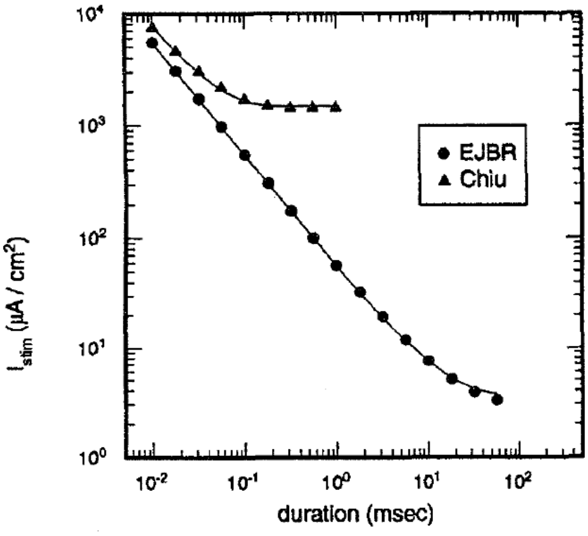

Fig. 2. 7 Strength-duration curves for cardiac (EJBR) and neural tissue (Chiu) in electrical stimulation[18].

2.3 Neural stimulation

Precise control over the activity of a large number of excitable cells, such as neural cells, has been a long-term goal of the scientific community. Until now, different approaches have been suggested for stimulation of neural cells and tissue, such as electrical, optical, thermal, ultrasound and magnetic stimulation. Electrical stimulation is the established method [19], [20] where a potential difference is applied between two, or more, electrodes to excite cell activity. Electrical stimulation is routinely used both in vitro and in vivo. There are many commercially available platforms for electrical stimulation, which face the problems of electrode degradation and corrosion, biofouling and phenomena occurring in the electrode-electrolyte interface that limit their capabilities. In optical stimulation, on the other hand the source of activation is light. Optogenetics is a promising and relatively new way of neural cell stimulation [21], which has attracted significant attention over the past years. However, since cells are not sensitive to light stimuli, they need to undergo a photosensitization procedure prior to their exposure to stimuli. This procedure usually involves the copy and transfer of the appropriate genes to the cells, adding complexity to the method, while at the same time, raising issues about the possible future application to humans [22]. Thermal stimulation has also been proposed as a successful stimulation method, where a localized gradient of temperature is created near the cell area. Different ways to create the localized gradient of temperature have been proposed [23], [24].

Ultrasonic stimulation [25]–[27] of nerves has been proposed as a macroscopic contactless method to achieve cell stimulation with implantable applications focused mainly on wireless recording applications [28]. In the following sections, a certain emphasis is given to magnetic stimulation as a method to elicit cellular activity, as it constitutes the basis of this PhD project. Starting from the main principle of TMS, the idea of bringing the TMS in the microscale is introduced and supported by studies that have already demonstrated results in this direction.

2.3.1 Electrical stimulation

Until now, a plethora of attempts on neural stimulation has been focused on electrical stimulation. Electrical stimulation of neural cells has been established as a well-known technique for the treatment of a wide range of cardiovascular and neurological diseases. However, there are some technical and biological limitations on the application of electrical stimulation, concerning the biocompatibility with imaging technologies such as magnetic resonance imaging (MRI), the limited control of electric fields and the inflammatory and immune reactions of the tissues under study because of the direct contact with the stimulating electrode [2].

Two dimensional stimulation of neurons in vitro has been attempted by using micro electrode array technology (MEA) [29], [30]–[33] that expanded over time to custom made MEA designs [34]. To overcome electrode corrosion issues, platforms with high-k dielectric insulation have also been proposed [35]. The main disadvantage of this method is the limited stimulation capacity due to the fixed location of the electrodes, non-precise stimulation and electrode-electrolyte degradation issues. Electrical stimulation has also been attempted with implantable intra-cortical microelectrodes [20] demanding an invasive manner of treatment. In Figure 2.8 some example technologies for electrical neural stimulation for in-vitro or in-vivo applications are displayed. Recent studies of electrical stimulation have proven to improve the inflammatory reaction caused by the implant, with the use of polymeric materials that possess similar stiffness to neural tissues [36], [37]. Tailoring the mechanical mismatch between soft neural tissue and the implant assures long-term performance and improves bio-integration.

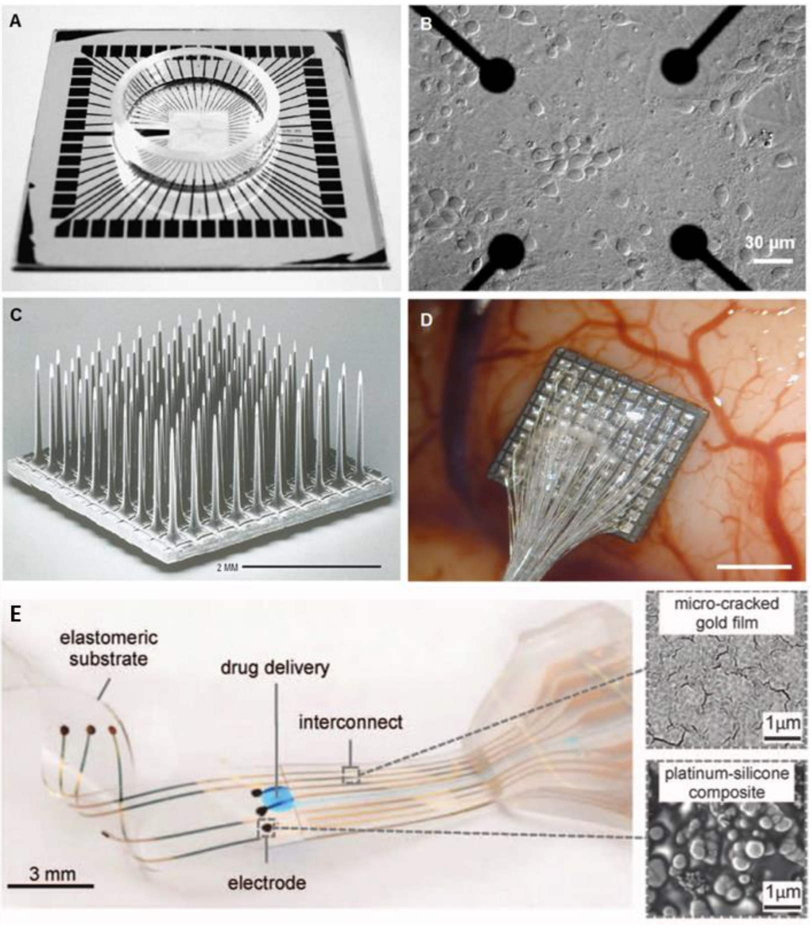

Fig. 2. 8 Examples of electrical stimulation. (a) A MEA with a ring for cell culture [30], (b) Hippocampal cells cultured on a microelectrode array [30], (c) Array electrode developed in the University of Utah, the so-called "Utah electrodes" for electrical stimulation [20], (d) Placement of Utah electrode array in temporal cortex [20]. (e) Soft neural implants developed to reduce inflammatory reactions upon implantation [36].

2.3.2 Optical stimulation

The earliest genetically targeted method, where light was used to control genetically-sensitised neurons, was reported in January 2002 [21]. In that study, drosophila rhodopsin photoreceptors were used for controlling neural activity in cultured mammalian neurons. Since then, the idea of stimulating neural cells in vitro, or even in vivo, by a source of light came in the frontline and the whole idea of optogenetics started to develop.

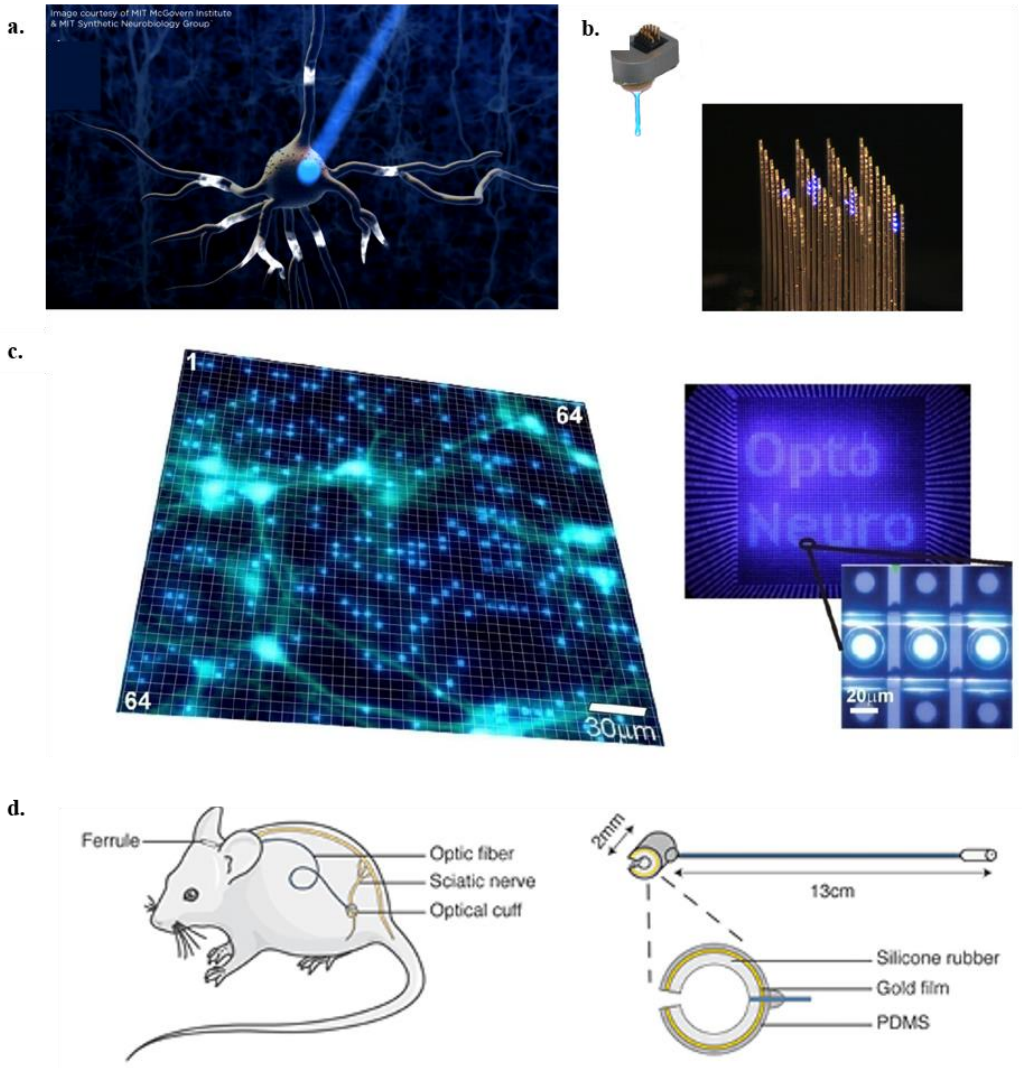

Fig. 2. 9 Examples of optical stimulation. (a) The idea of optical stimulation of a neuron [38], (b) 3-D chips for activating neural tissue in predetermined patterns. On the left, an optical micrograph shows an array of optical probes illuminated in an arbitrary pattern using a laser and tiny mirrors [38], (c) A planar micro-LED array for optical stimulation of photosensitive neural cells. Each micro-LED has individual control of intensity and timing. [39], (d) An optical cuff for optogenetic stimulation in mouse PNS [40].

In study [41], the light sensitive protein Channelrhodopsin-2 was expressed in neural cells after introducing a specific gene through virus delivery. After the necessary procedure of sensitising neurons to light, stimulation of the cells was achieved via high-speed optical switching. Two dimensional stimulation of neural cells has been similarly achieved in vitro by fabrication of an array of high power micro light-emitting diodes [39], [42]. Optogenetic approaches have been proposed for the modulation of neural activity in the central nervous system, while recent studies suggested their use to the more complex peripheral nervous system (PNS) [40]. In Figure 2.9, exemplar technologies of optical stimulation on neural cells are presented. Even though this technique is under development for more than 10 years, there are still outstanding challenges to be addressed [22]. The most important disadvantage of this method is that neurons need to go through a photosensitization procedure prior to their stimulation, a fact which increases the complexity of the technique. Other than that, the penetration length in the tissue is quite low and there is no possibility to modulate directly the extracellular potential, which is important for studying the effect of field potential on neural activity.

2.3.3 Thermal stimulation

Thermal stimulation is one more alternative approach of stimulating excitable cells and several studies have been successfully performed by this approach [43], [44]. In [43], the high aqueous absorbance of millimetre wave (MMW) radiation led to a significant increase of the action potential firing rate in excitable cells, as predicted by Hodgkin-Huxley model of neurons [15]. In addition in [44], an approach is presented that allows to remotely activate temperature-sensitive cation channels in cells through radio frequency magnetic field heating of nanoparticles. Superparamagnetic ferrite nanoparticles were targeted to specific proteins on the membrane of cells and heated by a radiofrequency magnetic field. The induced temperature increase is highly localised and able to stimulate neural and other types of excitable cells. In [45], the design considerations and reliability issues of a CMOS micro-heater array are studied, for neural stimulation in Lab-on-Chip (LOC) applications. Finally, a recent study [46] presented the idea of thermal stimulation of excitable cells through a light source. The mechanism of infrared stimulation was suggested as a means to increase locally the temperature and alter the capacitance of the plasma membrane; leading to the activation of the target cell. Finally, in [47] a similar idea of wireless magneto-thermal stimulation is proposed for deep brain applications, where excitation was achieved through the heat- sensitive capsaicin receptors of neural cells. Figure 2.10 a, b summarises the different mechanisms in state-of-the-art thermal stimulation techniques. It is worth mentioning that magnetic and thermal stimulation could be coupled in a real case scenario, as excitable cells are quite sensitive in small changes of the temperature and this possibility should be taken under consideration.

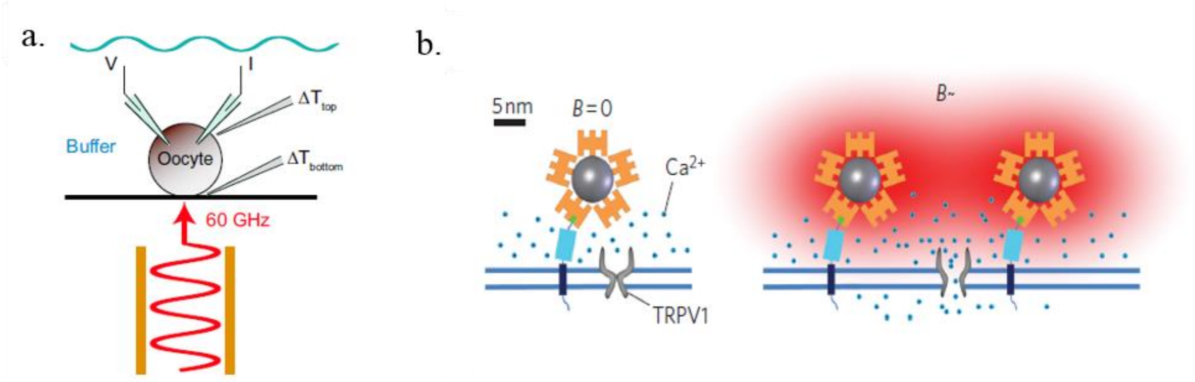

Fig. 2. 10 Thermal stimulation of excitable cells. (a) Temperature changes induced by millimetre wave stimulation. Experimental setup: Excitable cells rest 1mm above a waveguide transmitting a 60GHz millimetre wave from an RF generator. Local changes in buffer temperature are measured on the bottom and top of the excitable cell [43]**. (b) The mechanism of ion channel stimulation using nanoparticle heating. Schematic shows a superparamagnetic nanoparticle (grey) coated by streptavidin (orange) in the absence (left) and in the presence (right) of a RF magnetic field. The heat induced by the magnetic field leads to the opening of the ion channel and the activation of the cell** [44]**.**

2.4 Summary

In this chapter, a brief introduction on the neural cells characteristics was presented in order to give the background information and enhance the understanding of the bio-physical phenomena which control the mechanism of cell stimulation. A second scope of this chapter was to present the state-of-the-art technologies proposed to evoke cell activity in vitro or in vivo. The presented methodologies are governed by totally different first principles, resulting to different advantages and disadvantages in every case. These technologies are competitive techniques in the field of neural stimulation and stand in the opposite side from magnetic stimulation which is described in more detail at chapter 3.

Chapter 3

Magnetic stimulation and state-of-the-art technologies

Chapter 3 focuses on magnetic stimulation and the advantages of the method in comparison to the previously presented stimulation methods. Transcranial magnetic stimulation (TMS) is used macroscopically in the brain to excite neuronal activity in a contactless manner. The same principle could be transferred in the microscale and excite the activity of a single cell or cell population. The chapter presents the evolution and constant shrinkage of technologies which have been proposed over the years for millimetre and sub-millimetre magnetic stimulation of neural tissue. Further size reduction brought in the foreground microscale technologies only very recently, setting the scheme for real microscale TMS (μTMS). At another point, this chapter highlights the state-of-the-art methods in fabrication of micro-scale inductors.

3.1 Magnetic stimulation: from macroscale to microscale

Transcranial magnetic stimulation (TMS) is used to stimulate neuronal regions in the brain in a non-invasive manner and has been developed over the past decades [6], [48]–[50]. TMS has been used for treating several diseases, such as Parkinson [51], [52], dystonia [53], [54] and chronic neuropathic pain [55], [56]. It has also been proposed to treat some forms of depression [57] with moderate success and is under evaluation for the treatment of strokes, tinnitus and migraine headaches [58]–[60]. In this method, a magnetic coil is used externally to the scalp in order to generate a magnetic field, which easily passes through the skull and induces electric currents that stimulate the targeted brain region. In figure 3.1 shows a schematic of the transcranial magnetic stimulation method. Existing devices for TMS cannot generally reach further than two inches into the brain, making it impossible for use in deeper, sub-cortical targets, while the spatial control with the existing devices is limited. In addition, TMS requires large power sources [61] to create the magnetic fields, as the coils are large and far from the brain tissue. TMS devices need to be large in size to guarantee that the strength of the magnetic field is enough to activate neural tissue across long distances. This results in the need of having a patients under TMS treatment in the clinic for quite a long time [2]. On the other hand, the main advantage of magnetic stimulation is that it is a non-invasive method which overcomes all the limitations related to the direct contact of living tissue with an electrode.

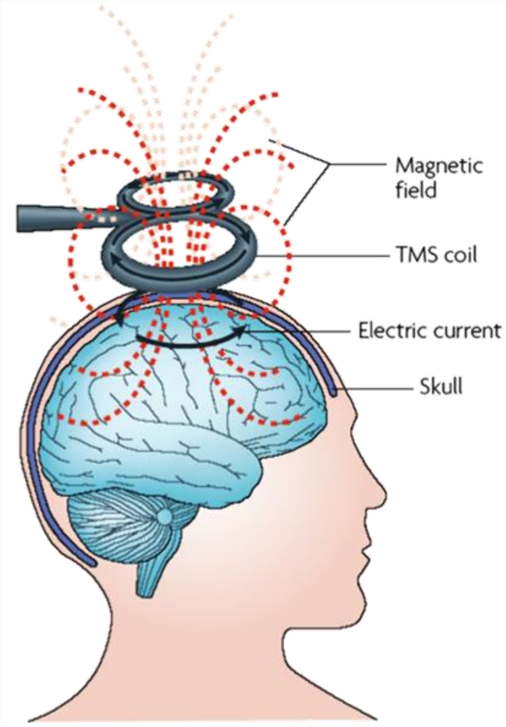

Fig. 3. 1 Schematic of transcranial magnetic stimulation principle.

The idea of using the TMS principle in coils of reduced size led to early attempts of neural stimulation with miniaturised electromagnets. The neurophysiological mechanism of magnetic stimulation was studied by implementation of mini-coils in the brain of behaving primates [62]. The mini-coils, which had a size of some tens of millimetres, were used both for activating brain areas and for simultaneous extracellular recordings. In parallel, a number of studies focused on numerical calculations, modelling and design considerations of coils for micro-magnetic stimulation [63]–[70]. An interesting design was proposed in [71], where a multi-layered planar coil in millimetre scale was fabricated on a liquid crystal polymer substrate to allow for possible retinal prosthesis applications. In study [72], a circuit and coil design were suggested for in vitro magnetic neural stimulation. Finally, in [73], a novel CMOS platform for magnetic stimulation and recording of neural tissue is suggested in the form of a 8x8 micro-coil array. However, the maximum possible value of the magnetic field is restricted due to limitations on the dimensions of micro-coils and input current that CMOS technologies permit, a fact which makes magnetic stimulation more difficult. Over the years, modelling and circuit design considerations for systems of millimetre-scale magnetic stimulation have been proposed [72]–[74].

Recent studies have demonstrated that even smaller, sub-millimetre scale commercially available electromagnets, can activate neuronal tissue or cells both in vitro and in vivo [2]–[4], bringing in the foreground the possibility that micro-magnetic stimulation coils, small enough to be implanted within the brain, may prove to be an effective alternative to existing stimulation devices. A number of advantages has attracted the scientific interest. Firstly, the fact that the electromagnet can be completely insulated with soft bio-compatible materials eliminates inflammatory reaction related to implantation [75], [76]. Several bio-compatible materials already presented in different technologies, could be used without significant loss of efficiency, such as polyimide [77], [78], Parylene-C [79] and liquid crystal polymers [78], [80], [81]. Similarly to TMS, the tissue-electrode related problems are also avoided [82]–[85], known as the most significant disadvantages of electrical stimulation. An additional advantage of magnetic stimulation has to do with the spatially asymmetric nature of the induced electric field created in the vicinity of an inductor. The asymmetry can be used as a method to selectively activate only a targeted region of a neural population and avoid others [2], [86]. Study [2] firstly demonstrated sub-millimetre magnetic stimulation and confirmed that elicitation of neural activity is affected by both the orientation of the coil and the magnitude of the stimulation signal. In study [4], similar experiments were performed in vivo and prove that micro-magnetic stimulation (μMS) is capable of successfully activating neuronal circuity in the cochlear nucleus. In study [3], the magnetic stimulation was used in an attempt to explore whether suppression of neural activity is possible. The result showed that repetitive magnetic stimulation, performed by a 0.5mm diameter coil, achieved a 70% successful suppression of subthalamic nucleus activity, while in [87] and [88], with the same size coil the magnetic stimulation of cortical pyramidal neurons was achieved. At another study [89], a submillimetre sized inductively coupled neural stimulator, in the form of a coil, is present as a proof of concept. The study further describes the challenges related to the inductive coupling of tiny inductors. Finally, very recently a micro-scale electromagnet was proposed as an implantable component for intracortical magnetic stimulation [1]. Figure 2.14 summarizes the most important studies on the miniaturisation of magnetic stimulation from sub-millimetre to micro-scale electromagnets.

The focus of the research presented here is to use the TMS principle in the micro-scale and demonstrate a two dimensional device which can create spatio-temporal magnetic flux profiles on demand and can elicit neuronal activity in vitro.

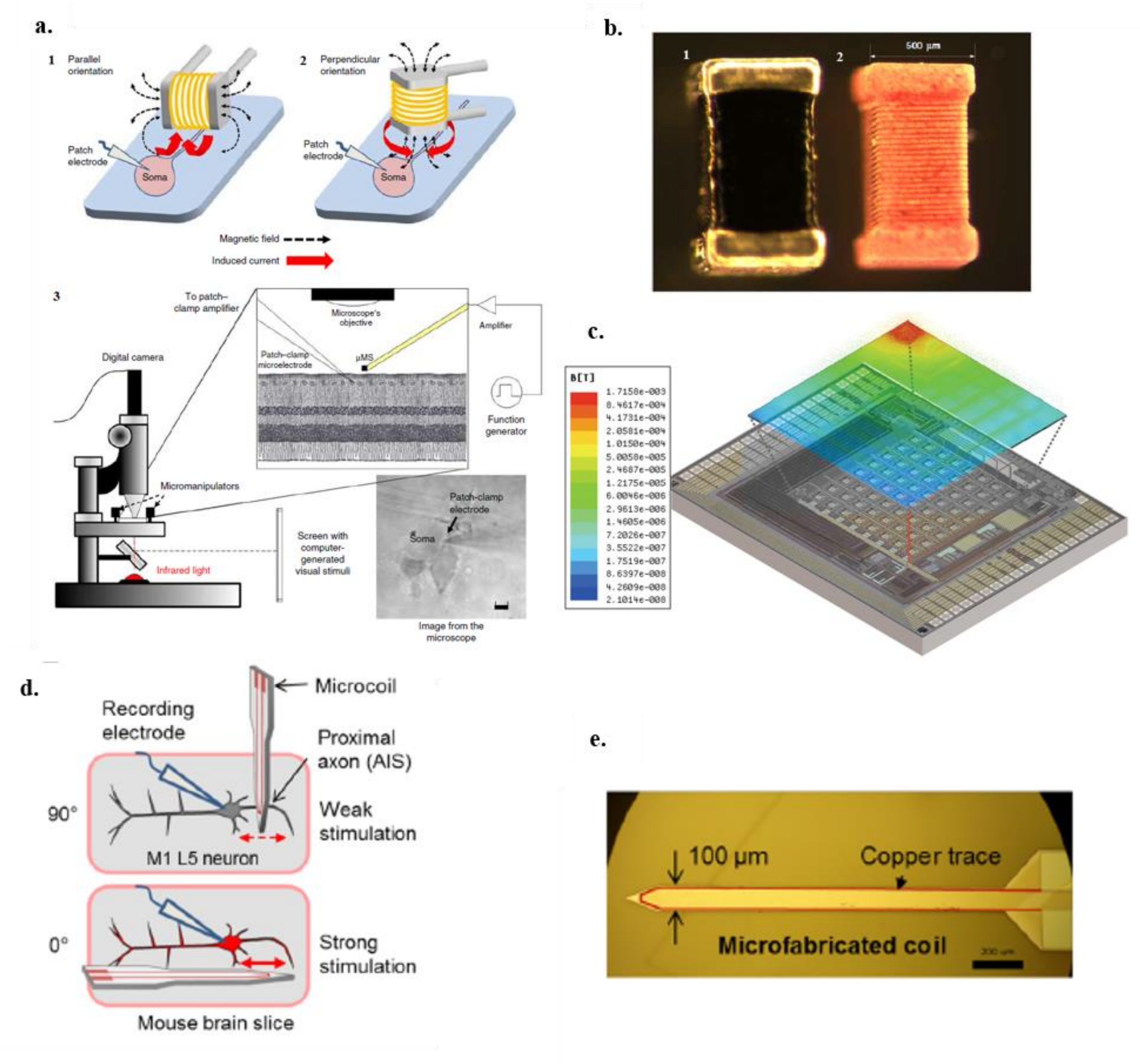

Fig. 3. 2 Microscopic magnetic stimulation of neural tissue. (a) 1, 2 Schematic graph presenting magnetic stimulation of a neuron with two different coil orientations affect magnetic stimulation. 3 Experimental setup showing magnetic stimulation and signal recording from the neuron. (b) The sub-millimetre inductors used in the electrophysiological experiments. (Images adapted from [2]). (c) A novel CMOS-based Lab-On-Chip array for the combined magnetic stimulation and opto-chemical sensing of neural tissue. (Image adapted from [73]). (d) Schematic representation of neuronal stimulation with a micro-scale electromagnet. (e) Image of the fabricated electromagnet (Images adapted from [1]).

The magnetic field production would be localised above the activated micro-coils and a planar array configuration was proposed, simultaneous neural stimulation at more than one points would be possible. The idea is to create a device which can control or influence the activity over a targeted neural region or of a single cell. Figure 3.3 shows a schematic representation of the conceptual idea or this research study. The proposed device would reach a minimum spatial resolution of 50μm and would be able to activate neural populations over a versatile region with minimum surface area of 425μm x 425μm and maximum of 1600μm x 1600μm, depending on the requirements of a specific application. Moreover, the challenges of this methodology are also studied. Limitation factors, such as the maximum current the micro-inductors could hold without facing electrothermal deterioration should be taken under consideration (e.g. devices to be engineered with thicker cross sections by electroplating). The final goal would be to have a device which could hold the necessary amount of current and lead to neural activation. The use of the device would be limited to in vitro applications. However, the possibility to transfer the technology into flexible bio-compatible substrates could pave the way for the future implementation of a useful neuro-stimulating tool.

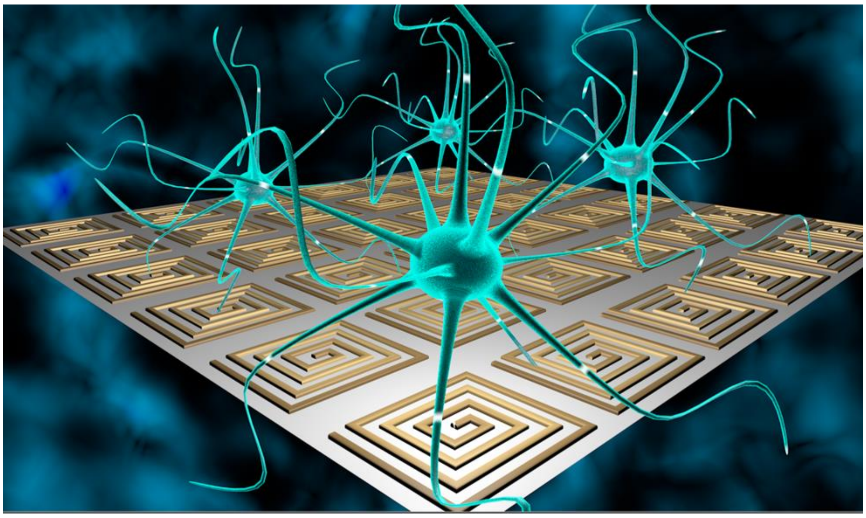

Fig. 3. 3 Conceptual idea of non-invasive magnetic stimulation from an array of micro-coils.

3.2 State-of-the-art fabrication of microscale inductors

The need of downscaling inductors in integrated circuits has been a long-term requirement for a broad range of applications, while the development of microfabrication techniques has assisted towards this direction. In the majority of applications micro-coils are usually exploited in the radiofrequency (RF) range. Typical examples can be found in antenna applications, transformer designs [90], [91], low noise amplifiers [92] and filters. In tandem, a number of different technologies [93] and geometries [94] have also been proposed in order to improve their performance and enhance their efficiency. Integrated inductors have also been used as sensors [95], in microscale NMR applications [96], [97] and as transmitter-receiver systems for human body implants [98]. Microscale inductors have been used in microelectromechanical systems (MEMS) technologies [99]–[102].

Despite the differences in the geometric characteristics, in most cases the proposed fabrication procedures of planar spiral inductors are very similar between the studies. Depending on the activation pads and their position in geometry, the procedures might include the presence of a seed layer. [99], [101], [103], [104]. This metallic seed layer is used in combination with photolithographic patterning for the increase of the metal thickness with electroplating. After reaching a desirable thickness the seed layer is removed. The fabrication methods are further tailored for inductors which function in the RF frequency range as high quality factors demand inductors on thick insulating materials to reduce losses. Specifically, in studies like [93] the fabrication of inductors was performed on top of SiO_2 islands with a relative high thickness of 50μm. Similar approach was followed for the three dimensional inductors in [105].

The development of microscale inductors has also been successfully presented on flexible substrates either for magnetic actuators [101] or magnetic sensor applications [104]. In the latter case, planar and three dimensional inductor configurations have been transferred to Kapton and Peek flexible substrates and in both cases the implemented devices show better electrical performances in terms of quality factor, compared to devices on standard oxidized Si substrates for a wider frequency range. This is due to the dielectric nature of these substrate materials which keeps losses to a minimum. On the other hand, a comparison focusing on the failure of the inductors due to thermal deterioration, between inductors fabricated on conventional Si wafers and polymeric flexible materials (e.g. Kapton) has shown opposite results. Specifically, there seems to be an influence of the substrate on the maximum current density a geometry could hold without significant thermal deterioration [106]. This is explained by the different thermal parameters of the substrate material (e.g. thermal conductivity). Figure 3.4 depicts examples of planar spiral micro-fabricated inductors with different geometric characteristics, developed for different applications.

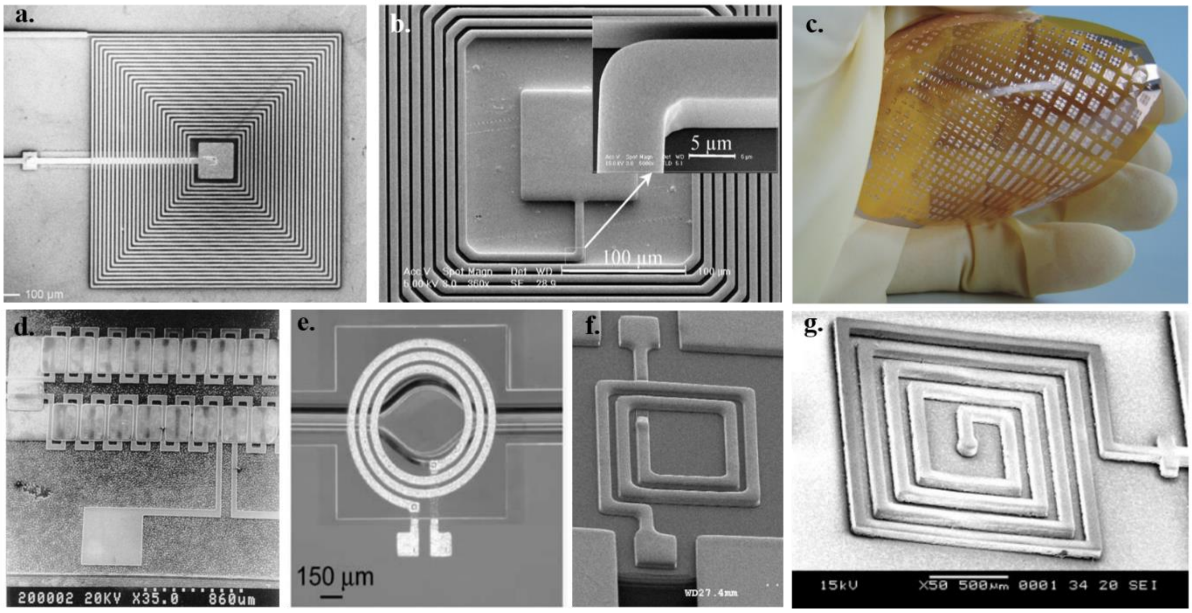

Fig. 3. 4 Example planar inductor geometries using state-of-the-art microfabrication methods. (a) **Micro-coil developed for MEMS scanning applications [99]**, (b-c) **Planar micro-coil geometry developed on flexible Kapton substrates for sensing applications [104]**, (d) **Toroidal-meander planar inductor developed with CMOS compatible methods [100]**, (e) **A circular planar inductor on top of a microfluidic channel for NMR spectroscopy applications [96]**, (f) **Top SEM view of a high quality factor planar inductor on top of a thick dielectric material [93]**, (g) **Planar microfabricated inductor on a microwave magnetic substrate (YIG) [103]**.

3.3 Summary

On this chapter a particular emphasis was given to transcranial magnetic stimulation which inspired the development of relatively small electromagnets for magnetic stimulation in neural populations in vitro and in vivo. There was a particular focus on its advantages over the alternative methods of excitable cell stimulation and on the evolution of the micro-magnetic devices over the years. The presentation of the state-of-the-art fabrication methods for the development of microscale inductors was another focus of this chapter. The idea of this PhD, is to go a step further in the direction of planar magnetic stimulation and to make structures that can produce micro-scale magnetic flux profiles on demand, capable to elicit neuronal activity in vitro and at the same time simple in fabrication, in order to be easily transferred to flexible substrates and pave the way for future multi-addressable magnetic neuro-stimulating tools.

Chapter 4

Simulations and design

The scope of this chapter is the electromagnetic design of micro-inductors with the help of a FEM software. The results are obtained by COMSOL Multiphysics software [9] which is a powerful simulating tool and uses finite element analysis. The simulations are useful to understand how different geometric parameters affect the efficiency of a micro-coil. The simulation analysis serves a means to decreases time and resources from the experimental procedure. The module used for the description of the physical problem is the AC/DC and specifically the *Magnetic and Electric Fields*. In a number of simulations the “Joule Heating” module is also weakly coupled to the “Magnetic and Electric Fields” module, in an attempt to test the impact of the temperature in the geometry. The results of the simulation study are taken into account for the design of the photolithographic masks. The final part of this chapter focuses on important experimental considerations which impose a broadening in the range of design characteristics.

4.1 Design with COMSOL Multiphysics software

As a first step, the study of a reference structure will be presented. In the next steps parametrical testing will be used to show how the different geometric characteristics affect the efficiency of the micro-coils. The geometry used as a reference is depicted in figure 4.1. At a first approach, the chosen structure characteristics follow the needs imposed by the application. Specifically, the size of the micro-coils is chosen to be comparable to the size of the cells with a surface area of 50μmx50μm, the micro-coil material is chosen to be Au which entails no bio-compatibility risk. The simulations were limited to square geometries in accordance to other studies were square planar inductor geometries were proposed [93], [99], [100], [103], [104] even though, circular inductors are also expected to have similar electrical behaviour. The metal track width and the spacing between the turns are both set at 2μm. The thickness of the micro-coil is chosen 5μm and the insulator thickness is assumed to be 1μm higher (6μm in total). The insulating material is Parylene-C and is preferred not only due to bio-compatibility issues, but also due to its simplicity in the deposition of a micro-scale thickness. In figure 4.1, layer 1 depicts the Si wafer and layer 2 the insulating Parylene-C layer.

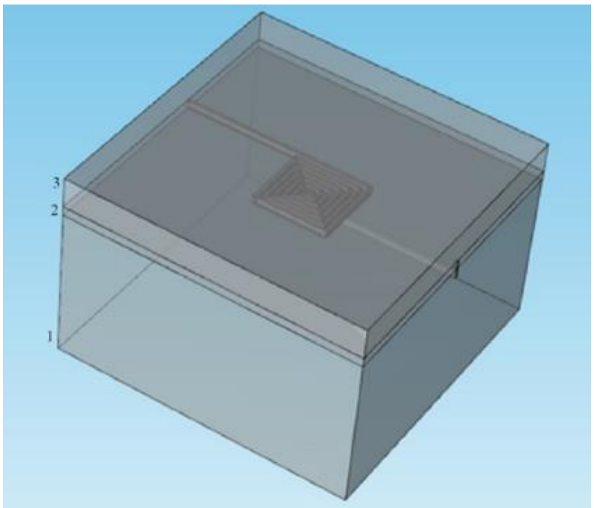

Fig. 4. 1 Example of a structure modelled in COMSOL Multiphysics. Layer 1 denotes the substrate, layer 2 the insulating material above the coil and layer 3 the neural tissue.

For better accuracy on top of Parylene-C a rectangular box of thickness 20μm which represents the neural tissue was further assumed. This entity is given the electric characteristics of neural tissue[107]–[109]. The current flowing through the micro-coil is chosen at 8mA. A sinusoidal input to the coil at the frequency of 1kHz is chosen, similar to a bio-realistic activation scheme. In this study, the magnitude of the magnetic field produced by the micro-coils is used as a figure of merit for a direct comparison between the geometries. The stronger the magnetic field the stronger the electric field induced. Figure 4.2a,b presents the magnetic flux density magnitude B at a distance 1μm above the micro-coil, at the top surface of the insulating material (z = 6μm), both as a field map and 3D configuration. Figure 4c shows a 3-D streamline of the magnetic flux density in a vertical cross section at the centre of the micro-coil.

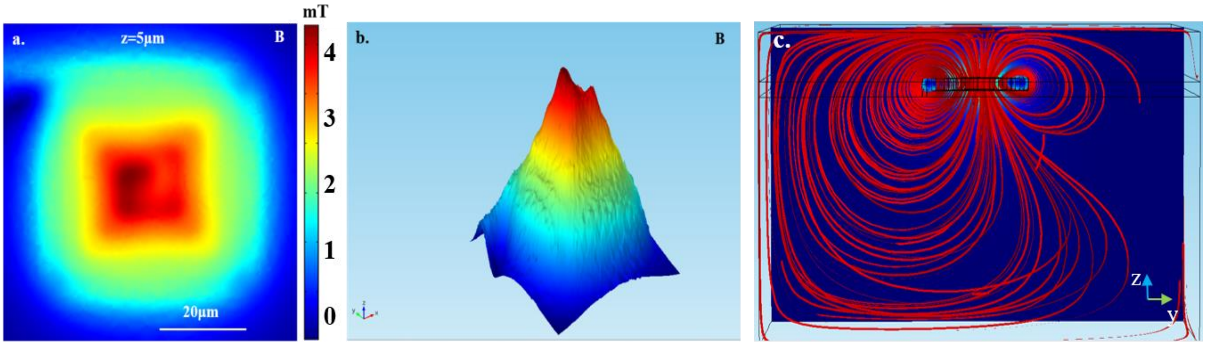

Fig. 4. 2 Spatial distribution of magnetic flux density magnitude B at z = 6μm. (a) a field map and (b) a 3-D representation of the magnetic flux density magnitude, (c) A 3-D streamline of magnetic flux density illustrated in a vertical zy cross section at the centre of the micro-coil.

In comparison to other literature studies, the magnetic field produced by the suggested electromagnet is similar or slightly higher. Specifically, the maximum value is 2.5 times higher than the simulation result in study [110], where a CMOS micro-coil array for magnetic stimulation was developed. The maximum value is also 1.34 times higher in comparison to studies [111], [112] where structures for magnetic manipulation were developed based on CMOS technology and 1.5 times higher in comparison to [113], where a circular microelectromagnet for magnetic manipulation of nanoparticles was developed.

Another important figure of merit of magnetic stimulation, is the induced electric field near the coil and the spatial derivative of the induced electric field in a horizontal plane, in the direction of either the x or y axis. Figure 4.3 shows schematically the stimulation sites in respect to the micro-coil geometry.

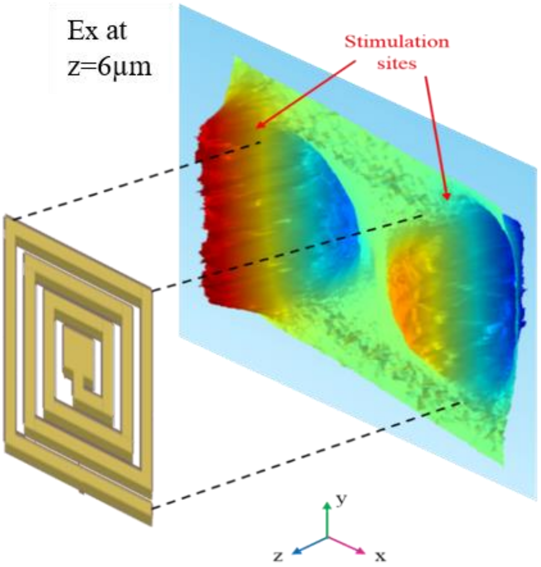

Fig. 4. 3 A 3-D representation of the spatial distribution of the x component of the induced electric field at a distance z = 6μm. The sites of stimulation are denoted in respect to the micro-coil geometry.

Comparison of the results to thresholds of activation suggested in literature, define the range of functionality of each device. Figure 4.4 summarizes the results for the the x and y components of induced electric field, at a distance z = 6μm. On the right, the results are again depicted in a 3D configuration. The received maximum value of dE_x/dx is approximately 10^9V/m^2 (at z = 6μm). This is well above the value of 11kV/m^2 which has been reported in [5], [114] as the threshold of stimulation for peripheral axons. This result corresponds to a current input of 8mA. The reason behind the significantly higher value from the threshold arises from the possibility of placing the cells in great proximity to the coil. In terms of fabrication, the proximity is mainly determined by the thickness of the Parylene-C insulating layer which covers the micro-coil. As the distance from the micro-coil increases the magnetic field and the induced electric field drop, up to a point that threshold of activation is not anymore reached, unless there is a further increase in the biasing current.

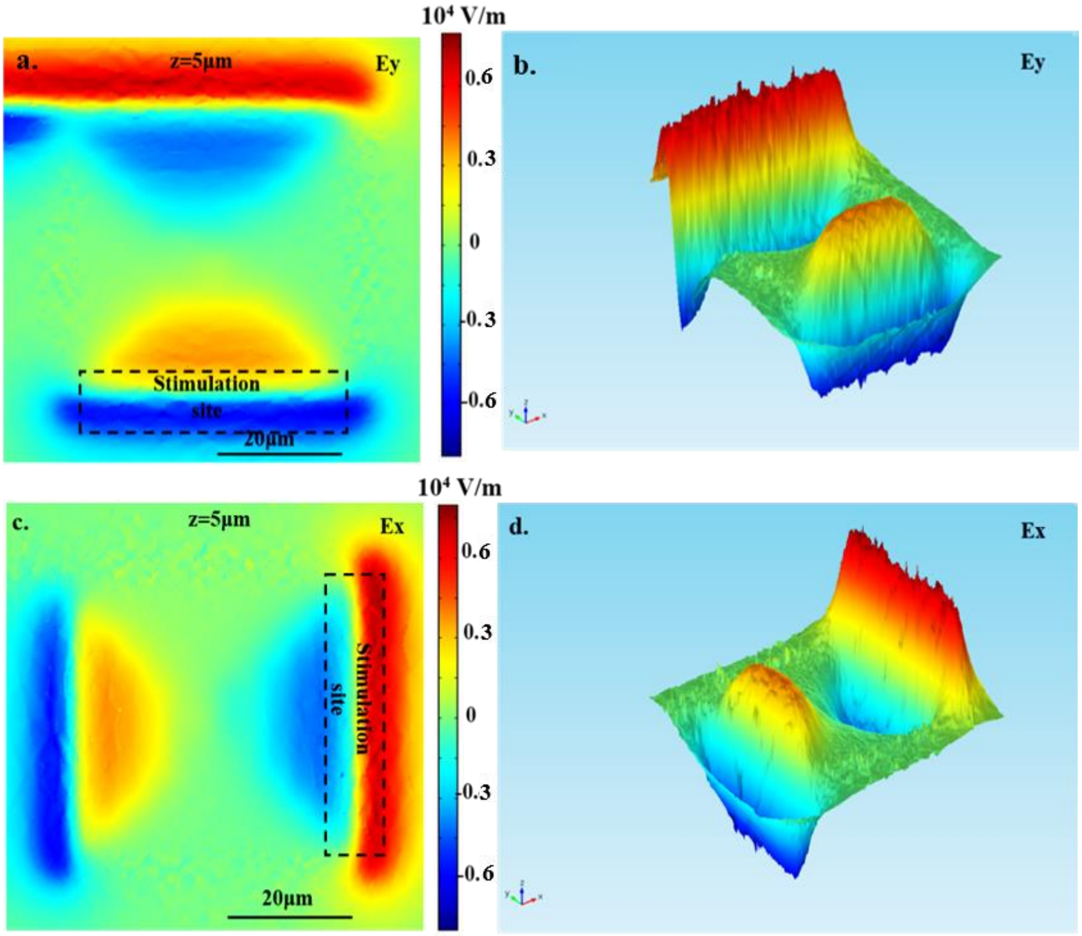

Fig. 4. 4 A 2-D and a 3-D representation of the spatial distribution of x and y components of induced electric field, at a distance z = 6μm (a,b) x component of induced electric field (E_x) and (c,d) y component of induced electric field (E_y).

4.2 Parametric study

In this subsection the simulations are repeated with only one parameter of the structure changing at a time. In this way it becomes apparent which geometric and experimental characteristics lead to a stronger magnetic field.

4.2.1 Number of turns

The first parameter which is checked is the number of turns in a micro-coil and how this affects the produced magnetic field. Starting from the reference structure of 6 turns and moving to a micro-coil with a single turn the magnetic flux magnitude was measured. The whole area of the coil remains 50μmx50μm in all cases. Figure 4.5 gives the maximum value of the magnetic flux density, along with the increase of the number of turns. As expected the magnetic flux density is increasing as the number of turns increase. The addition of more internal turns resulted also in the spatial localization of the magnetic flux in the centre of the coil.

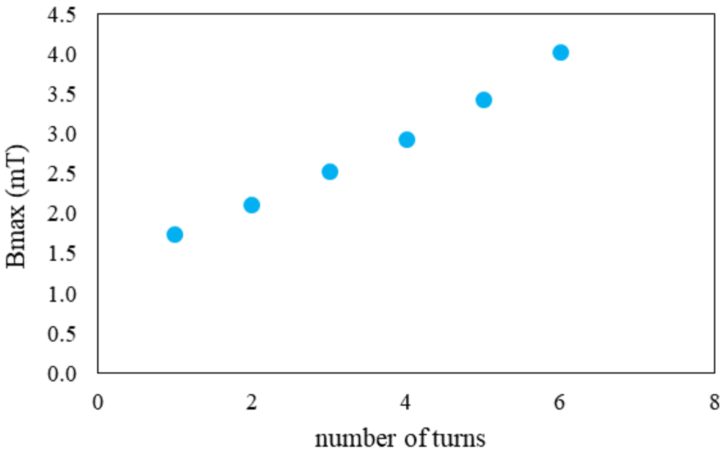

Fig. 4. 5 The dependence of magnetic flux density maximum on micro-coil's number of turns.

4.2.2 Metal track width

The next parameter which is taken under study is the width of the metal track in the micro-coil. Different widths were checked ranging from 2μm to 10μm. The results for the maximum value of the magnetic field are presented in figure 4. 6 and show an improvement as the width of the micro-coil decreases. This is something expected as the increase of the width affects the number of turns since the micro-coil surface area remains the same at 50 μmx50μm. The graph further illustrates a non-linear behaviour as the metal track width increases. This means that changes in metal track width become more important for a geometry with small track width (higher number of turns). In contrast, for larger width values, the differences in the metal track width seem not to be equally important.

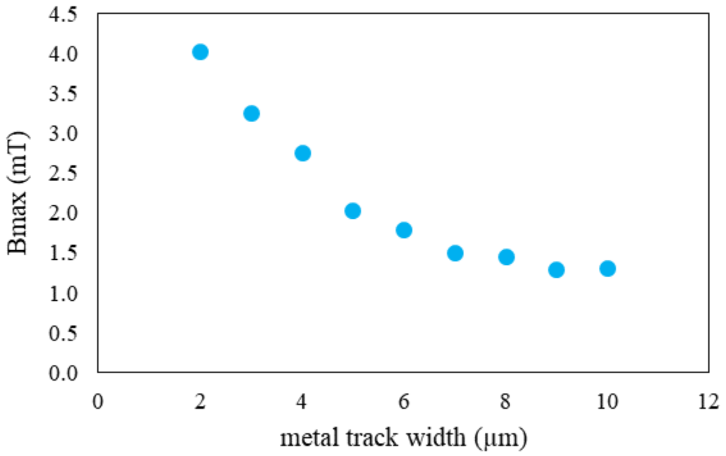

Fig. 4. 6 The dependence of maximum value of magnetic field on the metal track width of a micro-coil.

4.2.3 Spacing between turns

Here the changing parameter under study is the spacing between the turns. Three additional structures with spacing of 4µm, 6µm and 8µm are compared with the reference structure. The results are displayed in figure 4.7. As illustrated on the graph, with the increase of spacing between the turns the maximum values of magnetic flux density decrease in a linear manner.

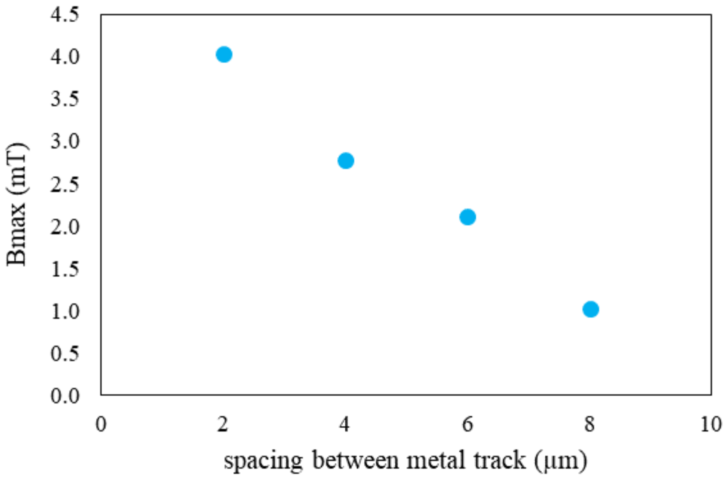

Fig. 4. 7 The dependence of maximum value of magnetic field on spacing between micro-coil's turns.

4.2.4 Magnitude of AC current

An additional parameter which is studied is the magnitude of the AC input current which flows through the micro-coil. Four biasing input currents are studied, namely 2mA, 4mA, 8mA and 16mA. The results are presented in figure 4.8.

The maximum of the magnetic flux density depends linearly on the input current which is used for the activation of the coil. However, the magnitude of the input current is in general a limiting factor for the micro-coil, as with an irrational increase the temperature of the metal is expected to increase as well. In other words, a high current amplitude triggers thermal deterioration phenomena. This should be taken into consideration in the experimental biasing of the micro-coils and deserves a separate experimental study, which is presented in chapter 6.

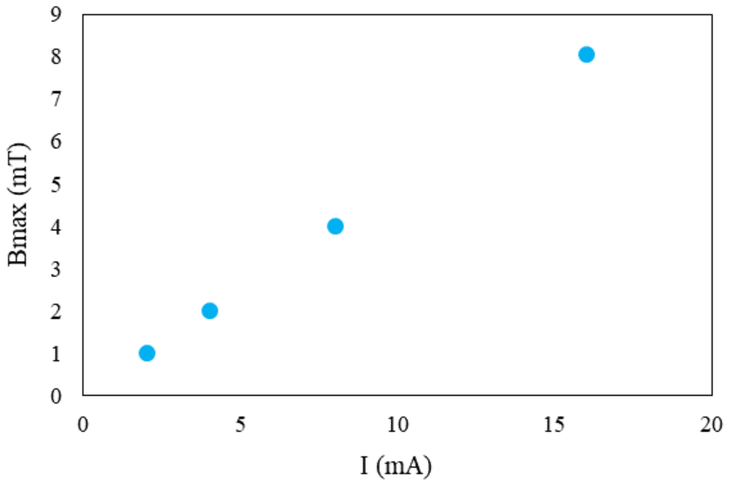

Fig. 4. 8 The dependence of maximum value of magnetic field on the magnitude of AC input current.

4.2.5 Micro-coil material

A number of micro-coil materials, with different electrical conductivities, were tested in the simulation (Ti, Pt, Ni, Al, Au, Cu, Ag). Since both the geometry and the biasing current remain constant no change is expected in the maximum magnetic flux magnitude and indeed this is what is observed in figure 4.9. However, in a scenario that the biasing of the micro-coil would happen with a voltage source the electric conductivity of the material would become important and this is something which is taken into account in chapters 6 and 8.

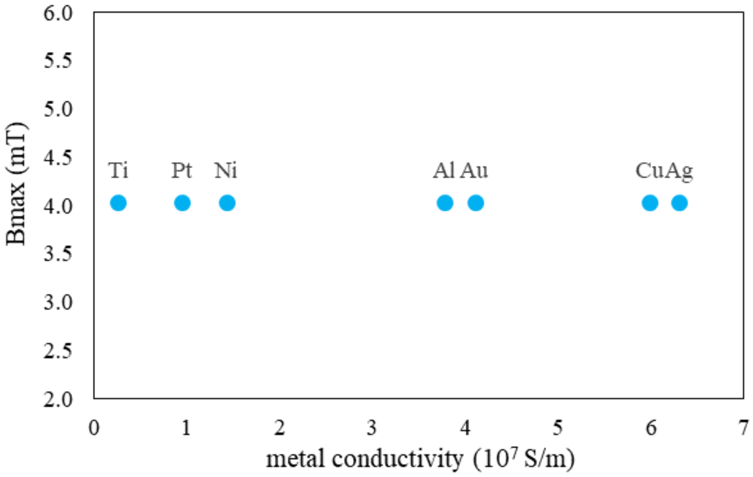

Fig. 4. 9 The dependence of maximum value of magnetic field on the micro-coil material.

4.3 The effect of temperature

The final attempt on the simulation study, was to couple two different physics modules in COMSOL. In more detail, the coupling between "Joule Heating" and "Magnetic and Electric fields" modules, is useful for plotting the temperature distribution in the structure. At the design point, this study was a first approach on the thermal deterioration phenomena which affect the behaviour of the micro-coils. The reference structure, with a metal track cross section of 10μm^2, was inserted in COMSOL and the multiphysics modules were set. The model run for different magnitudes of input current. Below, in figures 4.10 and 4.11, the examples of 20mA and 80mA are presented.

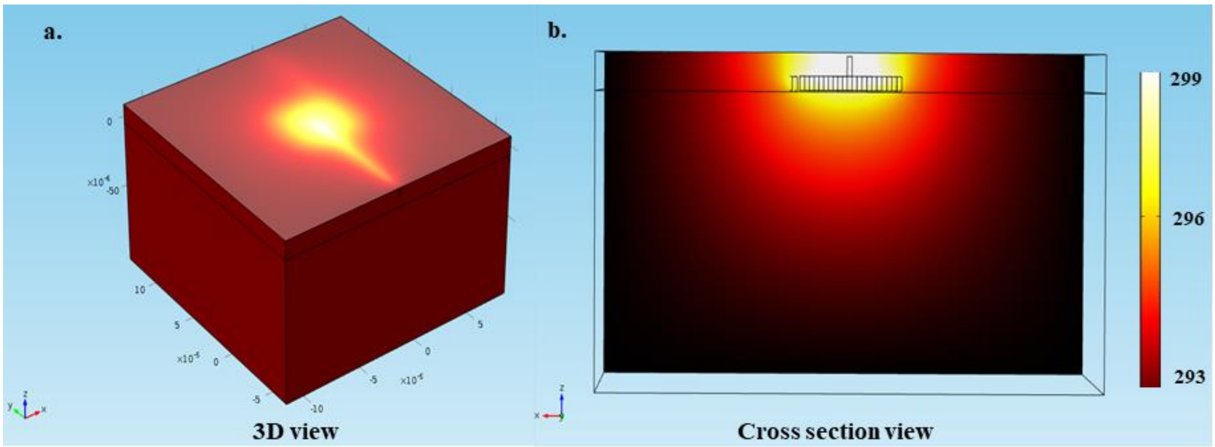

Fig. 4. 10 (a) Illustration of temperature distribution for the reference structure just above the insulating material and (b) on a cross section of the structure. The magnitude of the input current is set to 20mA.

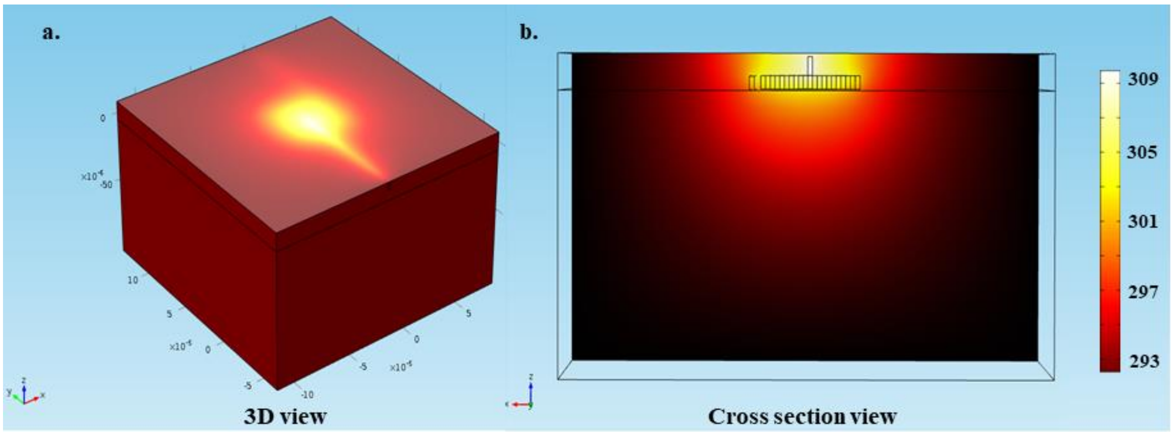

Fig. 4. 11 (a) Illustration of temperature distribution for the reference structure just above the insulating material and (b) on a cross section of the structure. The magnitude of the input current is set to 80mA.

For the biasing input of 20mA, the maximum temperature is observed just above the centre of the micro-coil. The temperature range, for the thick geometry under study, is reaching approximately the 5K above the room temperature, which is set at 293K. In contrast, the temperature increases significantly in the case of 80mA. The maximum temperature is located again above the centre of the micro-coil, but the new range of temperature change is approximately 15K.

4.4 Design considerations

The results of the previous study showed the characteristics which improve the performance of the micro-coils. In principle, for the case of a 50μmx50μm surface area micro-coil, the denser the metallic tracks the stronger the magnetic field it produces and the more localised in the centre of the coil. The results are similarly extrapolated for a higher surface area micro-coil. The maximum values of magnetic flux density for the reference structure was directly compared to other literature studies, where inductors are fabricated for stimulation or manipulation purposes [110]–[113]. As discussed, the proposed design shows similar or improved values of magnetic flux density maximum. Taking into account the results from the parametric study and the thermally coupled modelling, it becomes apparent that this result is significantly improved for a higher current amplitude. Specifically, the field doubles in strength and reaches 8mT, as the current doubles as well to 16mA, without showing any excessive increase of the temperature (e.g. for 20mA the reported ΔT was 5K). The amplitude of the biasing current is a very important parameter in the design due to the fact that it could be easily controlled in an experiment, without the need of testing an alternative geometry. At the same time it affects importantly the efficiency of the micro-coil. However, the importance of the thermal deterioration phenomena demands an experimental electrothermal study, which will be analytically presented in chapter 6. The electrothermal study was performed in fabricated micro-coils of different cross sections and the results presented there are in agreement with the results from COMSOL modelling.

The importance of achieving a high biasing current for the micro-coils is taken into account in the design considerations. As presented in the next chapter, electroplating will be used as a method to have bigger metallic cross sections and allow higher current capacities to flow through the coils. However, electroplating limitations bring to the foreground the need to design geometries with bigger spacing between the metallic tracks in order to overcome the functionality issues related to the isotropic growth of electroplated material. This is discussed in more detail in section 4.5 where the designs included in the mask are presented.

Last but not least, it should be mentioned that the maximum values of magnetic field could be further improved if needed, by two other methods. Firstly, by creating a micro-coil with a larger surface area. More metallic tracks will act additively and will enhance the strength of the produced magnetic field. Arrays with micro-coils of surface areas 100μmx100μm will be designed and fabricated, not only as a back-up plan in case higher magnetic fields will be required in the biological experiment, but also for the possibility to test them with bigger cells. A disadvantage of a bigger micro-coil surface area is that it loses some of the resolution in the localisation of the magnetic field, which could lead to a simultaneous stimulation of more than one neural cells in a bio-experiment. The second method to further enhance the produced magnetic field is by inserting a ferrite core (with a lithographic step) in the centre of the planar coil. This approach has not been neglected, but decided to be avoided, due to its fabrication complexity and the difficulty to control the hysteresis, losses and temporal delay in response inserted by the ferromagnetic material.

4.5 The design of the photolithographic mask

The design of the mask was carried out with Tanner Tools EDA L-EDIT software. Some structures designed on the mask are following on figure 4.12. Two different micro coil geometries have been designed: one with 50μm^2 surface area and one with 100μm^2, as different biological preparations have different properties (dimensions or even different threshold of activation) and the devices should function over a large range of properties. In addition, the different geometries would achieve different spatial resolution, which will be an important characteristic for future purposes. Micro-coils of different metal width are also designed, which could hold a larger amount of current flowing through them.

Finally, as electroplating will lead to micro-coils' thicknesses comparable in size with the spacing between the turns, there is a limit above which, further increase in the thickness would lead to the shorting of two consequent metal wires. As a result, 3 different ratios between spacing and metal wire width have been designed for every structure. From the simulations analysis, it is expected that the denser structures, with many turns and small spacing between them, would be more efficient and produce a stronger magnetic field. However, this design consideration is important as micro-coils with increased thickness are expected to be tolerant to higher current capacity. The electrothermal study and the bio-experiment would indicate the optimum balance between the two limits. As a result, three ratios between metal track width and spacing are fabricated namely 1:1, 1:2 and 1:3. Beside the single coil geometries, 6x6 arrays of micro-coils have been designed, with different spacing between the coils, for the achievement of two-dimensional magnetic stimulation.

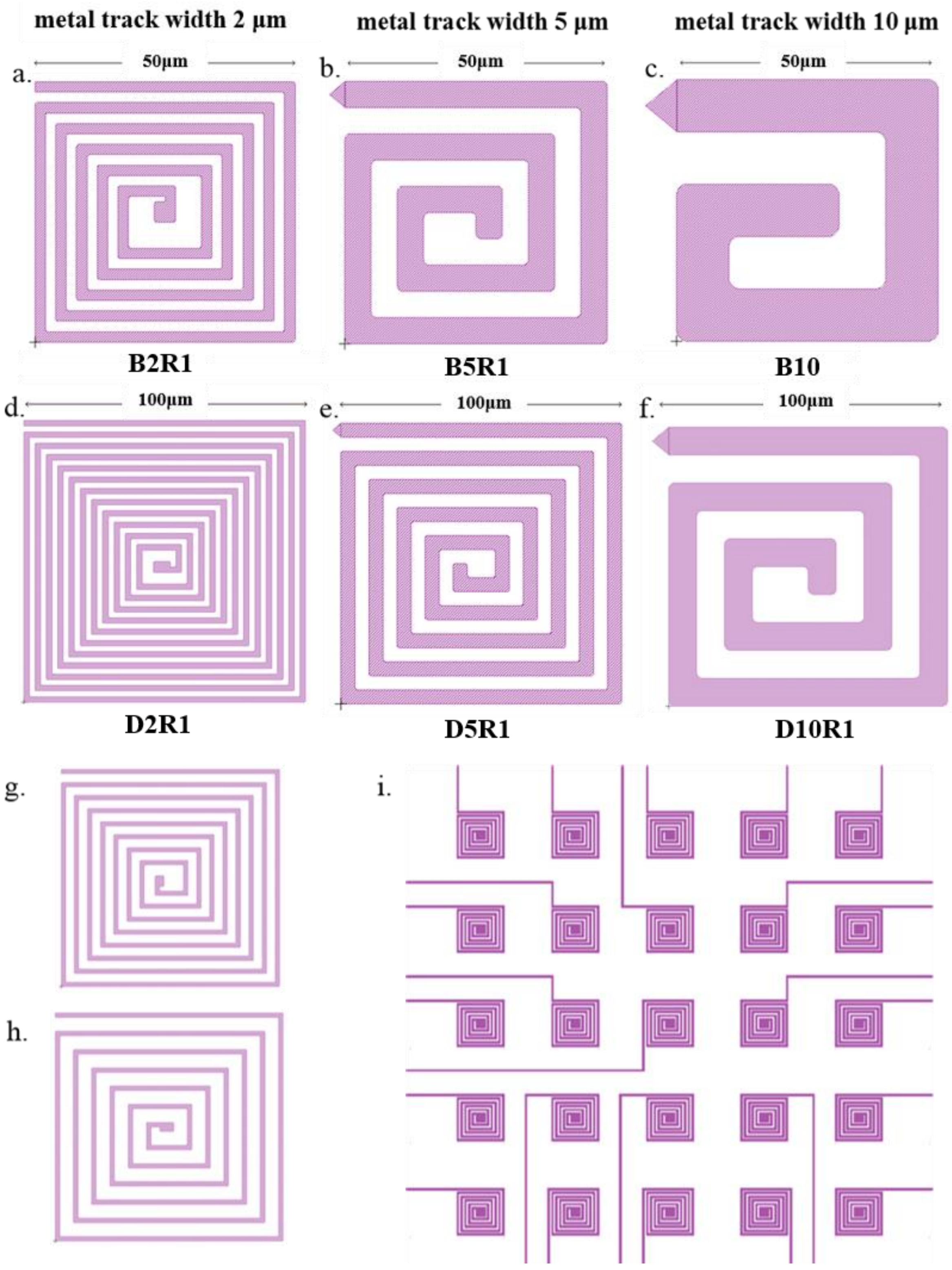

Fig. 4. 12 Different geometries of single and arrays of micro-coils designed in the mask. (a)-(f) Different coil geometries with 1:1 ratio between metal width and spacing. Metal track width differs from: 2µm (a,d) to 5µm (b, e) and 10µm (c, f). (g) A 100µm coil with ratio 1:2 between metal track width and spacing. (h) A 100µm coil with ratio 1:3. (i) A 6x6 array layout.

4.6 Summary

In this chapter a simulations study was presented focusing both on the electrical and electrothermal analysis of the micro-coils. A reference structure was initially presented and two different figures of merit were discussed, namely the magnetic flux density magnitude and the induced electric field in the vicinity of the electromagnet. The magnetic flux density magnitude is used to directly compare the results of the designed geometry to other state-of-the-art planar micro-scale inductors. The magnetic flux density is also used as a figure of merit in a parametric study, which studies the efficiency of the micro-coils for a different set of geometric or experimental characteristics. As expected, the denser structures, are those which produce higher magnetic fields, while the biasing current turned out to be a very important parameter, the increase of which results in an increase on the magnetic field in a linear manner. The amplitude of the biasing current though, cannot be irrationally increased due to thermal deterioration phenomena. Joule heating was tested for the reference structure in a COMSOL Multiphysics model, for a low (20mA) and a high (80mA) current and the differences in the ΔT are presented. Electroplating is suggested as method to increase the cross section of the metallic tracks in a micro-coil by increasing its thickness. Design limitations related to electroplating and other important considerations are finally discussed and lead to the design of the photolithography masks.

Chapter 5

Microfabrication of inductors and platform prototyping

This chapter describes in detail the fabrication procedure of the developed prototypes. Particular emphasis is given on the micro-fabrication techniques used to obtain the chip with the wafer level micro-inductors. Moreover, the packaging of the device and the choice of the appropriate biologically friendly materials to implement the final neuro-stimulation platform are presented in detail. Finally, information is given on the design of a printed circuit board important for the activation circuit and for the individual address of each micro-coil in the array.

5.2 The fabrication process

5.2.1 Fabrication steps

In this subsection, a brief description of the fabrication steps is going to be presented. Electroplating is the preferable technique for increasing the thickness of the micro-coils to the micro-meter scale. The process is carried out using 6 inch wafers. In figure 5.1 which follows, one can see a schematic diagram of the fabrication procedure. The fabrication steps as well as specific parameters related to every different process used are summarized below.

- **Preparation of wafers**

The fabrication procedure starts with the cleaning of the Si wafers. The wafers are placed in acetone for 10 minutes, followed by a 10 minute isopropanol wash. Finally, they are placed in the oven for dehydration for 20 min.

- **Deposition of metal layers with electron beam evaporation**

Deposition of Cr 5nm, Au 50nm and Ti 5nm on a Si substrate. The layer of chromium is used as an adhesion layer between Si and Au, while the titanium layer as an adhesion between Au and the upcoming SiN layer. The seed layer of gold is important for two reasons. Firstly, it would act as a ground plane where the central pads of all the micro-coils are going to be connected, a fact which simplifies the designing process, as now every micro-coil only requires one connection. At the same time it guarantees that all the gold parts would be galvanically connected to the same potential for electroplating, which is crucial for a successful and uniform deposition of metal.

- **Deposition of SiN with reactive sputtering**

The next step is the deposition of a 100nm insulating layer of SiN on top of the metal layers by reactive sputtering (Leybold Optics Helios Sputterer).

- **Optical lithography 1**

The first optical lithography is needed for the opening of the central vias of the micro-coils, which are important for enabling the connection of every coil to the gold ground plane. Also by the first lithography small and large scale ground pads are created in every chip and every period of the wafer respectively. The small ground pads are important for accessing the ground

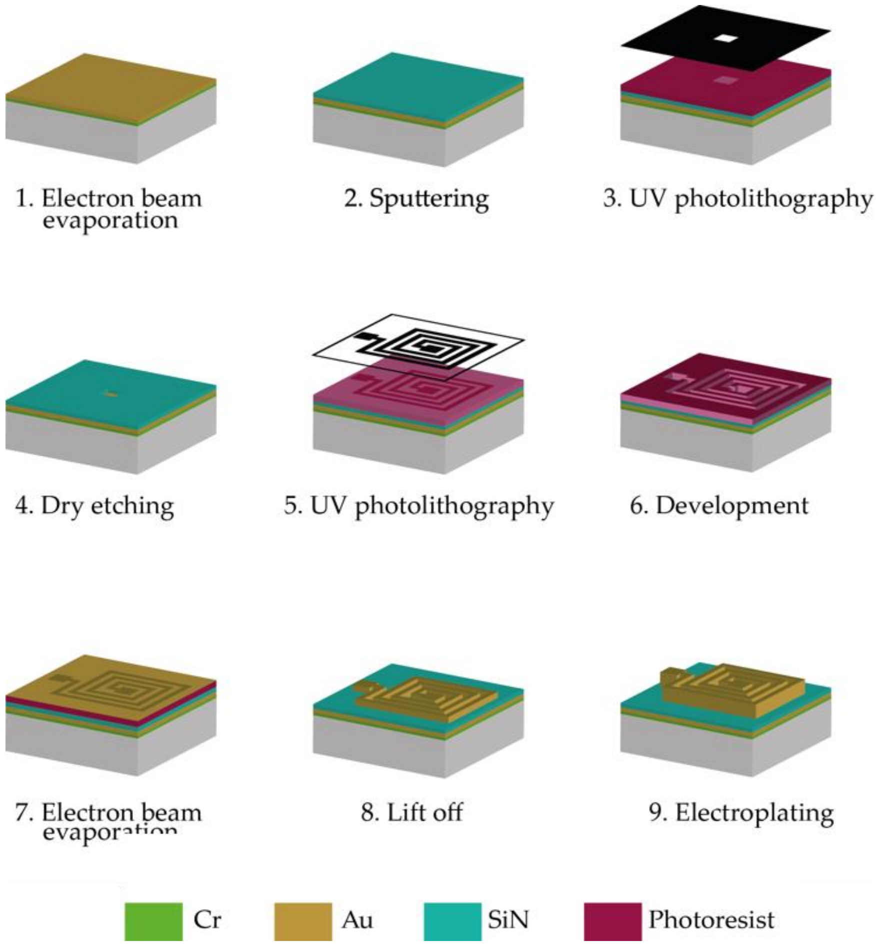

Fig. 5. 1 Schematic graph with the fabrication steps in the development of a micro-coil.

plane in a chip level, while the large ground pads are important for creating a metal contact for electroplating.

- **Removing SiN layer with Inductively Coupled Plasma etching**

After development, the 100nm layer of SiN in the central vias is removed by dry etching using ICP tool (Plasmalab System 100 ICP380). The gases used are SF6 and O_2, with a flow rate of 40sccm and 10sccm respectively. The inductively coupled RF power is set to 1000W and the capacitively coupled RF power is set at 20W. The pressure in the chamber is set to 5mT, the table temperature at 15°C and the helium flow at 18 sccm.

- **Optical lithography 2**

A second optical lithography with the negative photoresist AZ2070 is needed for the patterning of the coil geometries. At this step the biasing pads in the periphery of the chip and the metallic wires which connect the micro-coils to the pads are patterned as well.

- **Descumming**

After development, the resist impurities left in the effective area to be metallized are eliminated by the use of reactive ion etching (RIE80 tool) with an O_2 flow of 100sccm. The RF power is set at 100W and the pressure at 100mT.

- **Metallization with electron beam evaporator and Lift-off**

After cleaning, the samples are ready for metallization with the electron beam evaporator. A 5nm layer of titanium is used again as adhesion layer between the SiN and a new 100nm gold layer on top. The samples are finally left in a bath with NMP overnight for lift off. A sonication bath of 20 sec was also used in an attempt to improve the lift-off result.

- **Electroplating**

The further increase of the micro-coil thickness to the μm scale is achieved by electroplating. The wafers are cut in smaller square pieces after lift-off of a side of 5cm in order to be electroplated with Au. The square dies of Si wafer include a set of the different fabricated micro-magnetic arrays. The anode used is a 6cm side square, with larger surface area than those of each sample. The alignment marks are covered with a non-reactive material so as not to increase in thickness and deform. More details about the electroplating procedure could be found on the next subsection of this chapter.

The procedures were based on the Nanofabrication Facilities in ECS Cleanroom of University of Southampton and are intended to provide a general reference.

5.2.2 Materials for electroplating

The chosen electroplating material is Au, since it is relatively easy to electroplate and at the same time is inert, with no reported biocompatibility issues. Another possible metal candidate for electroplating is Pt. Other materials with better performance were rejected due to different limitations. Ni entails biocompatibility risks and this is the reason why it is avoided even though it is compatible with electroplating. Al cannot be electroplated out of a conventional aqueous plating bath because it is too active. Finally, Ti is also a good candidate and at the same time a biocompatible choice, but is also a metal that cannot be electroplated.

5.2.3 The electroplating setup

In this subsection, the electroplating of Au will be presented, including details concerning the solution, the setup and specific experimental parameters used which assure a good quality of deposition. The solution used for the electroplating of Au is ECF-64D from METALOR Technologies based on ammonium gold sulphite electrolyte, while the basic setup is displayed on figure 5.2. A Pt mesh with surface area 6x6cm^2 is used as an anode, while the sample to be plated has a surface area of 5x5cm^2 and is connected to the cathode. Anode and cathode are placed opposite to one another with their centres at the same height. There is also a reference electrode, in order to complete the three-electrode cell setup. To assure better uniformity the electroplating beaker was placed inside a water bath which was heated to 40^{o}C by a hot plate. In addition, a magnetic stirrer was placed inside the water bath to assist in the most uniform distribution of temperature across the electroplating solution.

In order to have a uniform deposition during electroplating it is essential that the current flow through the solution is kept as steady as possible. This is achieved with the use of a potentiostat, which maintains the potential of the working electrode at a constant level with respect to the reference electrode by adjusting the current at the counter electrode. The potentiostat (Autolab

PGSTAT101) is controlled through Autolab software [115]. After cyclic voltammetry tests, the voltage of -0.325V was chosen in order to achieve a desirable deposition rate of 720nm/h.

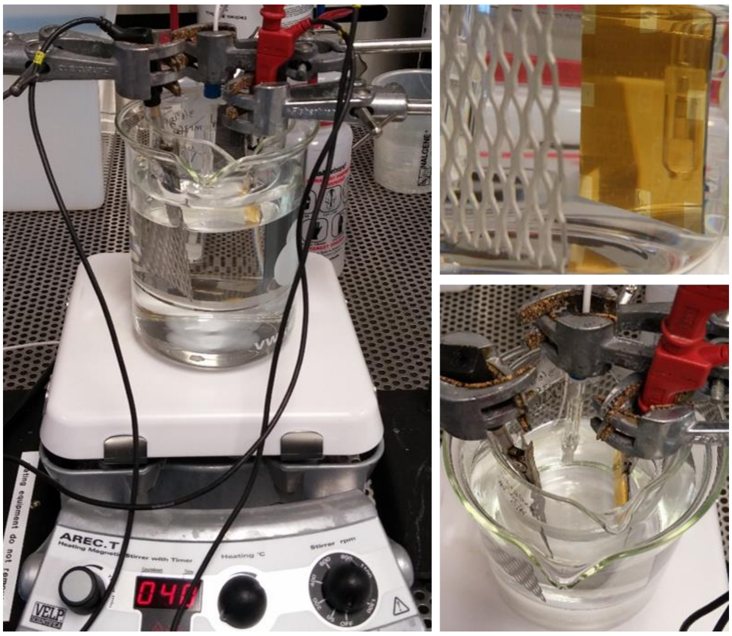

Fig. 5. 2 The electroplating setup used throughout this work. The Pt mesh is used as anode and is placed opposite to the sample which acts as a cathode. In the middle the reference electrode completes the electrochemical cell.

Physical characterisation with a scanning electron microscope just after the electroplating step shows that the deposition of Au is uniform on the micro-coil patterning. Also as expected, the material is symmetrically distributed over the micro-inductors' tracks since no thick resist is used as a patterning mould. This is a limiting factor of the maximum possible thickness of gold to be deposited. As expected, structures with a 1:1 ratio between track width and spacing are mostly affected. Figure 5.3 shows one example of a structure which has been electroplated to a limit that the spacing between the metal tracks is significantly limited. More specifically, Au in a thickness of 2.1μm is electrodeposited on a micro-coil of metal track width and spacing of 5μm. The structure is still functional, but further electrodeposition would lead to spacing merge and consequently to device failure. Being aware of this phenomenon, in case further increase of the thickness will be needed, the second photolithography will be repeated after lift-off, in order to create a mould able to confine the electroplated material.

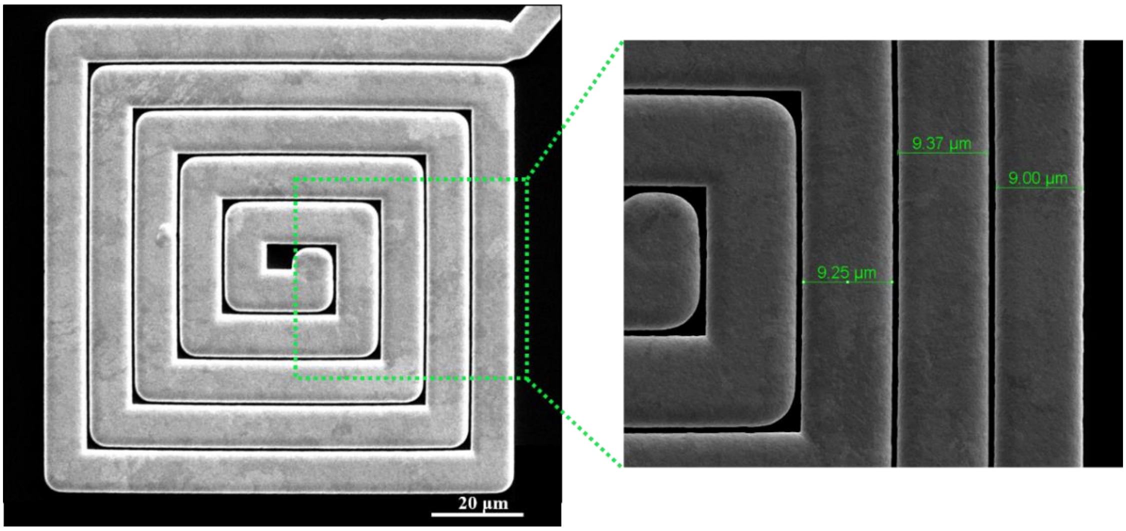

Fig. 5. 3 Example structure where spacing reduction occurs as electroplated gold thickness increases.

5.3 Scanning electron microscopy

Some examples of fabricated samples are presented in the images below taken with a scanning electron microscope (SEM). More specifically, figure 5.4 shows different coil geometries before or after electroplating while figure 5.5 shows examples of micro-coil geometries in array configurations.

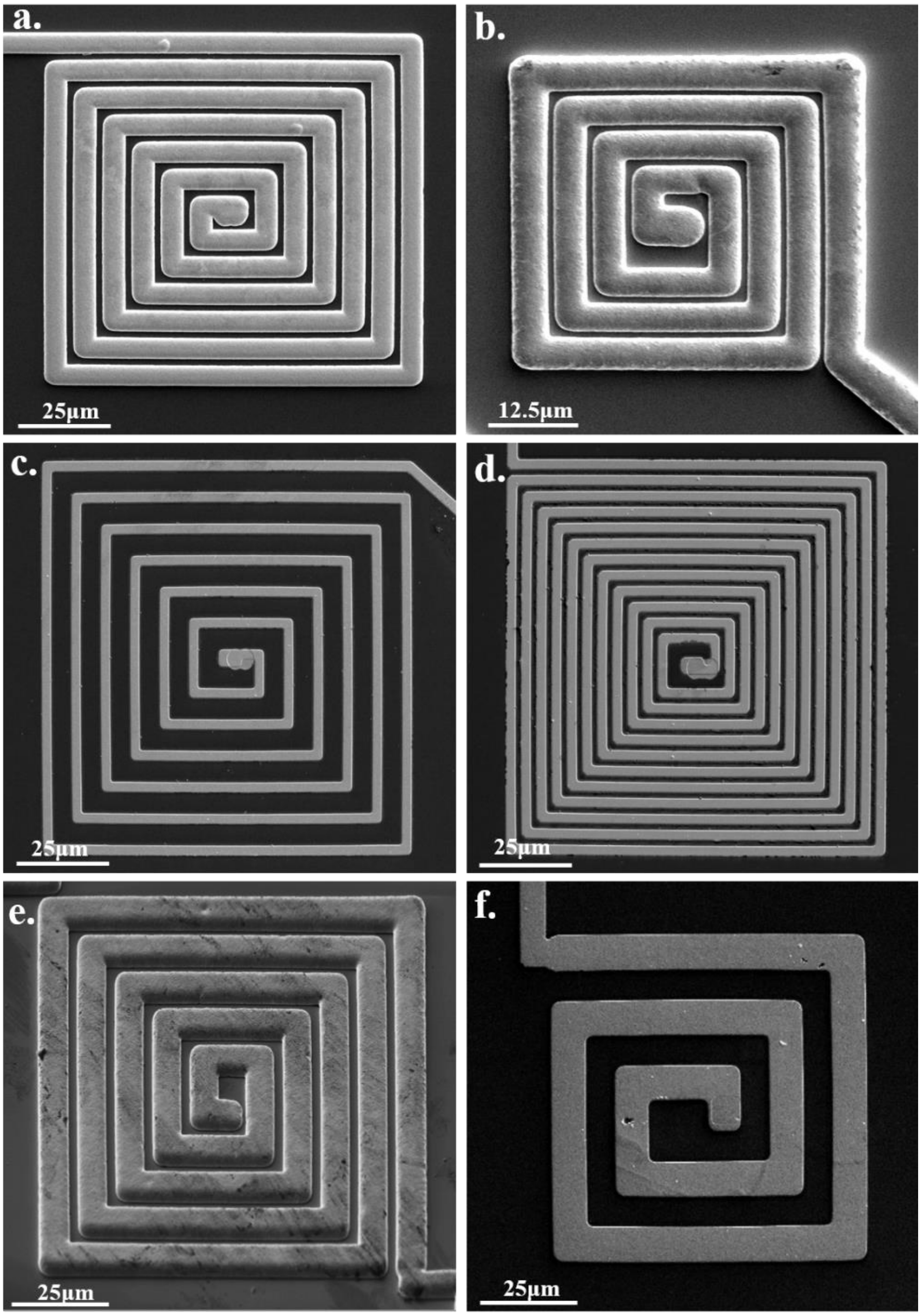

Fig. 5. 4 SEM images of fabricated single coil geometries. (a) Coil of side width 100µm and metal track width 5µm. (b) Coil of side width 500µm and metal track width 5µm (c) Coil of side width 100µm and metal track width 2µm (ratio 1:2). (d) Coil of side width 100µm and metal track width 2µm (ratio 1:1). (e) Coil of side width 100µm and metal track width 5µm. (f) Coil of side width 100µm and metal track width 10µm.

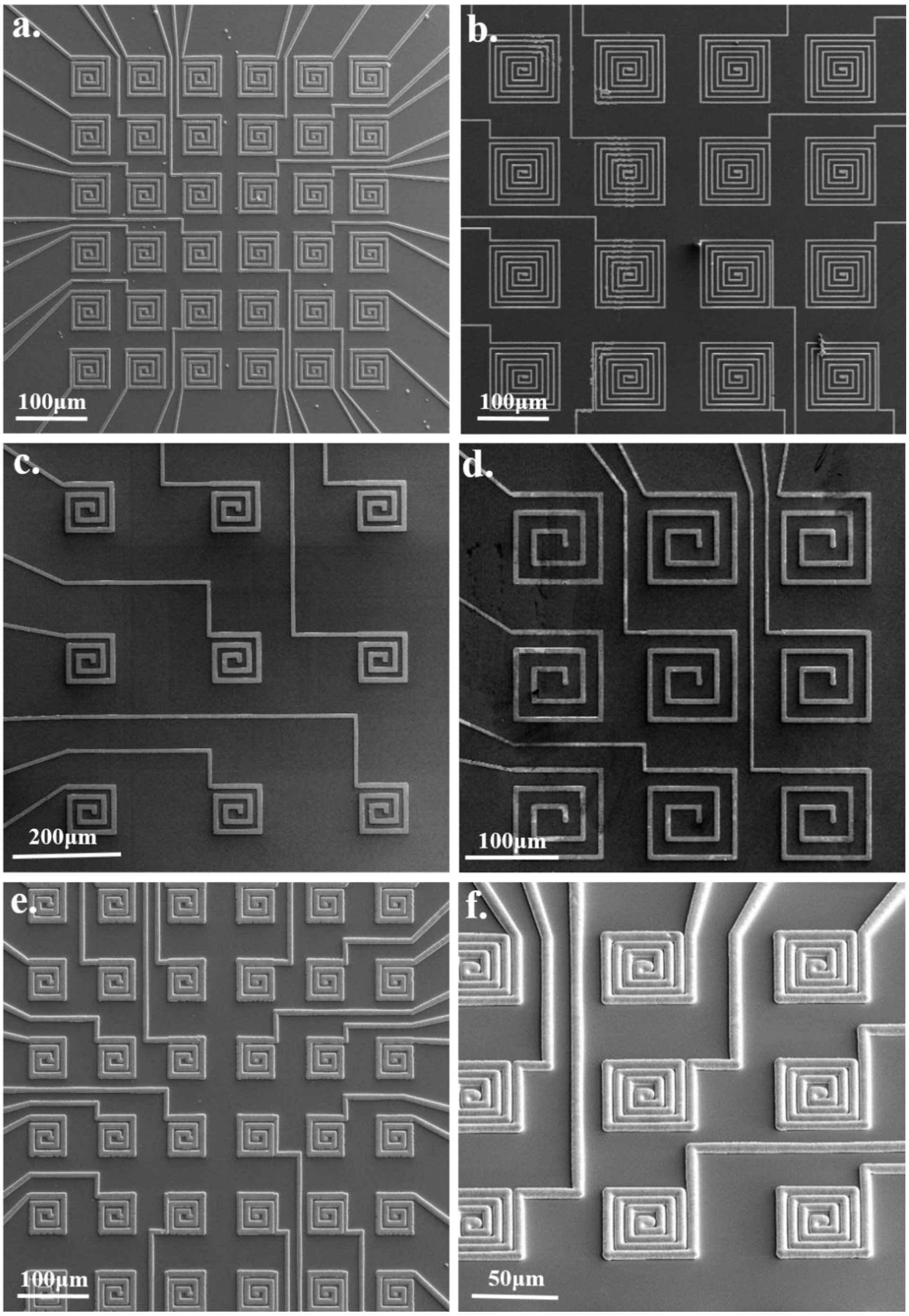

Fig. 5. 5 SEM images of different array configurations. (a) A full array with 36 micro-coils in a square configuration and separation distance between coils at 25µm. (b-f) Zoom into parts of fabricated arrays with different micro-coil geometries and separation distances ranging from 25µm -200µm.

5.4 Development of the neuro-stimulating platform

5.4.1 Bio-compatible packaging

The needs of the bio-experiment demand the encapsulation of the chip into a bio-compatible device. The fabricated wafers are diced into single array chips which are placed and wire-bonded in the packaging. Two package types were used throughout this work. A commercially available package (JCC6840003 by Kyocera Corporation Kyoto) with 64 pins and in the second stage an equivalent package designed in house on a printed circuit board (PCB). The PCB was designed in order to offer a larger effective area for the needs of the bio-experiment and at the same time reduce significantly the cost of each device. Both types of packaging are presented in figure 5.6.

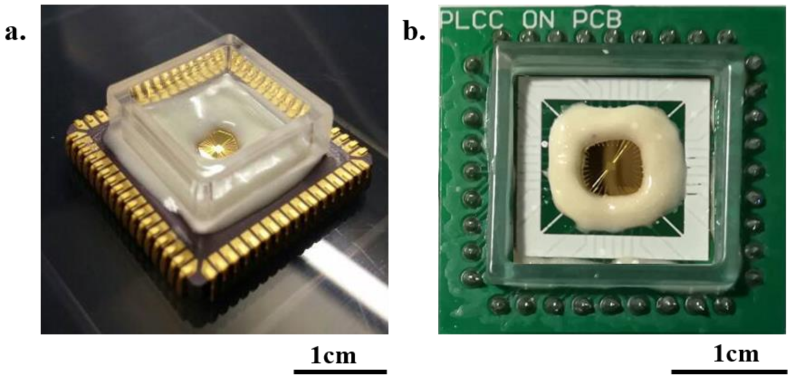

Fig. 5. 6 The packaged device. (a) **On a commercially available package and** (b) **on a PCB.**

In the next step a layer of epoxy was used to cover and protect the wire bonds. Important characteristics of the epoxy are: electric insulation, small thermal coefficient of expansion, good working life and ideally high thermal conductivity. A very important parameter of the epoxy is also its viscosity, as during the deposition of the material over the wire bonds it is crucial that the effective area of micro-coils will remain clear. Ideal candidate was the epoxy adhesive TC-6810 by 3M^{TM} which has a low viscosity of 40,000 - 90,000 cps in base, 11,000 - 21,000 cps in accelerator and 40,000 - 80,000 cps in the mixed solution. The epoxy solidifies after a curing time of 24hours at 23°C. At this stage a cell culture ring is also placed with the use of the epoxy, needed to create a chamber for the cell medium. The cell culture rings were fabricated in house with the use of a 3D-printer or a laser cutter. The geometric characteristics of the ring were chosen based on the necessary cell medium quantity required for a practical cell-culture. These designs were also optimised and re-adjusted after testing with the

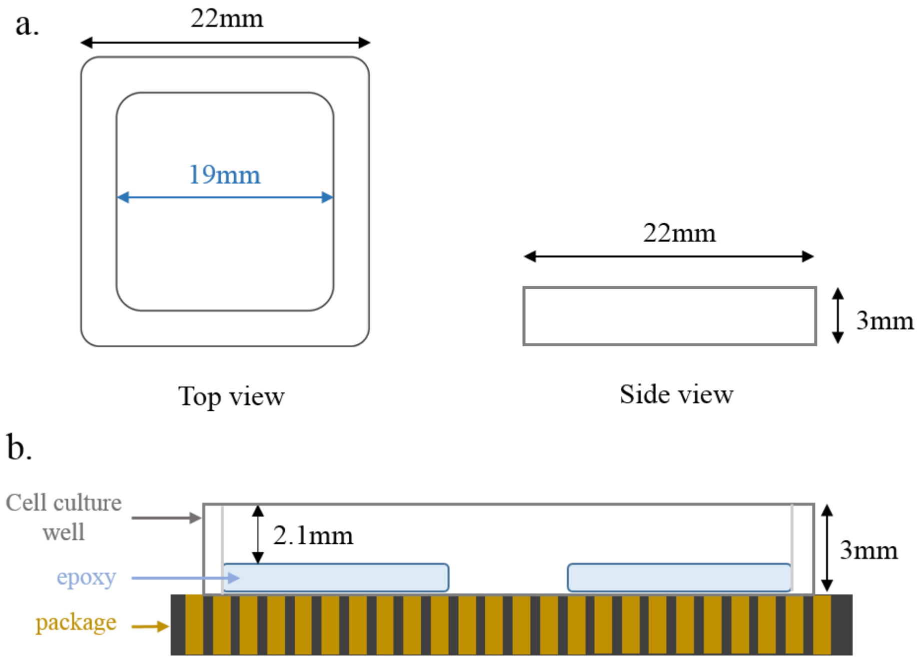

Fig. 5. 7 Geometric characteristics of the cell culturing chamber.

bio-experiment equipment. The final choice in the ring dimensions is illustrated in figure 5.7. After the application of epoxy the whole platform needs to undergo a procedure to become bio-compatible and this is achieved by the deposition of a Parylene-C film. The whole device is inserted in the Parylene coater and a micro-meter thick uniform layer of Parylene-C is deposited. The parts of the packaging that need to remain free of Parylene-C are covered prior to entering the Parylene coater. These parts are involved to the electrical activation of the device in the next step and is important not to be covered with the insulating material to avoid a poor quality contact. In the final step of the procedure the Parylene-C film is treated with a mild O_2 plasma for 30s to become hydrophilic. The hydrophilicity of the film is important for the attachment of the adhesion proteins needed for the cell vitality in a successful culture.

5.4.2 Activation circuit on a PCB

The packaged device is now ready to be mounted into another PCB designed especially for the biasing of the devices. 36 ufl connectors are used for the individual address of each micro-coil. The design of the PCB enables the connection of the ufl connectors to either a commercially available socket (for the JLCC package) or a series of header sockets (for the PCB packaged device). Figure 5.8 shows the top and side view of the printed circuit board for the electric biasing of the PCB packaged devices. Finally, figure 5.9 summarizes the steps towards the development

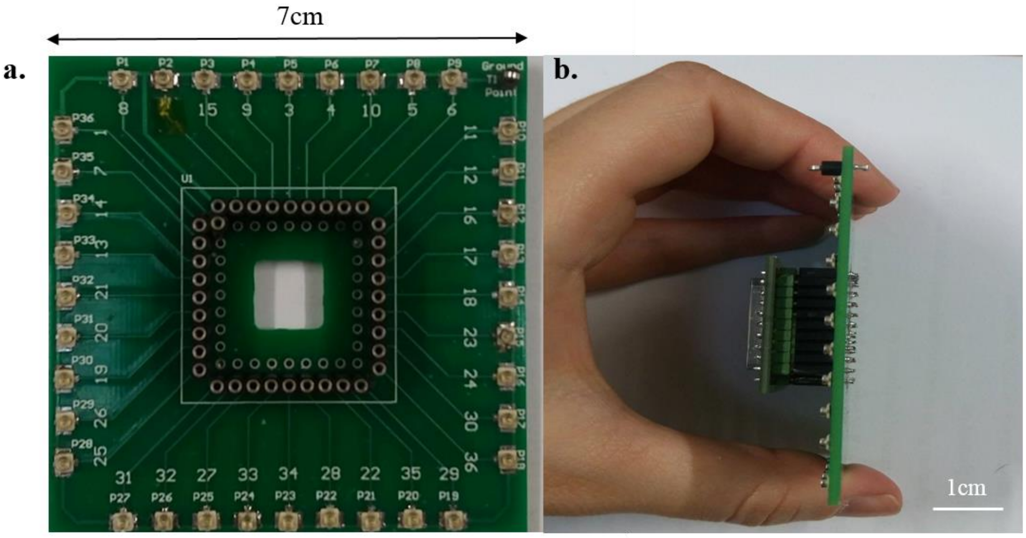

Fig. 5. 8 The PCB designed for biasing. (a) Top view and (b) side view with a mounted device on top.

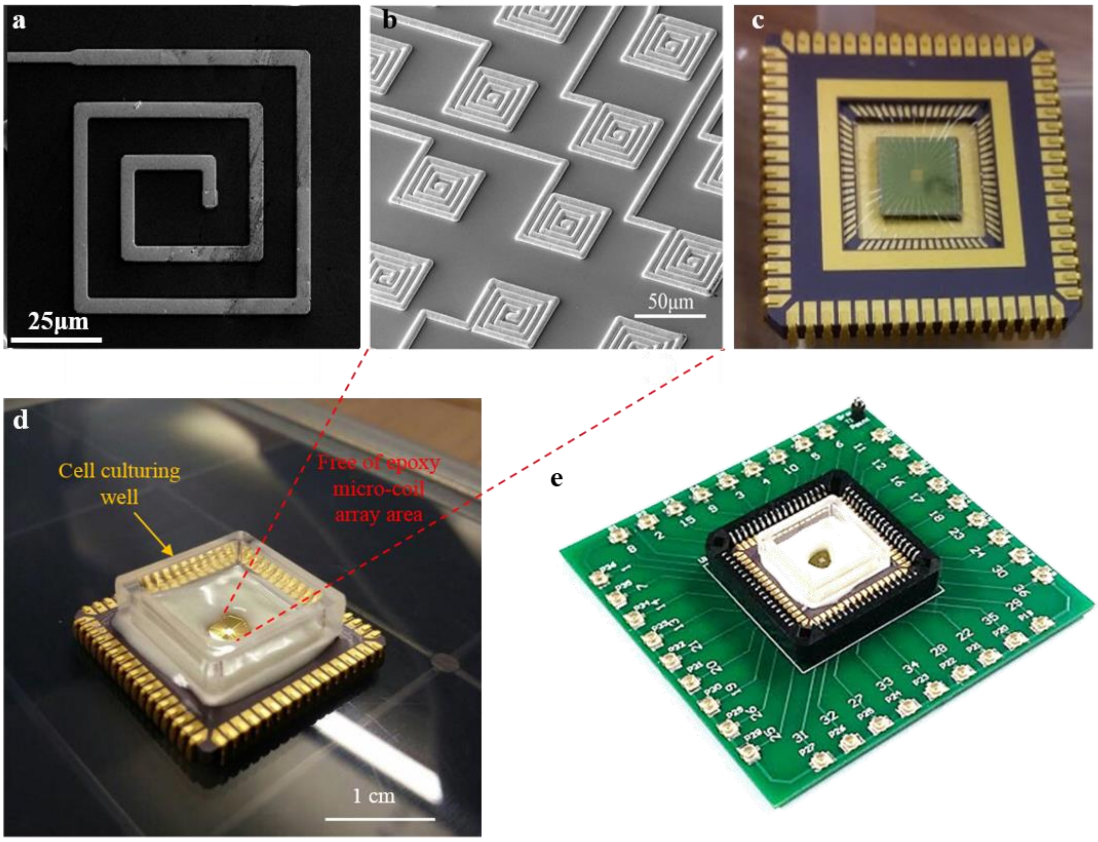

Fig. 5. 9 Steps towards the development of the neuro-stimulating platform. (a) SEM of a micro-coil. (b) The 6x6 array in the chip. (c) Wire bonded chip in the package. (d) Epoxy electrically isolated the wire bonds and cell culturing well. (e) PCB designed for the electrical biasing of each micro-coil.

5.5 Summary

This chapter focused on the prototyping of the micro-magnetic neuro-stimulation platform. Firstly, the micro-fabricating techniques used to obtain planar micro-inductors on chip were presented followed by the steps for the completion of a bio-compatible platform. The final device consists of a chip with 36 separately addressable micro-inductors, in a square array configuration, creating in such a way a non-invasive equivalent of a micro-electrode array. The micro-coils in the arrays create magnetic flux density profiles with micro-scale spatial resolution and are designed for cell morphologies of equivalent size. Characteristics of the alternative designs are also discussed, offering versatility in the effective area of stimulation within the chip, in agreement with the needs of the biological preparations. Finally, the activation circuit designed on a PCB to control the activation of the micro-coils in an array is presented. In the next chapter, the characterization of the fabricated samples will be discussed.

Chapter 6

Electromagnetic and electrothermal benchmarking

This scope of this chapter is to present the electrical characterization performed with a semiconductor parameter analyser to verify the expected inductive behaviour and study the influence of several fabrication parameters, such as the thickness of the electroplated material and the Parylene-C insulating film. A second scope of this chapter, is an electrothermal study, important to define a safe area of operation for the samples and to eliminate the deterioration of the devices due to Joule heating and electromigration phenomena.

6.1 Electrical characterization

One way to characterize fabricated micro-coils on semiconductor substrates is by carrying out an impedance analysis over a frequency range. Prototyped samples were addressed using a set of probe needles and a Keithley Semiconductor Characterization Suite (SCS-4200) for measuring the real and imaginary part (or magnitude and phase) of a complex impedance vector and convert them to the desired useful parameters that describe the system, such as: R, X, L and Q. Useful impedance analysis quantities used throughout this section are the following.

$$\text{Impedance: } Z = \mathrm{R} + \mathrm{iX} = |Z| e^{i\theta} \tag{6.1}$$

$$\text{Resistance: } R = \mathrm{Re}\{Z\} = |Z| \cos\theta \tag{6.2}$$

$$\text{Reactance: } X = \mathrm{Im}\{Z\} = |Z| \sin\theta \tag{6.3}$$

$$\text{Inductance: } L = X/(2\pi f) \tag{6.4}$$

$$\text{Quality factor: } Q = X/R \tag{6.5}$$

It is important to highlight, that the fabrication process as well as the characterization setup adds parasitics that affect both a component's efficiency and the accuracy with which one could determine its resistance, capacitance or inductance. Taking this into consideration, in order to describe the behaviour of a real inductor one should include in the equivalent circuit both a resistor and a capacitor.

Inductors might have capacitive parasitics resulting from the complexity of their structure. A typical equivalent circuit of a real inductor is shown in figure 6.1. R_s represents the losses on the metallic wire, while C_p represents the distributed capacitance between the turns of wire. The complex impedance of the system is given by equation (6.6), while the expected behaviour of both impedance magnitude |Z| and phase θ along with the increase of frequency are also illustrated in figure 6.1.

$$Z = \frac{R_s}{(1-\omega^2 LC)^2 + \omega^2 C^2 R_s^2} + i\frac{\omega L\left(1-\omega^2 LC - \frac{CR_s^2}{L}\right)}{(1-\omega^2 LC)^2 + \omega^2 C^2 R_s^2} \tag{6.6}$$

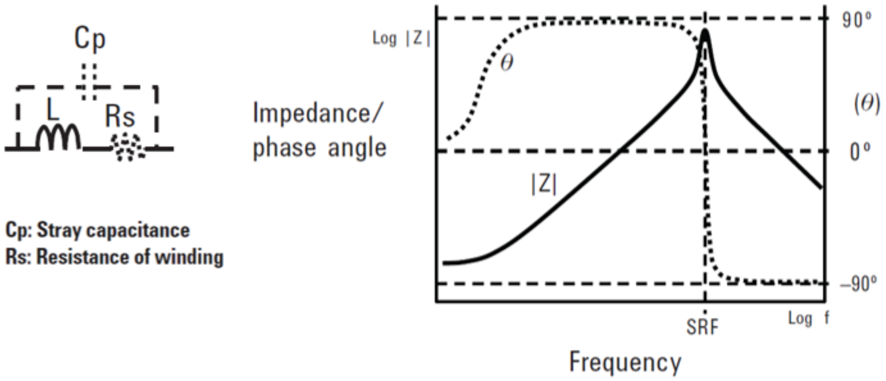

Fig. 6. 1 The equivalent circuit of a real inductor (left). Frequency response of |Z| and θ of a real inductor (right) [116]**.**

The effective inductance L_s of the system is given by equation (6.7). As the frequency increases, inductance also increases, L maximizes at a resonant frequency, while the capacitance behavior of the equivalent circuit becomes dominant above the resonance frequency. After the resonant frequency the measured values of inductance are negative, corresponding to capacitive behavior. The behavior of the effective inductance of the system is illustrated in figure 6.2.

$$L_s = \frac{X}{\omega} = \frac{L\left(1-\omega^2 LC - \frac{CR_s^2}{L}\right)}{(1-\omega^2 LC)^2 + \omega^2 C^2 R_s^2} \tag{6.7}$$

It is also expected that assuming low values of parasitic capacitance and resistance, the effective inductance L_s is getting closer to the ideal inductance L.

$$\text{When } \omega^2 C^2 R_s^2 << 1 \text{ and } \frac{CR_s^2}{L} << 1 \Rightarrow L_s \cong \frac{L}{1-\omega^2 LC} \qquad (6.8)$$

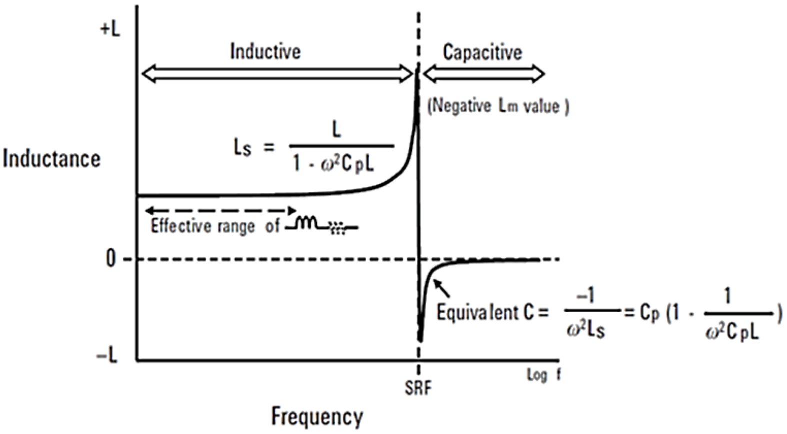

Fig. 6. 2 The behavior of inductance along with the increase of frequency in a real inductor [116]**.**

In the following subsections the results of the electrical characterization of the fabricated micro-coils are presented, covering a study of different parameters. An impedance frequency sweep of different geometries is presented to test the behavior of the micro-coils. Following to this, testing of one structure at different electrodeposited thickness is performed. Finally, the influence of the coating layer will be examined. The geometric characteristics of the fabricated structures under study are presented in table 6.1. The number of turns is a result of the coil size, the wire width and the spacing between the turns.

Table 6.1 The geometric characteristics of the fabricated micro-coils.

Structure	Coil side (µm)	Wire width (µm)	Spacing between turns (µm)	Number of turns
B2R1	50	2	2	5
D2R1	100	2	2	12
B5R1	50	5	5	3
D5R1	100	5	5	5
B10	50	10	10	1
D10R1	100	10	10	3

6.1.1 Impedance frequency sweep

The structures under study were electroplated to the thickness of 1.8μm. The samples were biased with AC voltage (rms) of 100mV while the frequency range covered was from 500kHz to 10MHz (the range of semiconductor parameter analyser). The rms value of the test signal was chosen at 100mV based on typical test options in the semiconductor parameter analyser. The results for the structures with coil thickness of 1.8μm are summarised in the plots below.

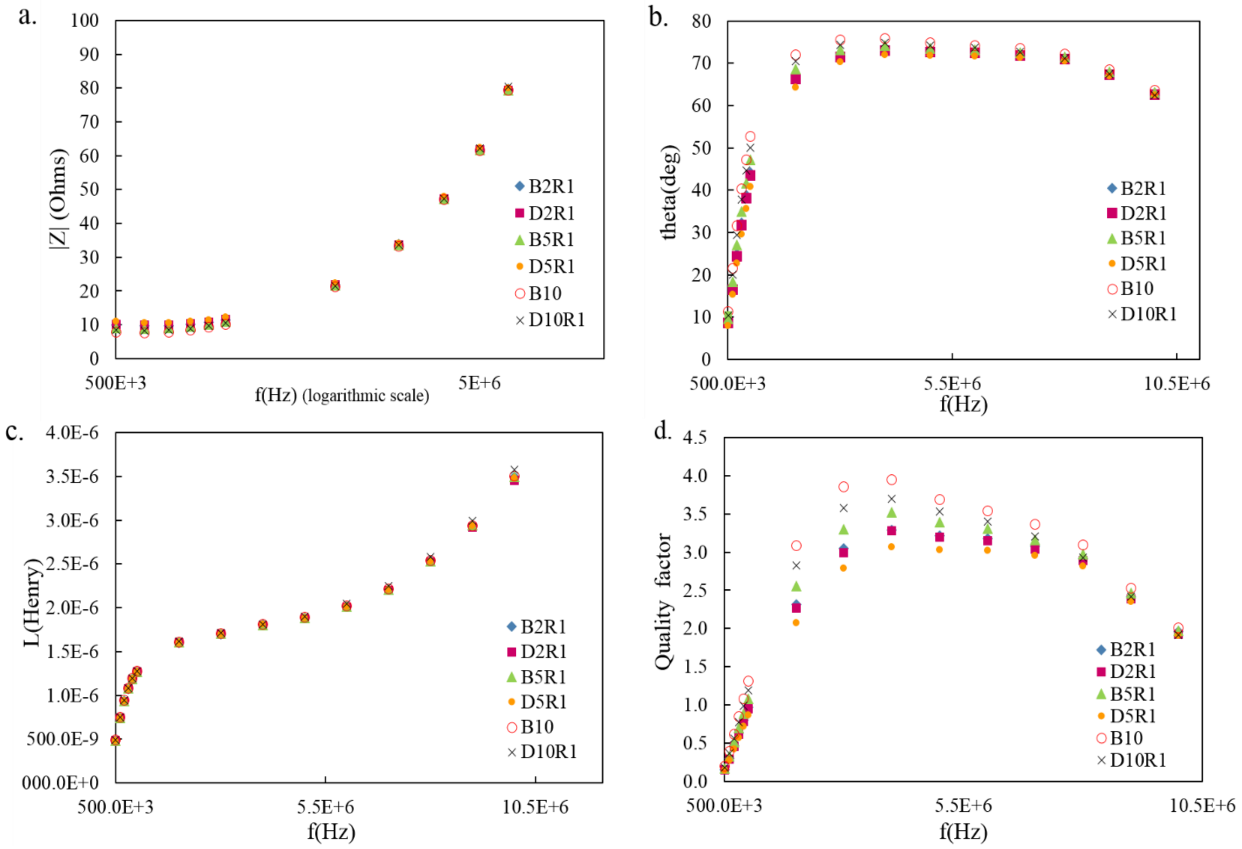

Fig. 6. 3 Impedance frequency sweep for the geometries of table 6.1. Presented: (a) impedance amplitude, (b) phase, (c) inductance and (d) quality factor of geometries.

a) Impedance magnitude and phase

The first level of comparison concerns the behaviour of Z magnitude and phase along with the increase of the signal frequency. The frequency range is from 500kHz to 10MHz. For the frequency range covered by the employed semiconductor analyser, one could see that there is no resonance. By a more careful observation of the phase to frequency graph 6.5b, theta is slightly decreasing in the higher frequency range and comparing the behaviour of the devices to the expected behaviour in figure 6.3, it could be assumed that even though the resonance is not obvious, it should be at a frequency close to 10MHz.As a result, the system is away from the resonance and shows an inductive behaviour at almost all the frequency range covered. The capacitive behaviour will become dominant at higher frequencies, out of our interests, as the micro-inductor will be used in the kHz range and lower. The complex impedance of the different structures shows a dispersion in the low frequency range, while as the frequency increases and above the 4MHz the magnitude of Z is reaching the same value for all the structures. The increase of |Z| by the increase of frequency is logical as both X and R increase by frequency and $|Z| = \sqrt{R^2 + X^2}$.

- **Increase of R:** The skin effect leads to the raising of an inductor's resistance as the frequency increases. The skin effect results from the tendency of an alternating current to flow through the outer areas of a conductor rather than through the middle. This has the effect of reducing the cross-sectional area of the conductor through which the current can flow, thereby effectively increasing its resistance. It is found that the skin effect becomes more pronounced with increasing frequency.
- **Increase of X:** Reactance is increased by the frequency because of the behaviour of an inductor to produce a voltage drop at its edges analogous to the change of the current flowing through it. This dependency on the time derivative of current is translated in the frequency domain as a linear relationship between X and f.

b) Inductance

The inductance is calculated by the equation (6.4). Figure 6.3 c shows that the structures are having very similar values of inductance over the whole frequency range. This is happening because the different structures behave almost identically in terms of reactance X. One reason which could explain this behavior, is the effect of the ground plane which could act as a series inductance which is dominating and improves the results. However, the influence of the ground plane, which is in contact with one end of the coil is something which should be further investigated.

c) Quality factor

The quality factor is a measure of reactance purity. The Q is measured as the ratio of the energy stored in a component to the energy dissipated by the component. Since Q is calculated by the ratio X/R and X is almost similar for all the structures, the higher values of quality factor are achieved for the structures that have lower losses/real resistance. As a result, coils with larger wire width (larger cross section) exhibit higher values of quality factors. The higher values of quality factor (2 to 4) are apparent at about 3.5MHz for the majority of the structures.

6.1.2 The influence of the metal thickness

In this subsection the comparison between structures of different thicknesses will be analysed. For simplicity, only the comparison of different thicknesses of one of the most efficient structures will be presented here. Specifically, the focus is on structure D2R1 which has the more number of turns in comparison to other fabricated samples and is expected to create the highest magnitude of magnetic field. An additional second lithography is repeated, as described in section 3.2.3 to avoid the limiting effect of electroplating.

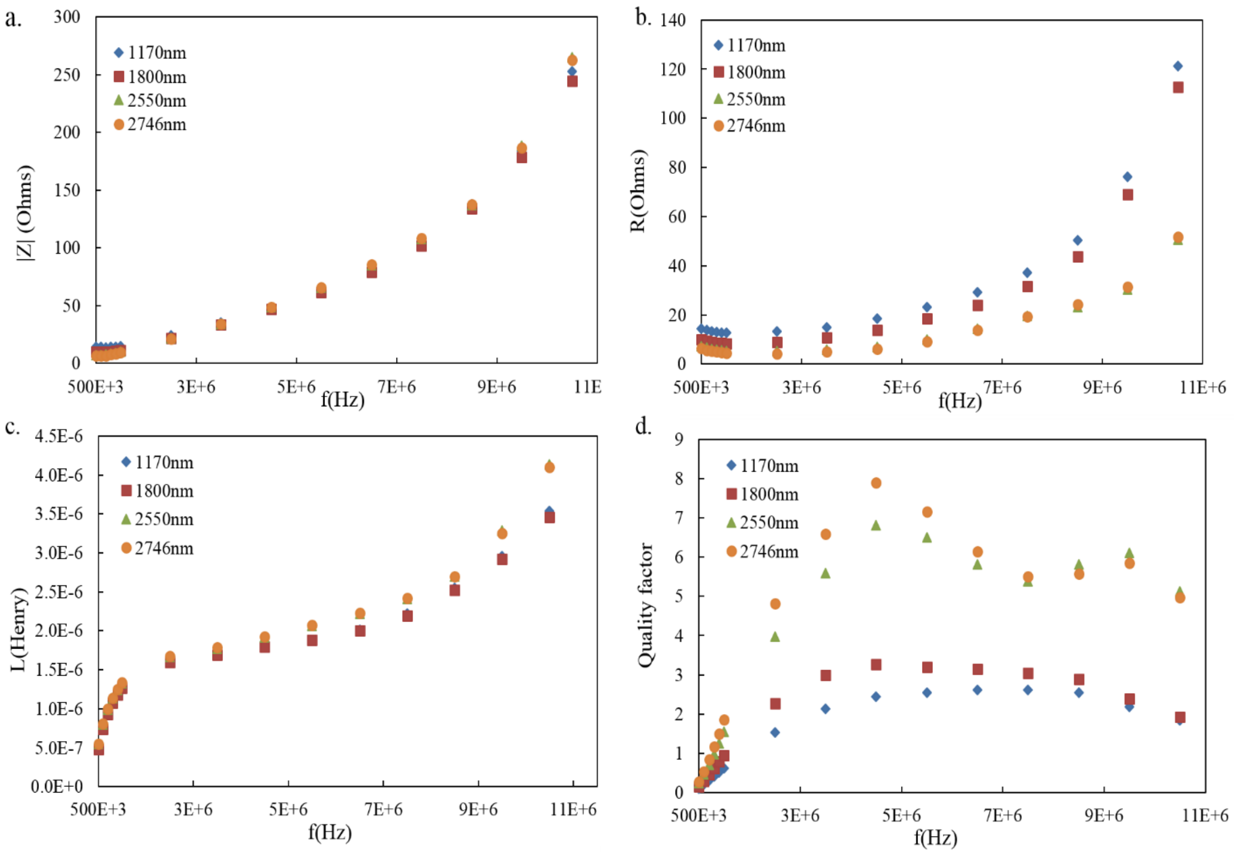

Fig. 6. 4 Comparison of (a) impedance magnitude, (b) resistance, (c) inductance and (d) quality factor of geometry D2R1 for four different thicknesses of electrodeposited gold.

The micro-coil geometries were tested for a set of 4 different thicknesses: 1170nm, 1800nm, 2550nm and 2746nm and the results are presented in figure 6.4. As expected, the structures which show lower values of resistance are those of higher thicknesses as the same amount of current has a wider cross section in the metal track to flow. At the same time no significant differences are noticed in the inductance of the different micro-coils and this is because the inductance is depending mainly on other geometric parameters that are the same for all the D2R1 micro-coils. The quality factor of the thicker micro-coils is more than doubled and this improved result is again expected from equation (6.5) and the fact that both the resistance is decreasing and reactance is increasing along with the increase of the micro-coils' thickness.

6.1.3 The influence of the coating layer

Another set of measurements was performed in an attempt to identify the influence of the coating layer that is utilized as passivation layer but also adhesive layer for the cells. Until now, all the devices under test have been coated by a thin layer of Parylene-C. The coating is conformal with a thickness of 1μm. For simplicity, the results illustrated below in figure 6.5 concern again the most efficient of the structures, D2R1, for micro-coils' metal thickness of 1800nm. After the addition of the coating Parylene-C layer, the values of impedance are slightly deteriorated. However, the fact that this decrease is so low has to do both with the thin layer of the polymer used and the fact that Parylene-C is a very good dielectric, with a very low expected current leakage. The same measurements were performed for several different geometries and the behaviour was similar to the observed result displayed above.

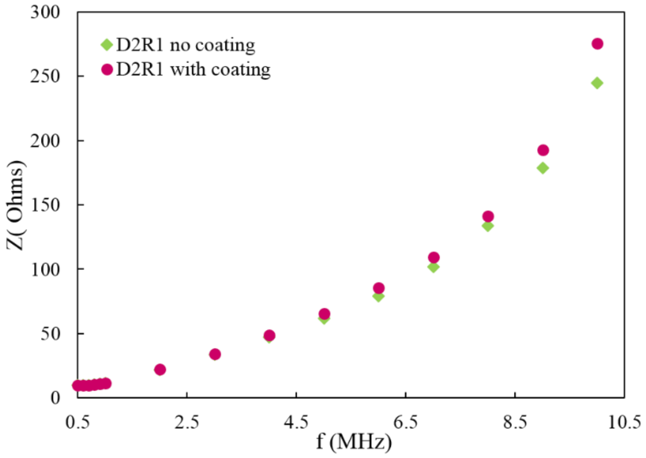

Fig. 6. 5 Comparison of impedance of micro-coil geometry D2R1 along with the increase of the biasing frequency, with and without a Parylene-C coating layer of 1μm.

6.2 Electrothermal characterization

The electric performance of all micro-scale electromagnetic components is hampered by two dominant factors: Joule heating and electromigration. The scope of this study was to evaluate how these phenomena change the electric behaviour of the samples during activation. A safe area of operation across six types of samples with different geometric characteristics was experimentally defined and their equivalent thermal resistance were compared. Finally, useful information for the reliability of the samples was extracted by comparing their median failure times. The findings present the activation restrictions which should be taken into account in order to avoid the thermal degradation of the components, while at the same time could be used as design guidelines for similar geometries.

In vitro implementation of TMS demands a size of the inductor comparable to the size of the target cell, to assure a high spatial resolution and a localised region of activation. Up to now however, the inductors used were in the submillimetre scale as it is a challenge to achieve high spatial resolution and sufficient current capacity to trigger the cell activity without electrothermally wearing out the inductors. The efficiency of a micro-magnetic stimulator to elicit cellular activity is defined by the geometric characteristics of the structure, the relative distance between the micro-inductor and a cell and by the maximum amplitude of the input current to the device.

Thermal and mechanical effects, such as Joule heating and electromigration, limit the performance of inductors especially when the cross section of the metallic components is decreasing to ~10μm^2. The thermal degradation of planar micro-inductors has been studied both experimentally [106], to identify the influence of the different substrates on the heat dissipation mechanism and numerically [45], in CMOS based inductors. The impact of these phenomena has been extensively studied on systems of very-large-scale integration (VLSI) interconnects. More specifically, the flow of current through a metal conductor either for biasing or signal transmission purposes, is a means of power distribution to the system. However, a number of physical mechanisms transform the electrical power into thermal, influencing the design and reliability of the system. Circuit designers of large scale interconnect systems set restrictions to the maximum current density flowing into the system to minimise as much as possible the increase of the temperature. [117]–[122].

For a time dependant current density j(t), two different quantities are involved in the deterioration mechanisms. The j_{rms} value is involved in the self-heating of the micro-coils, due to Joule heating, while the j_{avg} value is the involved in the EM mechanism [123]. Joule heating is a major issue of temperature increase in a metal and is described by equation (6.9).

$$\Delta \mathrm{T}_{Joule\ heating} = T_m - T_{amb} = \mathrm{I}^2_{rms}\ \mathrm{R}\,\mathrm{R}_{th} \tag{6.9}$$

T_m is the metal temperature, T_{amb} is the initial reference temperature, I_{rms} is the rms value of the flowing current, R is the electric resistance and finally R_{th} is the equivalent thermal resistance.

Electromigration is another temperature dependent phenomenon related to the mass transfer (metal atoms) due to high stress created as the current density increases. The main cause of the metal atoms' mechanical movement is the momentum transfer from the electron wind. In some cases, the failure and damage caused are irreversible due to openings and loss of metal continuity. The phenomenon is more significant for DC currents, rather than AC currents of same magnitude. The median time to fail (MTF) in hours [124] is given by Black's Law in equation (6.10).

$$MTF = \frac{A}{\mathrm{C}\,J^n}\ \mathrm{e}^{\frac{E_B}{kT_m}} \tag{6.10}$$

Where A is the cross section, C is a constant depending the micro-structure of the deposited material, J is either the DC or average density in A/cm^2, n typically lies between 1-2, E_B is the activation energy in eV, k is the Boltzmann constant and T_m the temperature of the metal in degrees Kelvin.

The development of a neuro-stimulating tool able to work over a wide range of biological preparations and morphologies requires well defined limits of safe operation to add an additional level of control to the experiments. The activation limits of the inductors were tested, so as to define the maximum current density they could hold and discussion is triggered on considerations which should be taken into account in the design of similar type of electromagnets. The proposed chip for magnetic stimulation of neural cells in vitro consists of 36 micro-inductors in a square array and is developed with standard micro-fabrication techniques. Six different geometries are studied, all of which with a side width of 100μm, but with differences in the metal track width and thickness.

6.2.1 Measurement procedure

The measuring procedure followed involves a DC current set as an input, with a constantly increasing amplitude from 1-100mA. Between each amplitude step and after a significant time waited for thermal equilibrium, another DC value of lower amplitude is applied, at 1mA, representing a measurement in a colder state of a micro-coil. All the measurements were performed with a current list sweep on Keithley 4200 SCS, in a pulsed mode, where the duration of the ON and OFF phases of each pulse lasted 100ms and 1s respectively. The choice of 1s as a safe time for the system to reach equilibrium was tested prior to the actual experiment, with some parametric testing. Since the time constant of the system was not known, the initial measurements started with a current list sweep with 10ms of pulses followed by 10s of rest. The measurements were compared with pulses of 10ms followed by 5s of rest and finally 10ms on and 1s of rest. Since no significant differences were observed in the behaviour of the samples in the different cases, 1s was considered as a safe limit for the system to reach equilibrium and study the steady state. Both a forth and back pulse sweep were tried, as part of the experiment standardisation in the first steps of the study. For measurements below the deterioration limit, no non-linear effect was observed and this is why it was decided to focus on measurements of increasing amplitude pulses only. Above the deterioration limit, the backward measurements (especially of R_{cold}) became more random, a fact which was considered as an indication of deterioration of the device.

The settings are chosen to be equivalent to those needed in a realistic scenario of excitable cells' excitation. The rms values of the current density are determined by the choice of the specific duty cycle (10%), which is based on the worst case scenario of a realistic activation scheme. Keeping a record of the resistance in the hot and cold states of the micro-coils leads to the calculation of T_{hot} and T_{cold} values in every step and to the final plotting of the injected and dissipated power by the micro-coils over temperature. The measurements at a low current give the resistance at a cold state, while the measurements at high currents give the resistance at a hot state. The current of cold states remains constant at 1mA, while the current of hot states is increasing by 1mA between two consecutive measurements up to the value of 100mA.

Specifically, T_{hot} and T_{cold} are calculated from equations (6.11) and (6.12) at every measurement point. The DC resistance of the inductor is given by equation (6.11), where ρ_T is the electric resistivity of the material, l is the total length and S the surface which corresponds to the cross section of the metallic track.

$$R = \rho_{\mathrm{T}} \frac{l}{S} \tag{6.11}$$

The electric resistivity ρ_T depends on the temperature in a linear manner, as expressed by equation (6.12). P_{Tamb} is the resistivity at ambient temperature with a value of 2.44 10^{-8} Ohm·m for gold and a_{th} is a temperature coefficient, which for gold has the value of $0.0034K^{-1}$.

$$\rho_T = \rho_{T_{amb}} \left(1 + \alpha_{th} \left(T - T_{amb}\right)\right) \tag{6.12}$$

The measurements are performed with a 2 probe setup. One SMU in current mode feeding the inductor through the biasing pad and the other SMU forcing a reference zero potential in the ground pad (current list sweep in pulsed mode).

6.2.2 Effects of Joule heating in electric resistance

The deterioration points of the six different geometries are illustrated on figure 6.6 a, b. Samples I-III are geometries with different track width from a die with thickness 1.95μm, while IV-VI are similar geometries with lower thickness, 0.9μm. The geometric characteristics of the samples are summarized in table 6.2. Every two measurements (one hot at different current and one cold constantly at 1mA) the biasing current increases by 1mA. For each coil, the upper and lower set of measurements correspond to the hot and cold measurements respectively. The resistance is plotted along the number of measurements, so as to illustrate clearly the behaviour of the resistance at the colder states. However it remains easy to correlate each number of hot measurement to the current flowing through the micro-coil, since: I(mA)=#measurement/2+0.5. In other words, every two measurements (1 cold and 1 hot) we increase the current on the device by 1mA. The deterioration point is defined as the point where a sharp increase in the cold state (always measured at 1mA) is observed, as this indicates a failing mechanism in the metal track (e.g. change in the geometric characteristics of the cross section). For example, coil I has a deterioration point at #measurement 89, which corresponds to I(mA)=89/2+0.5=45mA. Samples III and VI, have a deterioration limit at current amplitudes greater than the maximum 99mA tested. The resistance is extracted based on measurements of two different micro-coils of the same geometry.

Table 6.2 Geometric characteristics, electric resistance and current (peak values) at deterioration point of the geometries under study.

Sample	Thickness (μm)	Width (μm)	R_{calc} (Ω)	$R_{cold\text{-}meas} \pm \delta R_{cold\text{-}meas}$ (Ω)	I_{det}(mA)
I	1.95	5.9	8.16	7.85 ± 2.53	45
II	1.95	8.9	4.32	6.04 ± 2.50	80
III	1.95	13.9	3.69	5.56 ± 2.15	>99
IV	0.90	3.8	25.72	30.17 ± 4.73	24
V	0.90	6.8	11.93	27.20 ± 6.67	40
VI	0.90	11.8	6.61	14.03 ± 4.27	>99

As expected the smaller the metallic track cross section of a micro-coil, the lower the current at which the degradation occurs. This is obvious either by comparing different geometries on the same thickness (eg. samples I-III versus IV-VI), or same geometries over different thickness (eg. samples I versus IV). The behaviour of sample IV is showing the expected behaviour with some more stochasticity, which could be attributed to the fact that it is the most sensitive geometry. Sample IV has the smallest cross section in comparison to the rest of the samples.

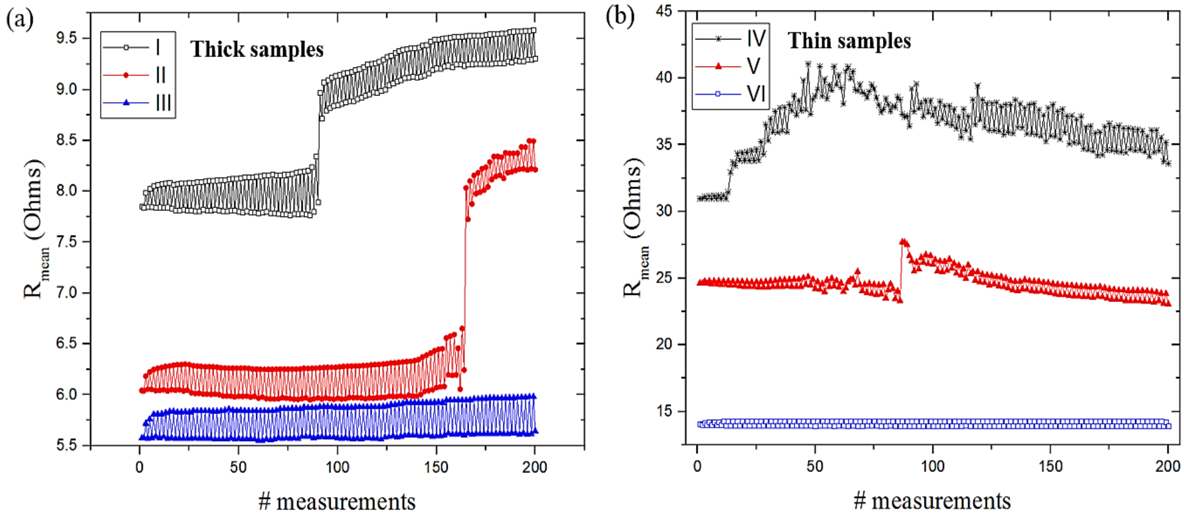

Fig. 6. 6 Thermal degradation of micro-coils, given by a steep increase in resistance as the current increases. (a) Samples I-III with a thickness of 1.95μm and (b) Samples IV-VI with a thickness of 0.9μm.

The values of resistance before starting the current sweep, are also presented in table 6.2, along with their expected values, which were calculated analytically. The value of the resistance arises from the micro-coil resistance, which is standard for all micro-coils in an array, plus some additional factors such as the resistance from the thin wire which connects the coil to the pad and the resistance due to the ground plane. Part of the thin wire geometries are illustrated in figure 5.5. The thin wire has a mean length value of 2000μm and differs up to ≈300μm between different coils within the same array. In the case of an electrodeposited layer of Au with a thickness of 1.95μm, this is translated as an additional resistance in the order of 0.62Ohms/100μm. This creates a systematic error which is taken into account on the estimation of the resistance uncertainty. For the calculation of the ground plane resistance equation (6.13) was used, where R_s is the sheet resistance of the ground plane 488mOhm/sq, d is the distance between the inductor via to substrate and the actual ground pad and α is the radius of the electrodes.

The value of the resistance arises from the micro-coil resistance, which is standard for all micro-coils in an array, plus some additional factors. The additional factors are a resistance from the thin wire which connects the coil to the pad and the resistance due to the ground plane. The thin wire has a mean length value of 2000μm and differs up to ≈300μm between different coils within the same array. In the case of an electrodeposited layer of Au with a thickness of 1.95μm, this is translated as an additional resistance in the order of 0.62Ohms/100μm

$$R = \frac{R_s}{\pi} \cdot \alpha \cosh\left(\frac{d}{2a}\right) \tag{6.13}$$

The $\delta R_{\text{cold-meas}}$ error includes both the standard error of two measurements in different coils of same type and also a systematic factor arising from the thin wire difference in length.

6.2.3 Heat transfer mechanisms

In this subsection discussion of the heat dissipation mechanisms which occur in the samples are discussed. Figure 6.7 shows the temperature power plot, with results of both thick and thin structures. The power is calculated from the measured voltage and current values and is plotted up to 75mW. Electric energy is converted to thermal energy and the non-linear behaviour of the graph indicates that thermal conduction is not the only dissipation mechanism. If thermal conduction was the only heat transfer mechanism this graph would show a linear dependency between temperature and power, with the slope giving the thermal resistance of the structure. Heat transfer by convection is also occurring, while heat transfer by radiation is not very likely due to the low emissivity coefficient of the gold.

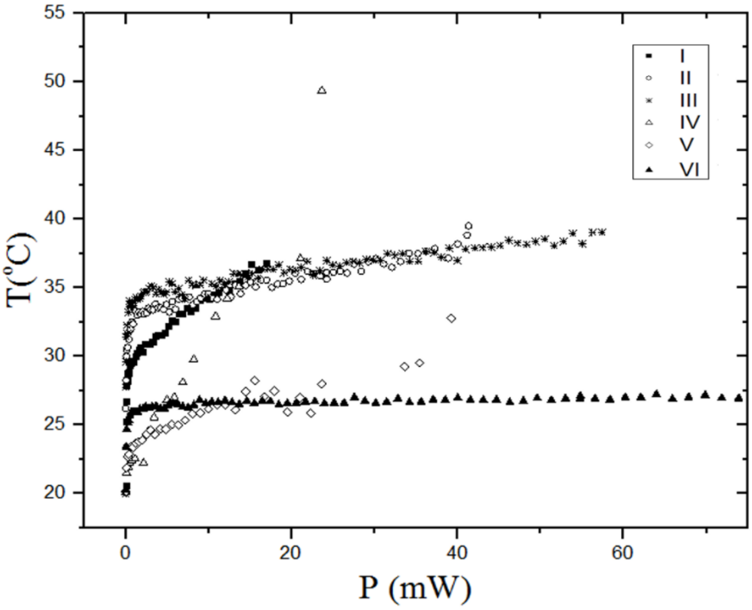

Fig. 6. 7 Temperature over applied power for the six geometries.

6.2.4 Maximum current density in the deterioration point

The rms current density up to the deterioration point of each sample is presented in figure 6.8. A linear fit of the deterioration points of the structures, illustrated as red full circles in figure 6.8, is giving a relation between the maximum current density flowing to the different geometries and the deterioration temperature. The extrapolated relation is the (6.14).

$$J_{rms|\det}\left(\frac{mA}{\mu m^2}\right) = -\,0.133T_{\det}\left({}^{o}C\right) + 6.345 \tag{6.14}$$

Sample IV was excluded from the fit, so as to obtain a more accurate result. Being the most sensitive sample, in the sense of thiner cross section, has the most unstable and noisy behaviour between all samples especially as it approaches the deterioration point. This is also obvious from figure 6.6b. Figure 6.8 and relation (6.14), provide key information for the design of micro-inductors as inductive components or heating elements.

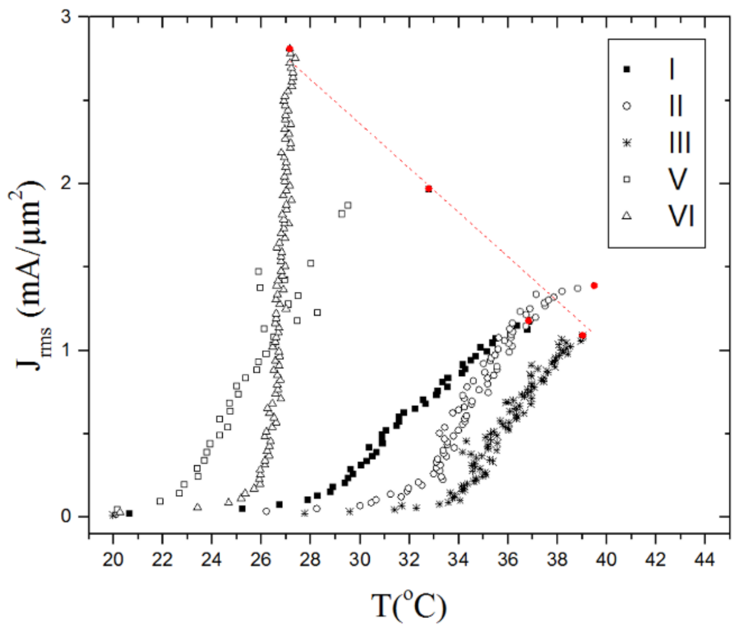

Fig. 6. 8 The current density (rms values) of the geometries versus the temperature of the metal due to Joule heating. The deterioration points are plotted as red full circles.

6.2.5 Long term reliability analysis: electromigration

Embedding the magneto-stimulating platform into a lab on a chip device is translated into a need for long term functionality. However, electromigration is another deterioration factor which affects the long term reliability of the micro-coils and should be taken into consideration. As discussed, Black's law, in equation (6.10), describes the failure time of electronic components functioning at specific conditions. However, it is not possible to estimate the value of the constant C as it is related to specific characteristics of the electroplated gold layer, such as the metal grain size. At the same time, there is no scientific record for the value of this constant for gold, as most of the studies focus on standard materials used in CMOS technologies. Even though it is not possible to calculate an absolute value for the MTF of each sample, a relative comparison between the samples could be made. The MTF of each sample is calculated in respect to the MTF of the most sensitive sample in terms of geometry, which is the IV sample. This aids finding the most reliable amongst the samples and also quantify its superior performance. Assuming functionality of the inductors close to their deterioration limit, with a duty cycle as above and under non-stop functionality, the worst case scenario was studied. For the calculation the current density at the deterioration point of each sample was used, the temperature is given from the relation $T_m=T_{ref}+\Delta T_{det}$, where T_{ref}=293K and ΔT_{det}

arises from the previous Joule heating study and represents the increase of temperature at the deterioration point.

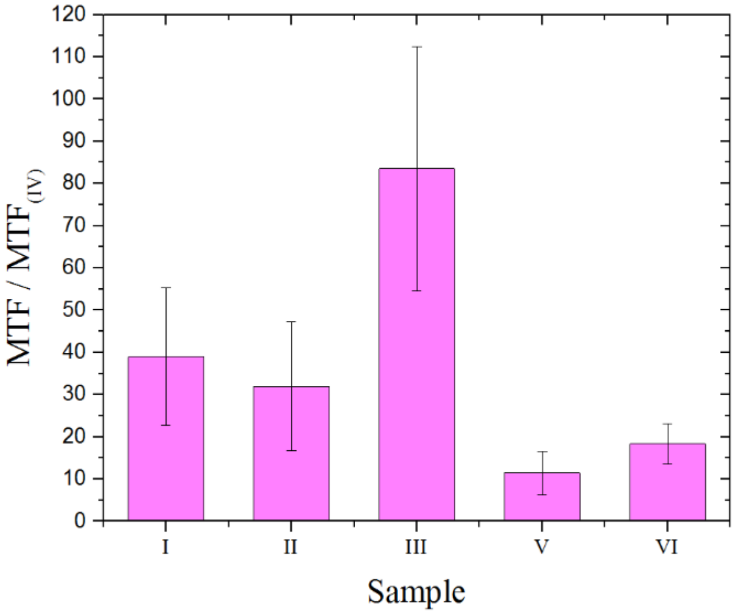

Fig. 6. 9 The median time to fail (MTF) of each sample over the MTF of the sample IV, with the smaller cross section.

Finally, the activation energy of an electroplated and not passivated gold layer is E_a=0.88eV [125]. Figure 6.9 summarizes the comparison of the MTF of each sample over the MTF of sample IV. As expected, all samples have higher MTF, with sample III showing the highest with MTF_{III}/MTF_{IV}=83.53±28.96.

Electromigration should also be taken into account in case there is a demand (eg. arising from the biological experiment) for increasing the current flowing through the micro-coils. In that case, the duty cycle of the train of pulses becomes an important factor. More specifically, the MTF should be higher than or equal to a failure time set as a goal, described by equation (6.15).

$$MTF \geq MTF_{goal} \Rightarrow \frac{\exp\left(\frac{E_a}{kT_m}\right)}{J_{avg}^2} \geq \frac{\exp\left(\frac{E_a}{kT_{ref}}\right)}{J_o^2} \tag{6.15}$$

Where T_{ref}=293K and J_o is the current density at the deterioration point. Since $J_{avg}=r \cdot J_{peak}$, the peak value of the allowed current density at a specific temperature Tm, is bound by the upper limit of equation (6.16).

$$J_{peak}^2 \leq \frac{J_o^2}{r^2} \frac{\exp\left(\frac{E_a}{kT_m}\right)}{\exp\left(\frac{E_a}{kT_{ref}}\right)} \tag{6.16}$$

Plotting this relation in figure 6.10, for sample IV, shows how drastically the maximum allowed current density peak decreases in higher metal temperatures. At the same time, the plots of different duty cycles indicate that towards spike operation micro-coils could sustain higher amounts of current, if this is needed for stimulation purposes. The relation is plotted over a biologically acceptable temperature range since temperatures above 40°C cannot be tolerated due to cell sustainability reasons.

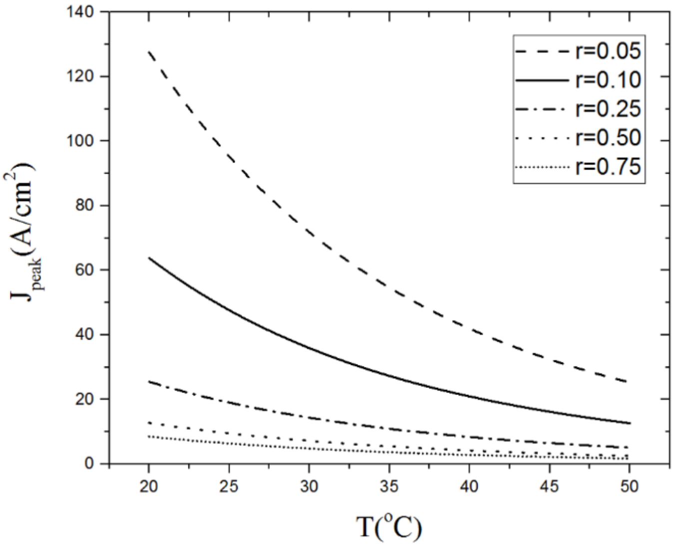

Fig. 6. 10 The maximum allowed peak value of current density pulses over the metal temperature T_m, for five different duty cycles (sample IV).

6.3 Summary

The first objective of this chapter was the electrical benchmarking of the prototyped devices. Specifically, an impedance frequency sweep was used to test the quality of the fabrication in six geometries. A comparison between the different samples was presented and the characteristics (impedance, inductance and quality factor) of the micro-fabricated samples were defined. Moreover, the impact of the passivation polymeric film and the different thickness of the electrodeposited material are also studied. The second scope of the chapter was an electrothermal study to assess the limits of safe operation of different geometries. The functioning conditions were set similar to those needed in a real bio-experiment. A relation between the current density at the deterioration limit and the temperature was also extrapolated and could act as a design parameter to similar studies. Finally, the effect of electromigration on the samples was discussed with a comparison between the different median failure times of the samples, while the maximum allowed current density peak value was calculated for different duty cycles. As expected, the most robust samples were those with the larger cross sections.

Chapter 7

Bio-realistic simulations and testing

This chapter focuses on bio-realistic approaches which were performed in order to test and quantify the capability of the micro-inductors to excite activity in neural cells. These studies are used as a proof of concept for the micro-magnetic stimulation and the aim of both studies is to test the efficiency of the developed devices prior to their use in real biological preparations where additional factors of complexity will be added. In the first approach, NEURON simulation environment [10] is used, which is an open source software developed as a tool to study numerically a simplified bio-physical problem. Cell activity and action potential propagation is determined by discretising a cell geometry into segments. In the second approach, the devices were characterised with the use of a phantom gel. The phantom gel was composed in house and was electrically characterised in order to present similar electrical properties (electrical permittivity and conductivity) to neural tissue. The phantom was placed on top of the Parylene-C insulating layer to represent neural tissue and then the current induced in the material was measured while the micro-coil was activated.

7.1 Characteristics of the micro-coil

The geometry chosen to be tested in the bio-realistic study is illustrated in figure 7.1 and its geometric characteristics are summarised in table 7.1. The specific geometry was chosen as it is the most efficient one for the smallest surface area of 50µmx50µm.

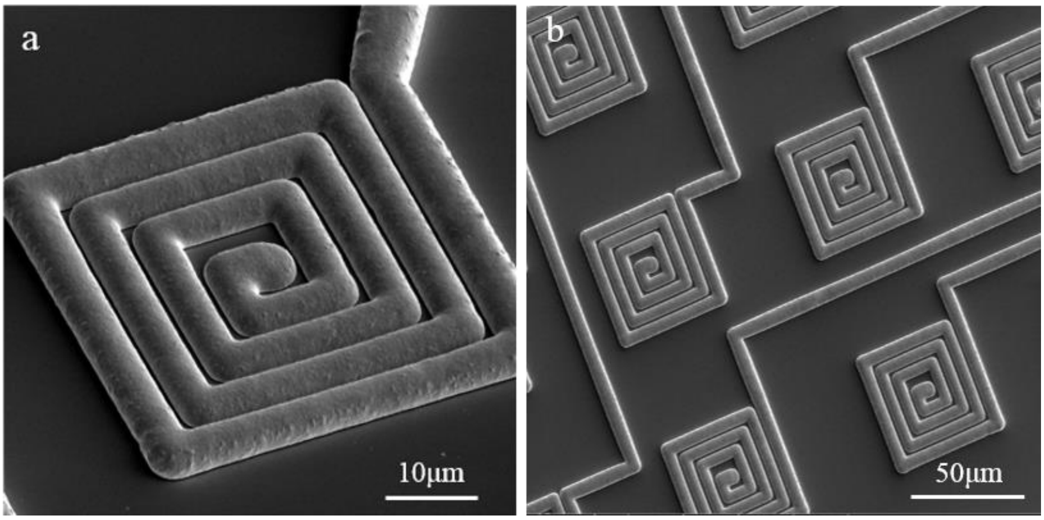

Fig. 7. 1 SEM imaging (a) A single micro-coil geometry. (b) Part of an array configuration.

Table 7.1 Geometric characteristics of the micro-coil under study.

	Value	Unit
Wire thickness	1.7	μm
Wire width	2	μm
Spacing	2	μm
Number of turns	5	
Surface area of coil	50x50	μm^2

The fabricated inductor was electrically characterised so as to identify the RLC equivalent circuit which describes its behaviour. Impedance frequency sweep of the device was performed on a Keithley SCS-4200. The testing biasing signal was 30mV and three set of measurements were taken. The resistance and reactance of the devices are calculated by measurements of the impedance magnitude and phase angle, while the inductance is extracted through the obtained values of reactance. The frequency ranged from 500kHz-10MHz, based on which the inductance and quality factor of the system are extracted. In figure 7.2(a), the impedance magnitude and the phase angle of the complex impedance vector are presented. Figure 7.2(b), shows the extracted values of inductance and quality factor Q, during the electrical test. Observing the behaviour of Z amplitude and phase in figure 7.2(a) and comparing it to figure 6.1, it is noticable that the self resonant frequency of the system is approximately at 10MHz, as Z magnitude reaches a peak and phase starts to decrease after a plateau. Above the self resonant frequency, the capacitance behaviour of the system would be dominant.

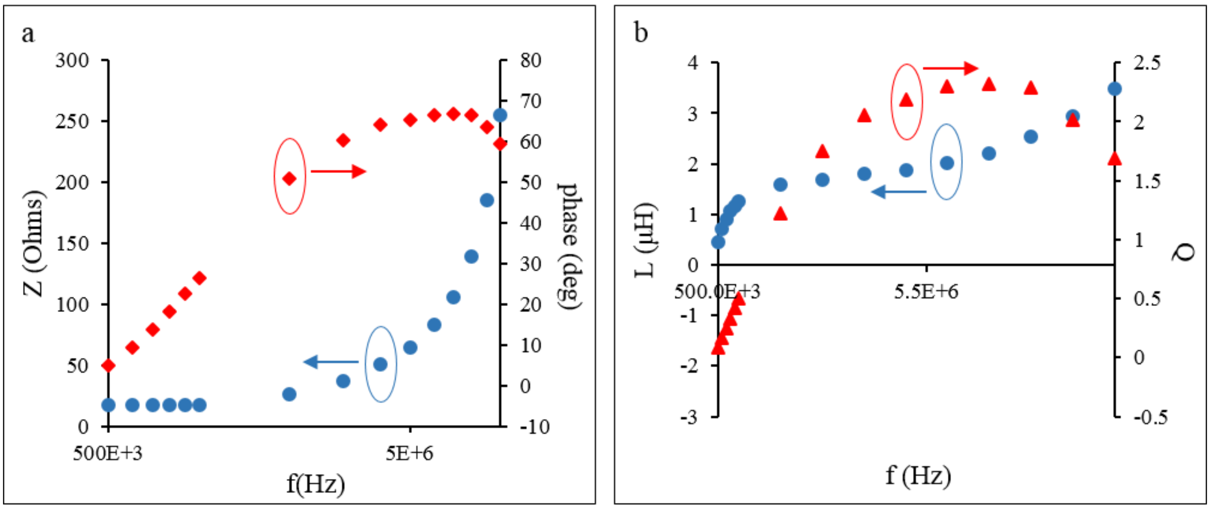

Fig. 7. 2 (a) Measured magnitude and phase of the complex impedance vector. (b) Inductance and quality factor Q of the system. For both cases, a logarithic scale is used for the horizontal axis of frequency.

7.2 NEURON simulation environment

NEURON simulation environment [126], is an open source simulator of neural cells and networks primarily developed by Michael Hines, John W.Moore and T. Carnevale at Yale and Duke University. The idea of this software is to formulate a conceptual model, which demands simplification of the real-world complexities, to describe particular properties of a biological system. The simulator is biologically oriented to provide modelling tools of neural cell geometries, solve computationally the mathematical equations and predict the behaviour of the system. Users can either use a graphical user interface, write code scripts or use flexibly a combination of both methods to define complex electrophysiological properties. An example of the graphical user interface is illustrated in figure 7.3, where the description of the different windows is highlighted.

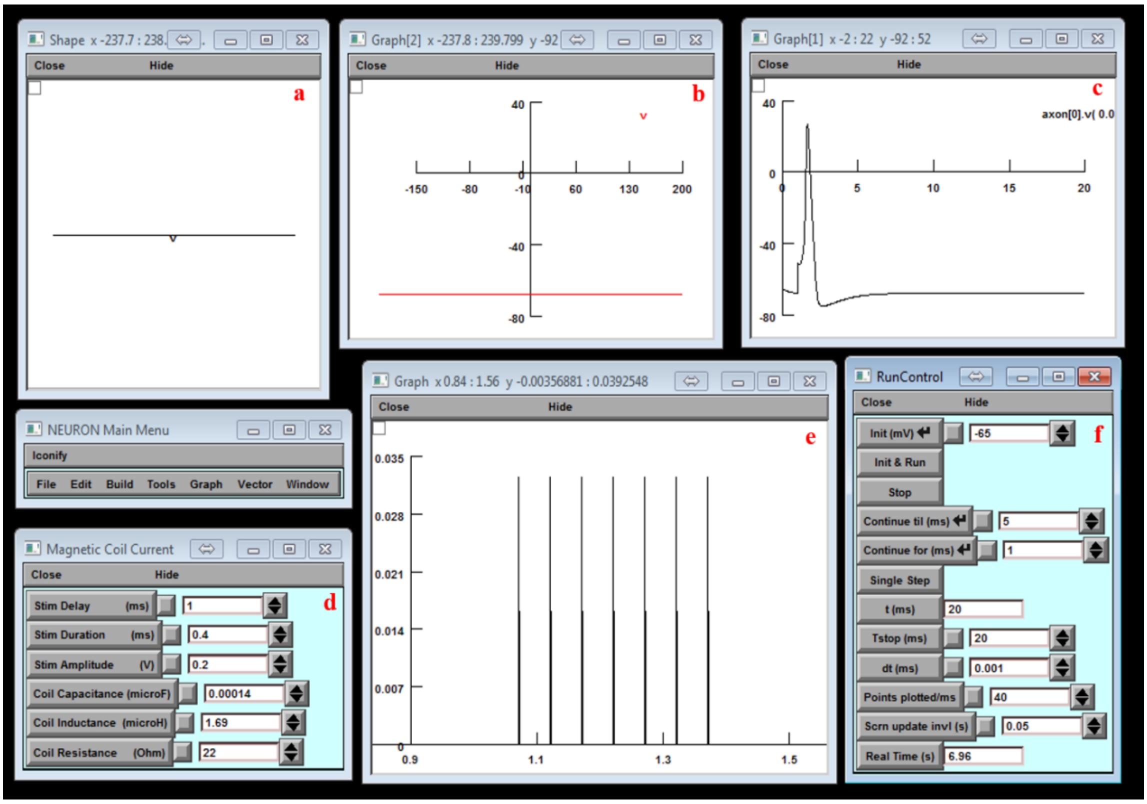

Stim Delay (ms) 1
Stim Duration (ms) 0.4
Stim Amplitude (V) 0.2
Coil Capacitance (microF) 0.00014
Coil Inductance (microH) 1.69
Coil Resistance (Ohm) 22

Init (mV) -65
Continue til (ms) 5
Continue for (ms) 1
t (ms) 20
Tstop (ms) 20
dt (ms) 0.001
Points plotted/ms 40
Scrn update invl (s) 0.05
Real Time (s) 6.96

Fig. 7. 3 Example of graphical user interface in NEURON simulation environment. Windows: (a) Cell morphology, (b) Spatiotemporal changes of transmembrane potential, (c) Transmembrane potential over time, (d) Stimulus settings, (e) Stimulus representation, (f) General settings.

7.3 Cable equation for magnetic stimulation

This subsection introduces the mathematical description of the simulated model. The analytical description gives the important information to understand the results obtained from NEURON simulation study. The cable equation [127] and Hodgkin-Huxley nonlinear dynamics of voltage-sensitive membrane channels [128] describe the behaviour of the neural tissue in response to applied electrical fields. The transmembrane flow of current leading to alteration of membrane potential (cellular excitation or inhibition) is closely related to the second spatial difference of the potential field along the axon, cell body, and dendrite [129]. The cable equation could also be in use for the case of magnetic stimulation [68] and is presented in equation (7.1)

$$\lambda^2{}_m \frac{\partial E_x(x,t)}{\partial x} = -\lambda^2{}_m \frac{\partial^2 V_m(x,t)}{\partial x^2} + \tau_m \frac{\partial V_m(x,t)}{\partial t} + V_m(x,t) \tag{7.1}$$

Where: E_x is the x component of the induced electric field assuming that a fibre on the x axis parallel to the plane of the coil. τ_m is the membrane time constant given by the relation: $\tau_m = c_m r_m$ and λ_m the length constant of the fibre given by the relation: $\lambda_m = (r_m/r_i)^{1/2}$. V_m represents the transmembrane voltage (the voltage difference between intracellular and extracellular fluid), r_i is the intracellular resistance per unit length (Ω cm^{-1}), r_m is the membrane resistance (kΩ·cm axon length), and c_m is the capacitance per unit length (F cm^{-1}).

The goal is to determine the induced electric field as well as its spatial variation, with respect to the input current in the coil geometry (number of turns, shape). The magnetic field could be expressed as the curl of the magnetic vector potential **A** given in equation (7.2).

$$\vec{B} = \nabla \times \vec{A} \tag{7.2}$$

While Faraday's law in equation (7.3) gives the induced electric field **E**.

$$\nabla \times \vec{E} = -\frac{\partial \vec{B}}{\partial t} \tag{7.3}$$

Combining both expressions a generic form for the induced electric field is obtained and presented by equations (7.4) and (7.5). The magnetic vector potential is described from the geometric characteristics of the structure under study and the current density J flowing through it.

$$\vec{E} = -\frac{\partial \vec{A}}{\partial t} \tag{7.4}$$

$$\vec{A} = \frac{\mu_o}{4\pi}\int_V \frac{\vec{J}(r', t_r)}{|r - r'|}\, \mathrm{d}^3 r' \tag{7.5}$$

Where: μ_o is the magnetic permeability of free space and r is the distance between an element of the coil and the point where the magnetic potential is calculated. The calculation of magnetic potential, or directly of the induced electric field for any type of complex structure could be easily performed by a finite element method software and the magnetic stimulation equivalent cable equation is then fully described. The aforementioned calculations are accurate in the absence of neural tissue. Special consideration should be taken into account in the presence of tissue, as surface charges are accumulated at the air-tissue interface. This fact creates a secondary electric field, which has been studied in several scientific studies [110], [130]–[132].

This induced electric field **E** can be further separated into a spatial and a temporal function. As discussed in more detail in section 7.4, the spatial part of the electric field is calculated in COMSOL which solves the mathematical problem described by equations (7.2)-(7.5) prior to the simulation and was then exported from COMSOL to NEURON. For the temporal part of the electric field the methods study [133] are implemented. Both functions combined create the activation function which is given by the left side of equation (7.1). The modified cable equation (7.1) combined with the calculation of the activation function leads a quantified prediction of the neural stimulation. Neuronal excitability was simulated using the Hodgkin-Huxley model that is part of the NEURON simulation environment.

7.4 Modelling an axon in the vicinity of a micro-coil

The main concept of this simulation study, is to model the cell geometry in NEURON simulation environment and use data from the experimental characterization of the devices and from FEM simulations in COMSOL. The two components needed to accurately describe the properties of the model are the impedance of a prototype device as measured experimentally in combination with the spatial distribution of the induced electric field resulting from the an electromagnetic study in COMSOL. These characteristics are inserted into NEURON environment to study the possibility of cell activation. The conceptual model was based on an existing model from a well cited study in the field [63], which was modified to fit a case of interest. More specifically, in that simulation study, the capability of a circular coil of radius 2cm which was placed close to an axon of 16cm length and 100μm diameter was tested. Since the axon diameter of 100μm, proposed in [63], is high and it was important to decrease it by an order of magnitude to be more relevant to in-vitro studies of interest. For the same reasons, the axon length was further modified to 70μm, comparable to the dimensions of the micro-coil, as in a real case scenario. As the platform should work over a wide range of biological preparations and can be used versatilely with different cell cultures or tissue slices, a variety of cell morphologies is expected; thus the study was kept as much as possible realistic yet cell-agnostic.

A neural axon was set, assigned with active Hodgkin-Huxley channels, lying parallel to the plane of the micro-coil and centred above the coil. The cell is divided into discrete segments, on each of which an induced electric current is calculated, representing the magnetic stimulation effect on the segment. The electric field which is induced in the vicinity of the coil could be expressed as a product of a spatial and a temporal component. The spatial component of the induced electric field in the x direction can be calculated externally in COMSOL Multiphysics software and then inserted to NEURON code. The exported values of Ex(x), for constant values of y (direction of axon in the xy plane) and z (vertical distance of axon from the plane of micro-coil), are then inserted to NEURON. The spatial derivative of Ex in the direction of x, contributes in the calculations of the induced electric field term in the cable equation. The temporal part of the solution, is calculated as described in the methods of study [63] in every time step. The final solution arises as a spatiotemporal composition of solution in the individual segments. The R, L, C values of the stimulator circuit are also modified to the measured values of the equivalent circuit, obtained from the electrical characterization of the system presented in figure 7.2. More specifically, the geometry under study here has an equivalent circuit with RLC values defined as: R=22Ohms, L=1.69μH and C=14nF, considering the self-resonant frequency at 10MHz. Finally, the input stimulus has amplitude up to 200mV and variable stimulus durations were tested. The planar distribution of the electric field is presented in figure 7.4(a), while in figure 7.4(b) the spatial distribution of the x component of the electric field is illustrated, both of them for the plane where z=10μm.

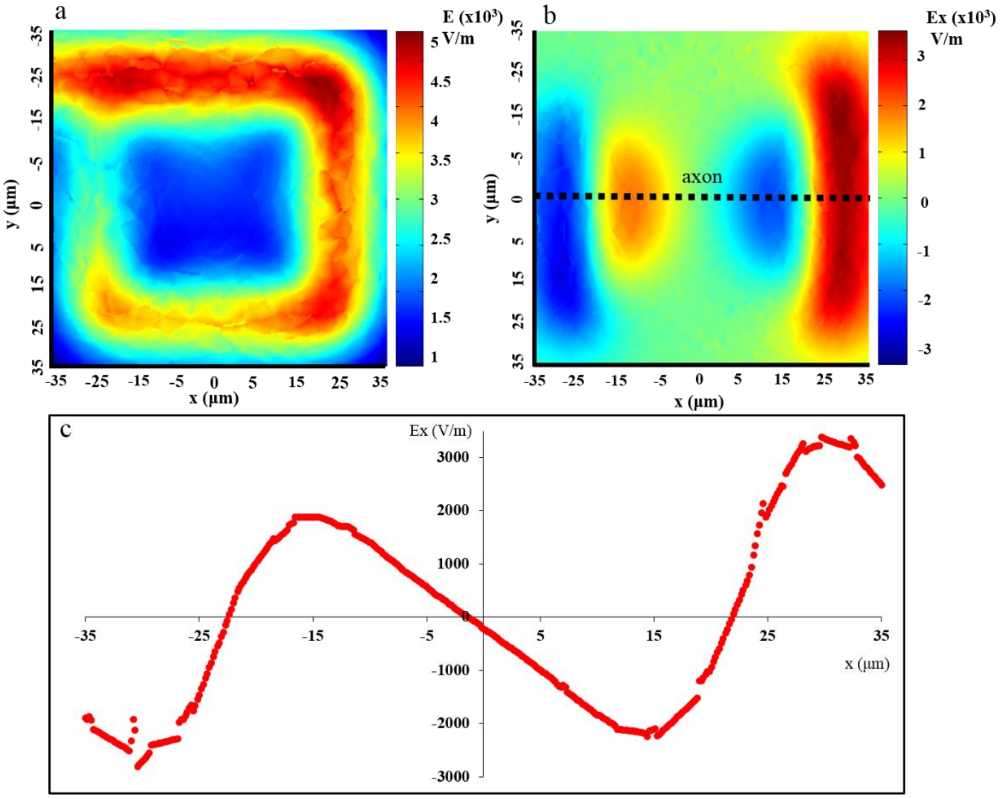

Fig. 7. 4 Planar distribution of (a) electric field (E) and (b) x component of electric field (Ex), for a distance of 10µm above the micro-coils. (c) Plot of x component of electric field along x, for a specific value of y.

This distance was chosen as a realistic but long enough distance to cover the worst case scenario. Specifically, the distance between the electromagnet and the cell medium in an actual bioexperiment is mainly determined by the thickness of the parylene-C film, which is deposited at thicknesses <10µm. If stimulation is possible for z=10m, it would also be possible for all the range of distances below 10µm where the induced values of the electric field are higher. The graph shows also the relative position of the axon to the micro-coil. Finally, figure 7.4(c) is the plot of Ex along the increase of x, for y=0 where the axon is located. The transmembrane potential elicited in the axon modelled, is presented in figure 7.5 along with time, indicating the activation of the cell for a stimulus of 200mV with a duration of 0.4ms. Similar behaviour is observed for stimulus durations in the range of 2µs-2ms. The simulation shows that a simplified cell geometry, placed in a distance similar to the realistic case, feels the presense of the induced electric field and an action potential is elicited and propagates along the axon. Stimulus duration has been tested with NEURON and cell stimulation for purely pulsed stimuli was observed with amplitudes up to 200mV and durations between 2µs-2ms. Stimulus with an amplitude of 200mV and duration of 1μs did not elicit cell activity. The range of stimuli tested was based on similar studies of microscale magnetic stimulation [2]–[4].

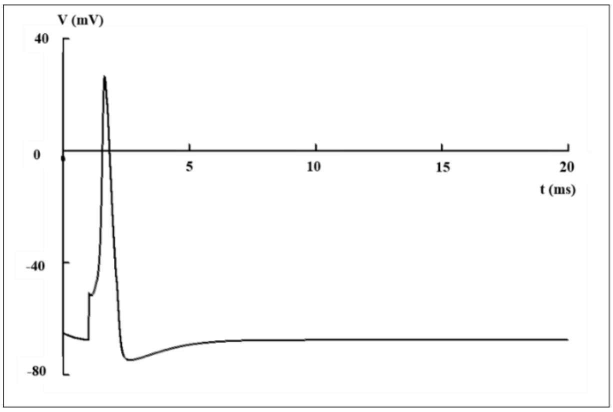

Fig. 7. 5 Example of stimulus which manages to activate the neural cell. The activation of the cell is illustrated by the transmambrane potential elicited in the axon over time.

7.5 Modeling a cell: axon and soma configuration

For the interest of a complete study the simulations were expanded to include a more detailed cell description. More specifically, a neural geometry consisting of a soma and an axon was considered situated in the vicinity of the coil at the same distance. The size of the soma was set at 10μm based in literature [134] and also came in agreement with the soma dimensions of the cultured hippocampi neural cells presented in chapter 8. The axon was again 70μm. The stimulus characteristics remain the same and two different orientations of cells were tested. Figure 7.6 shows a schematic of the neural cell structures in relation to the x component of the electric field they feel. In the first orientation (Figure 7.6 green neuron) the cell produces an action potential as in the case of the single axon. In contrast, in the second orientation (Figure 7.6 red neuron) the Ex component of the electric field does not have any impact on the cell. The latter is expected, as Ex does not have any significant change across the line of the laying cell and no stimulation sites are present. In a real case scenario though, due to the symmetry of the design, this cell would be activated due to the y component of the electric field.

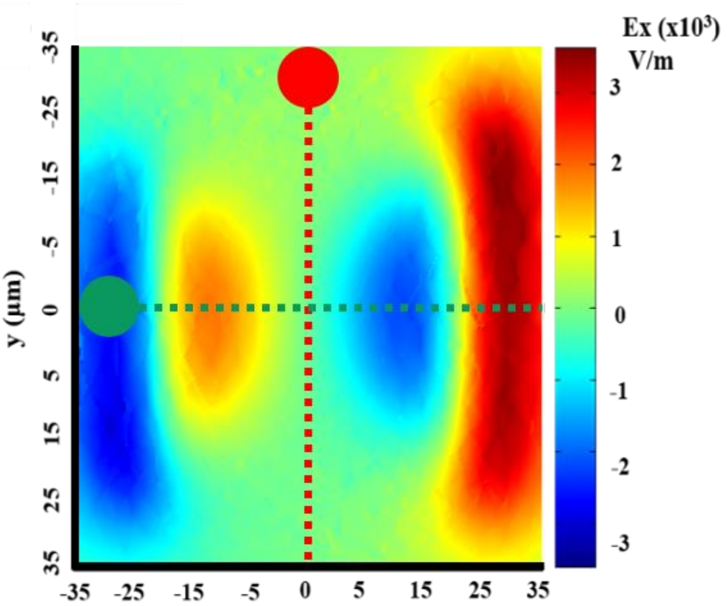

Fig. 7. 6 Planar distribution of x component of electric field (Ex) for a distance of 10µm and a schematic representation of two cell configurations (soma and axon) situated in two different orientations in a plane above the micro-coil.

7.6 Measuring inductive current in a phantom gel

Due to the very small size of the micro-coils, magnetic characterization with ordinary magnetometers is very difficult. However, even in the case where a magnetic characterization could be performed, the result of a known value for the magnetic field would not be directly useful for identifying the capability of the devices to activate neural tissue, since the threshold of neural activation is referenced either in terms of voltage or current. As a result, this study focused on a way to measure the induced current, produced by the micro-coils, in a material with electrical properties similar with those of neural tissue. In the following subsections, the material composed to mimic the electric properties of neural tissue, as well as the setup and results of the experiments are presented. The idea of using a phantom solution or gel to mimic different properties of human tissue has been used a lot in literature [135]–[140], especially on studies concerning the electromagnetic behaviour of brain or muscle tissue. Based on this idea, a series of experiments have been performed, using the composed phantom, as a useful intermediate step before testing in a real cell cultures of increased complexity and unknown variables.

7.6.1 Phantom solution composition

The phantom solution has a specific composition so as to demonstrate similar electric properties (electric permittivity and conductivity) to real neural tissue. The composition is based on study [137], however small changes in the ingredients were needed so as to have a better fitting between the electrical properties of the gel and those of measured brain tissue for a lower frequency range. Additionally, an increase in the amount of the gelling agent hydroxy-ethyl cellulose (HEC) is introduced to achieve a semi-solid consistency, which is needed in the experiments. The phantom gel materials, used in the experiments are presented in table 7.2. More technical details concerning the fabrication of the phantom gel are provided in Appendix 2.

Table 7.2 Phantom gel materials and composition.

	% by weight
Sugar	54.5
Water	39.2
HEC	3.9
Salt (NaCl)	2.4
Bacteriacide	0.1

7.6.2 Electrical characterization of the phantom solution

The appropriate way to characterise at low frequencies a medium lossy dielectric, as the composed gel, is by using a parallel plate capacitor configuration [141]. A schematic of the characterisation setup and the equivalent circuit of this method is illustrated in figure 7.7. During the characterization experiment, the gel is set as a dielectric in between the parallel plates of a capacitor. By knowing the thickness of the dielectric and the surface area of the capacitor, one could extract the electric permittivity and conductivity of the dielectric [142]. The gel quantity set between the metallic plates of a capacitor has a thickness of 3mm. The significant thickness of 3mm is chosen, so as to have negligible impact on the measurements from the air trapped in the interface between the gel and the metallic plates. It is known that the real part ε_r' of the complex relative permittivity ε_r^* gives an indication of the polarization of the dielectric, while the imaginary part ε_r'', is a measure of how lossy the material is. The imaginary part is also called loss factor of a material and includes both the effects of dielectric loss and conductivity.

A Keithley semiconductor parameter analyser was used to perform an impedance measurement of the dielectric in the parallel plate configuration. The received results are chosen to be expressed in the equivalent circuit of a parallel conductance G and capacitance C_p.

$$Y = G + i\omega C_P = i\omega C_o\left(\frac{C_P}{C_o} - i\frac{G}{\omega C_o}\right) \tag{7.6}$$

From equation (7.6) the complex relative permittivity ε_r^* could be obtained and finally by its imaginary part, the conductivity of the fabricated gel will be extracted.

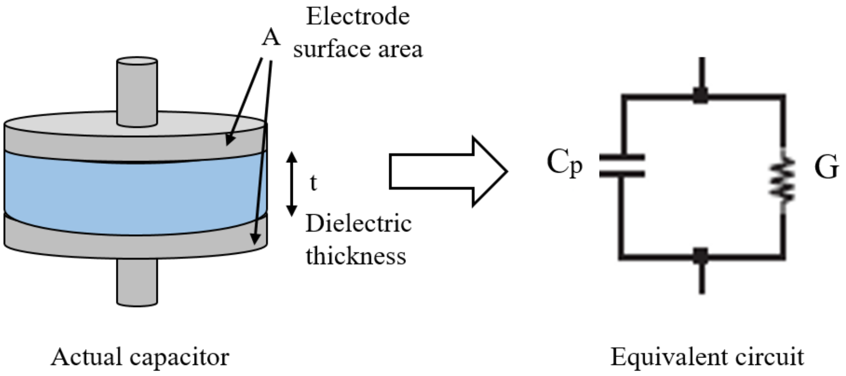

Fig. 7. 7 Parallel plate capacitor configuration used for the electric characterization of the gel and the equivalent circuit which describes the setup.

In equations (7.7) and (7.8), t is the thickness of the dielectric, C_o the capacitance without the dielectric, ω the angular frequency, ε_o the permittivity of free space, R_p the resistance of the parallel circuit and A the surface area of the capacitor plates.

$$\varepsilon_r^* = \varepsilon_r' - i\varepsilon_r'' = \left(\frac{\varepsilon'}{\varepsilon_o}\right) - i\left(\frac{\varepsilon''}{\varepsilon_o}\right) = \left(\frac{C_P}{C_o} - i\frac{G}{\omega C_o}\right) \tag{7.7}$$

$$\varepsilon_r' = \frac{tC_p}{\omega\varepsilon_o} \quad \text{and} \quad \varepsilon_r'' = \frac{t}{\omega R_p A \varepsilon_o} \tag{7.8}$$

Since the next step will be the measurement of the induced current in the gel because of the activation of the micro-coils, the parameter of interest is the conductivity σ of the fabricated gel which is defined by equation (7.9).

$$\sigma = \varepsilon_r'' \varepsilon_o \omega \tag{7.9}$$

The results were directly compared to the data base provided by the well-known experiments of *Gabriel et al.* [107], [108] at the lower frequency ranges. *Gabriel et al.* datasets for electric permittivity and conductivity of both grey and white matter are presented also in Appendix 3. To be more specific, the conductivity of the fabricated gel was compared with the result obtained by the mean value of grey and white matter brain tissue. The results from the electric characterisation of the solution are summarised in figure 7.8.

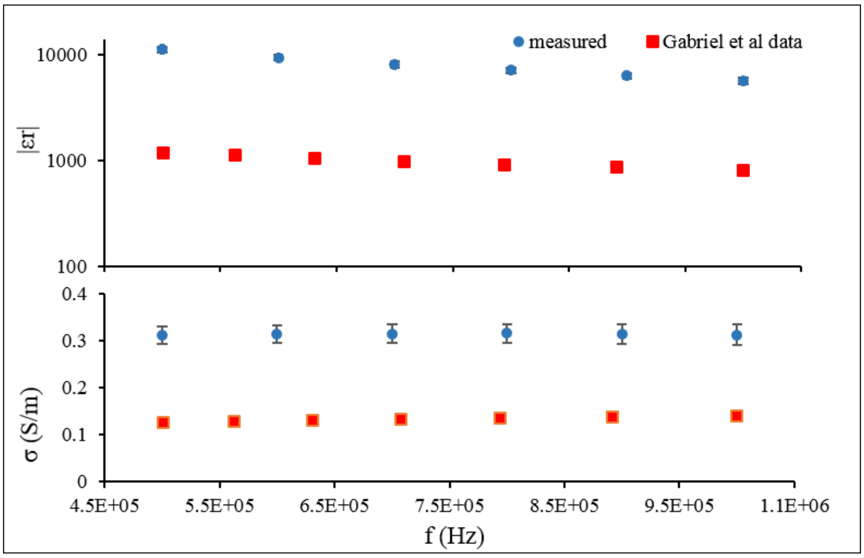

Fig. 7. 8 Electric permittivity and conductivity values of the fabricated phantom compared with measured values in real neural tissue. Error bars representing standard error.

Specifically, figure 7.8 shows the electric permittivity and conductivity as measured at the solution in blue, versus the Gabriel at al. data in red. Three sets of measurements of electric permittivity ε_r and electric conductivity σ were taken and their mean values, displayed with circle markers in the graphs, are directly compared to the values of real biological brain tissue, given by [108]. The relevant biologically expected values, displayed with square markers, are the mean values of white and grey matter for every frequency. The electric conductivity values of the phantom gel have are in good agreement with the electric conductivity values of brain tissue, while the electric permittivity results could not reach the same extent of similarity. However, the value of conductivity is influencing more significantly the induced current density in a leaky dielectric. Specifically, the current density in a leaky dielectric is given by equation (7.10).

$$\mathbf{J} = \mathbf{J}_{free} + \mathbf{J}_{bound} = \sigma\mathbf{E} + \frac{\partial \mathbf{P}}{\partial \mathrm{t}} + \nabla \times \mathbf{M} \tag{7.10}$$

J is the current density which consist of two parts: $\mathbf{J}_{\mathbf{free}}$ current density by free carriers and the $\mathbf{J}_{\mathbf{bound}}$ current density attributed on the relocation of bound charges. **E** the applied electric field vector, **P** the polarisation field vector produced by the dielectric and **M** the magnetization vector of the material. Since the material is not magnetic, the last part of equation (7.10) could be omitted. For the frequency range of interest, and by moving to the frequency domain as the study concerns harmonic signals, a simple comparison between the two terms is enough to give the dominant factor in the current density of the dielectric:

$$\mathbf{J}_{free} >> \mathbf{J}_{bound} \tag{7.6}$$

The explanation arises by equations (7.12) and (7.13) below. $\mathbf{J}_{\mathbf{bound}}$ in equation (7.13) takes a range of values, defined by the frequency ω of the harmonic signal, but in any case gives a $\mathbf{J}_{\mathrm{bound}}$ smaller at least by an order of magnitude from $\mathbf{J}_{\mathrm{free}}$.

$$\mathbf{J}_{free} = \sigma\mathbf{E} \approx \left(10^{-1}\frac{S}{m}\right)\mathbf{E} \ \approx 10^{-1}\mathbf{E} \tag{7.12}$$

$$\mathbf{J}_{bound} = i\omega\mathbf{P} = i\omega\varepsilon_o\left(\varepsilon_r - 1\right)\mathbf{E} \approx \left(10^5 s^{-1}\right)\left(10^{-12}\frac{F}{m}\right)10^4\mathbf{E} \approx 10^{-3}\mathbf{E} \tag{7.13}$$

As a result, despite the significant difference between the measured values of electric permitivity and the biological values, it is possible to use the suggested phantom and extract safe results. Regarding the difference in conductivity, which should be also taken into consideration, it is easy to assign more realistic values to the results by a simple multiplication, as the current depends linearly on the value of conductivity. The next step of this study is to use the composed and characterised phantom gel on top of a micro-coil and measure the amplitude of the induced current when the microfabricated inductor is set at an “ON” state and a current flows though it. The values of induced current in the phantom are then compared with current amplitudes obtained in extracellular electrical stimulation experiments of neural tissue. The basis of this comparison is that magnetic stimulation, is more accurately described as an indirect electrical stimulation method. In electrical stimulation, current flows in the cell medium create a localised instability which forces the cell to excite an action potential and restore the equilibrium. In the case of magnetic stimulation, the current instability is produced by the alternating magnetic field. Since the mechanism of activation remains the same in principle, the comparison of the results to those of electrical stimulation becomes meaningful.

7.6.3 Inductive current measurements due to micro-coil activation

At the next step, a chip with a single micro-coil geometry, covered with Parylene-C, was used in order to identify the induced current density evoked into the gel by the activation of the micro-coil. The signal used for the biasing of the micro-coil was an AC signal of 500kHz, for a number of different amplitudes between 20-200mV. A burst of rectangular pulses was also tested as a biasing signal, but was not preferred for this experiment, due to charging phenomena in the gel. The measurements were performed with the use of Keithley 4200 semiconductor parameter analyser and the use of a probe station. In figure 7.9, the characterization setup used for the measurements of the induced currents in the phantom gel is presented. The phantom gel was centred carefully above a single micro-coil geometry and on top of the insulating Parylene-C layer. The micro-coils are biased by a function generator through the lower set of needles illustrated figure 7.9. The peak-to-peak values set in the function generator cover the range of 20-200mV. The measuring probes are illustrated on top and during the experiment were set to a number of different positions above the centre of the micro-coil, with the use of a micropositioner and a microscope.

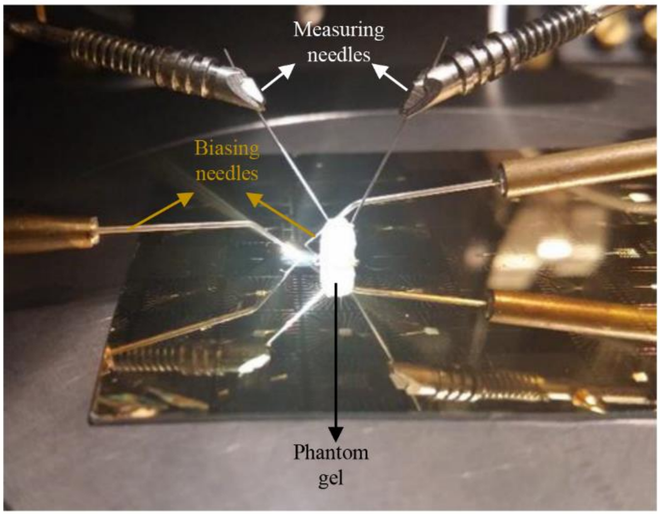

Fig. 7. 9 The characterization setup to measure the induced current in the phantom gel, due to the activation of the micro-coils.

The starting distance was from the surface of the Parylene-C film (z=0) to a final distance of 1000μm. The results are displayed in figure 7.10 and are part of one set of measurements inside the gel. For every position of z, four different measurements were taken for the different voltages applied (peak to peak values). Repetitions of the measurements have been performed, but decided not to be included, as there was a difficulty in relocating the needle into the x,y.z position due to the semi-solid consistency of the gel and could be misleading. Data from the repetition of the experiments, for a different x,y,z position in the gel, above the micro-coil, as well as for different biasing frequencies, show similar behaviour and induced currents in the μA range. The measurment of the induced current in the gel, in figure 7.10 as expected shows a decreasing tendency as moving away from the micro-coil surface. The amplitude of the induced current is extracted in the steady state with the use of a harmonic signal of 500kHz. The maximum value is received, for z=0 just above the Parylene-C surface, while for every position z, the induced current increases with the increase of the biasing voltage amplitude.

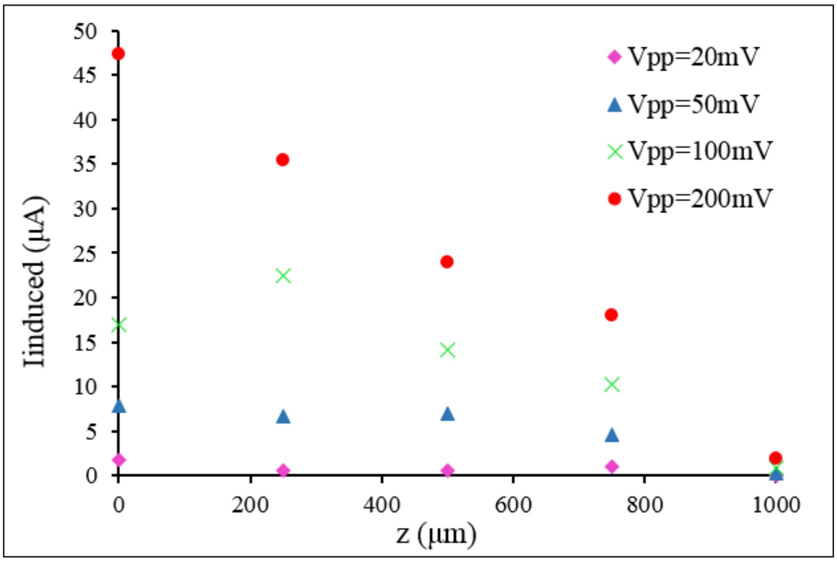

Fig. 7. 10 The current induced in the phantom solution, for a different nuber of positions away from the micro-coil and for a different setting of peak to peak applied voltage used as bias to the micro-coils. All the measurements were performed for the frequency of 500kHz.

A direct comparison of these results with those of study [143], shows that the proposed platform produces equivalent current amplitudes to electrical pulses applied extracellularly in the cell medium. More specifically, study [143] reported that neural cells of the spinal border cells or motoneurons, have their lowest threshold of activation (for a minimum distance from the cell) at stimulus amplitudes of 0.15-0.20μA and 0.35-0.40μA respectively. Figure 7.10 shows that for the minimum distance the results are significantly higher, even by interpolation to the more realistic expected values of conductivity (devide by a factor of 3 the conductivity values received from figure 7.8).

Similarly, measurements of the induced current in the phantom gel were performed for an increased peak to peak applied voltage to the micro-coil, for a number of different frequencies in the range of 500kHz-1MHz. Figure 7.11 contains the mean values of the data received from two sets of measurements. Error bars in the y axis represent the standard error, while in x axis the accuracy of the function generator. As expected, for every frequency, the increase of the biasing micro-coil voltage leads to the increase of the measured induced current in a linear manner. This is explained by applying Ohm's law in the micro-coil and Faraday's law of induction in the gel, while taking into consideration that for a specific frequency the impedance of the structure and the conductivity of the phantom gel remain also constant. It is obvious that the higher the frequency the more the induced current measured, but here the increase is not linear due to the frequency dependant behaviour of the impedance.

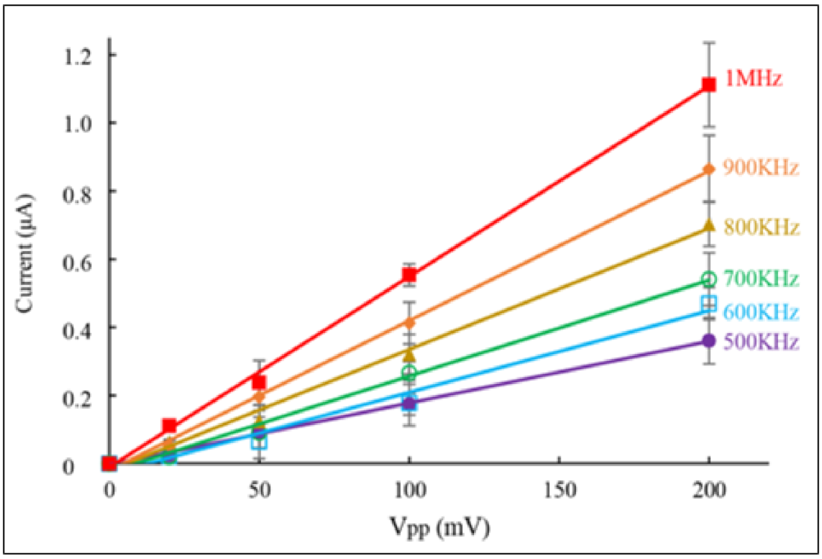

Fig. 7. 11 Measurements of the induced current in the phantom gel along with the increase of the peak-to-peak voltage applied to the micro-coils for different frequencies in the range 500kHz-1MHz.

However, the threshold of cell activation is not determined only by the amplitude of the stimulus but also by its duration and is given by the strength-duration relation. The strength-duration curve is not fully understood for the magnetic stimulation mechanism [2]. Therefore, the approach in the real bio-experiment would be to start from a specific stimulus duration and run over a range of stimulus amplitudes, which should be below the deterioration threshold of the micro-coils. This procedure will be repeated with a gradual increase of stimulus duration, until cell activation will be observed. Furthermore, in a realistic scenario of cell stimulation, a pulsed method of stimulation could be combined with a sinusoidal signal of higher frequency, as in [3], where a burst of sinusoidal periods led to suppression of neuronal activity.

Finally, micro-coils should be able to work over a wide range of biological preparation, a fact that implies that the bioexperiment itself would determine the specific needs for the characteristics of the system. In case further improvement of the results is needed to achieve cell stimulation, this could be achieved by thicker coils, with larger cross section, able to hold a higher current capacity and produce stronger electromagnetic field or neural cells placed in greater proximity to the micro-coils, set by a lower thickness in the Parylene-C layer. Finally, a signal with a steeper time variance, such as a pulse of same amplitude and frequency, would result in an even higher induced current magnitude as describes by Faraday’s law.

7.7 Summary

In this study, the performance of the devices is tested both numerically and experimentally. In summary, the RLC characteristics of the system, received from the electric characterization, are used to calculate the temporal component of the stimulating effect on NEURON. The induced electric field, extracted from COMSOL calculations is also imported to NEURON to define the spatial component of the stimulation. The numerical study showed that an action potential is created and propagated along the axon of a neural cell, placed at 10μm away from the inductor. The simulation was repeated for a neural geometry consisting of a soma and an axon. Two different placement orientations were tested above a micro-coil. Following the simulation study, a phantom gel with similar electric properties as the brain tissue was composed and used to quantify the amplitude of the induced current by the activation of a micro-coil. The results support the capabilities of the engineered prototypes and demonstrate the desirable characteristics. The next steps of this study involve additional technics which demonstrate the functionality of the devices, with magnetic stimulation in vitro being the final goal.

Chapter 8

Functionality of the micro-fabricated arrays

This chapter summarises a series of experiments which support the functionality of the micro-magnetic arrays. At a first approach, a qualitative experiment is demonstrating the existence of a magnetic field near the electromagnets, by magnetic nanoparticle trapping. Inductive coupling, between neighbouring coils in the same array, is also a further performed as a quantitative method to extract the strength of electromagnetic coupling between adjacent micro-coils. Finally, the biological testing of magnetic stimulation in vitro is presented in neural cells. The cells used were hippocampi neural cells and were chosen by collaborator biologists in University of Padova, based on their biological methods and cell availability. The biological testing is presented with details in the methodology of the cell culturing to the actual experimental procedure.

8.1 Magnetic beads demonstration

Magnetic beads have been used in a plethora of different bio-applications to support the existence of a magnetic field or as a components to achieve spatial manipulation from localised magnetic fields [111]–[113], [144]. Within this framework of applications a series of experiments with magnetic nanoparticles was performed. These experiments were performed prior to the biological experiments and indicate the existence of a magnetic field, which is very difficult to be measured with conventional methods and magnetometers, due to the very small size of the structures. At the same time, useful observations for the choice of the most appropriate samples for the bio-experiment were made.

The activation of the micro-coils in the PCB packaged devices is achieved with the use of a function generator. An OPAMP (TL081) is used in a buffer configuration so as to achieve a good matching between the low resistance of the coil addresses and the internal resistance of the function generator. The input of the coil is observed with an oscilloscope. A schematic of the activation setup is illustrated in figure 8.1.

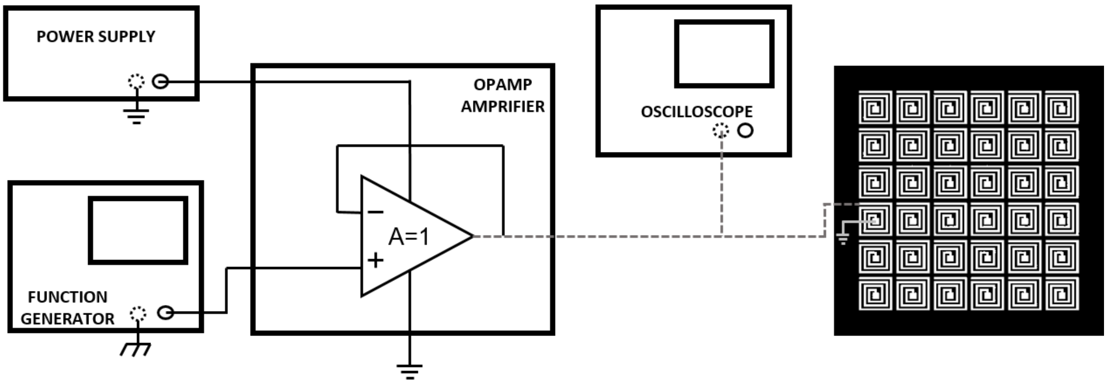

Fig. 8. 1 Schematic of the electronic setup for the activation of the micro-coils.

Fe_2O_3 [Sigma-Aldrich Fe_2O_3 powder <5μm] magnetic nanoparticles with an average diameter of 5nm are mixed into deionised water in a concentration of 5mg/ml. Small amount of the aqueous solution is dropped with a pipette in the effective area of the sample, which is confined by the 3-D printed ring. During activation of the micro-coils the area of activation is observed and recorded with the use of an optical microscope. Here, the magnetic nanoparticle trapping is presented on two of the fabrication geometries, even though it was tested on all samples. The trapping of the magnetic beads from a micro-coil is reported on figure 8.2, where consecutive screenshots in a time range of 11sec were taken. The time window width is random and was chosen to highlight the accumulation of magnetic beads on top of the activated micro-coil. The micro-coil presented in figure 8.2 has a side length of 100μm and 3 windings.

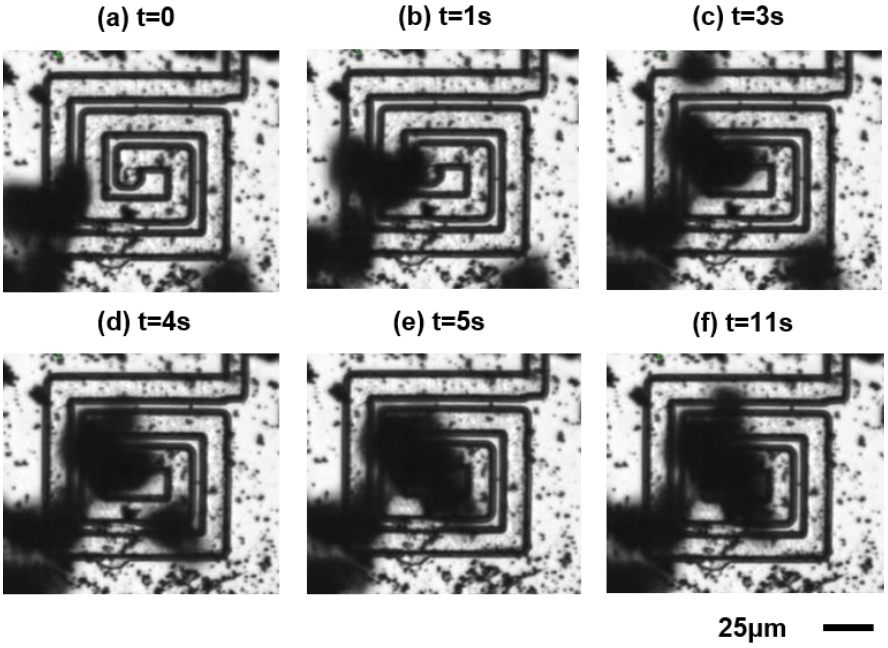

Fig. 8. 2 Trapping of magnetic nanoparticles from a micro-coil presented in consecutive time screenshots from 0-11 seconds.

The signal set to the function generator for the activation of the micro-coil is 100mV, corresponding to 20mA of current flowing though the micro-coil. The input signal used was a pulse with 10% duty cycle at the frequency of 1Hz. A low frequency was chosen, in order to give an appropriate response time to the beads to move and observe their movement through the microscope. From the images it is clear that the magnetic nanoparticles aggregate in the presence of the magnetic field and as time passes, the area above the activated coil is getting covered with a constantly increasing number of nanoparticles. Similarly, figure 8.3 shows magnetic nanoparticle trapping from a different geometry with a side length of 100μm and 3 windings.

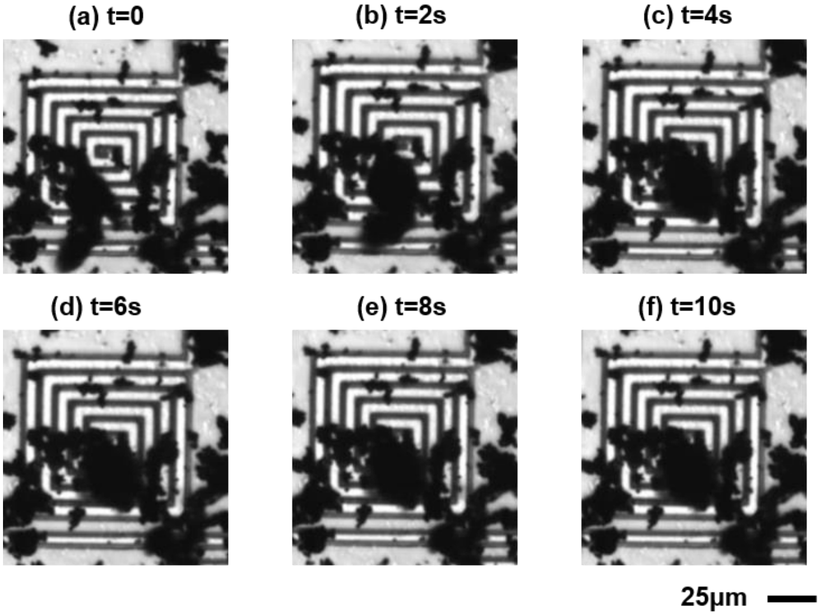

Fig. 8. 3 Trapping of magnetic nanoparticles from a second micro-coil presented in consecutive time screenshots from 0-10 seconds.

As an example, in some cases of micro-coil activation, trapping of magnetic nanoparticles was observed by neighbouring coils as well. This was observed on structures where the separation distance between adjacent coils in an array was at 25μm (the minimum fabricated) and was not the case for separation distances of 50-200μm. The platform could be proposed as an alternative design for micro-scale localisation of magnetic fields. Different micro-coil sizes and array sizes are possible, making the device ideal for tailoring its functionality to the needs of a specific experiment, in terms of spatial resolution.

8.2 Inductive coupling

The experiments with the magnetic beads indicated some interaction between the micro-coils, in the case of the smallest fabricated separation distance (25μm). This is equivalent to a behaviour of a transformer and the inductive interaction is expected to become more important as distance between the micro-coils decreases. As a result, the interaction between neighbouring micro-coils, due to induction phenomena was experimentally measured at the separation distance of 25μm.

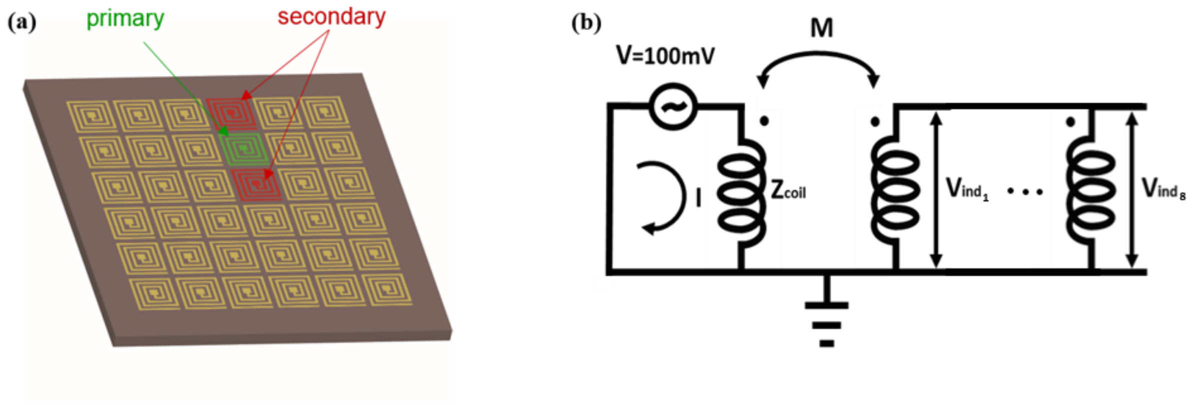

Fig. 8. 4 Inductive measurement methodology and results. (a) **Primary activated micro-coil in the array, shown in green and secondary recording micro-coils in red.** (b) **Schematic of inductive measurement methodology.**

The measurements were performed to chip level inductors, with the use of a probe station (four probe measurement) and a semiconductor parameter analyser (Agilent B1500). The four probe measuring system was ideal for the needs of this experiment as one of the probes was set to ground since all inductors share a common ground connection. The micro-coil under test was activated by another probe, while the two remaining probes were performing passive measurements in the time domain at two neighbouring micro-coils. Figure 8.4a shows the primary activated coil in the array, in green and exemplar secondary ones, in red. The schematic of figure 8.4b, explains the methodology of an inductive measurement. Since two adjacent coils share a common ground, the system is described as an equivalent autotransformer. The voltage in the secondary coils is recorded both for a sinusoidal input and for a series of pulses, at a frequency of 100Hz and amplitude of 100mV. Both input and recorded signals are presented in figure 8.5. The recorded waveforms, for both cases, result from the average between two simultaneous recordings on two adjacent coils to the activated one. The selected secondary coils were chosen as the first neighbours, at the same distance.

The result indicates, higher amplitude on the output for the pulsed signal, which is expected since the time derivative of the pulses is higher, meaning a steeper change, in comparison to the sinusoidal signal. Based on the harmonic case and moving to the frequency domain, the mutual inductance M between two adjacent coils from the relation can be extracted by relation (8.1).

$$\tilde{V} = i\omega M\tilde{I} \tag{8.1}$$

Where $\tilde{V}$ and $\tilde{I}$ are the phasors of voltage and current respectively and ω the angular frequency of the activation signal.

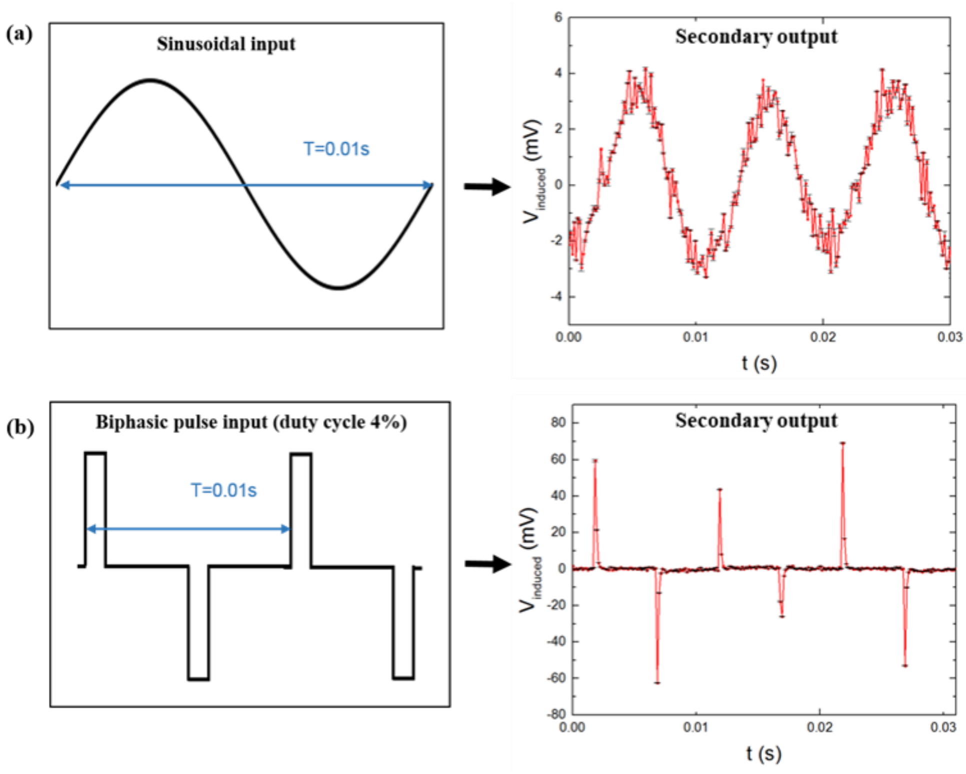

Fig. 8. 5 Two different cases studied. (a) Setting as an input a sinusoidal wave and a series of pulses. (b) The recorded output in both cases, arising as an average of two simultaneous recordings at the secondary coils.

The amplitude of the complex impedance of the micro-coil (Z_{coil}), is accurately described by the resistive component, which is becoming dominant at the low frequency range of 100Hz. Specifically, for the micro-coil under test, the resistance is measured as R=13.7Ohms. Assuming the symmetry of 8 identical first neighbours with R_{tot}=1.71Ohms (total resistance of 8 identical inductors in parallel all with R=13.7Ohms), described by the equivalent circuit of figure 8.4b, the calculated mutual inductance is M=3.3mH.

The high amplitude of the induced voltage in the pulsed case indicates that structures with the separation distance at 25μm, are not ideal for localised magnetic stimulation. This is also in agreement to the observations with the trapping of magnetic beads. However, the needs of the bio-experiment would demand the testing of pulses or signals with a steep time variance and as such, these geometries are avoided and not further processed.

8.3 Magnetic stimulation of neural cells in vitro

In this section the focus is on the experimental procedures of micro-magnetic stimulation testing in neural cells. For this study neuronal cells isolated from hippocampi of rat embryos were used. Firstly some fundamental information of the patch clamping technique, which was used to observe and record cellular activity during the experiment, is presented. The preparation of the samples and the methodology of a successful cell culture are also presented. Finally, the actual bio-experiment is described followed by a discussion with the most important findings and further optimisation of the procedure. All experiments were performed in collaboration with the NeuroChip Laboratory of Prof. Stefano Vassanelli – Dept. Biomedical Sciences, University of Padova, Italy. Within the framework of this research study magnetic stimulation was tested with another type of excitable cells and specifically with cardiomyocytes. Appendix 4 contains information regarding these experiments with neonatal rat ventricular myocytes.

8.3.1 Patch clamping fundamentals

The patch clamping method was proposed in 1976 [145] and prove to be a catalytic method for elucidating how ion channels operate. The idea of the method is to use a micropipette, having a diameter of the order of 1 μm, in order to attach to the surface of the cell. The current changes caused by single ion channels of the cell are measured by voltage clamp method. Soon after the first experiments, the patch clamp techniques were further developed to measure the capacitance of the cell membrane [146]. The patch clamp method has four alternative configurations, namely the cell−attached, whole cell, outside−out and the inside−out configuration. Figure 8.6a summarizes the different configurations and figure 8.6b demonstrates how the different parts of the setup correspond to equivalent resistances or capacitances in an electric equivalent circuit. In the experiment the cell-attached method was used, which disturbs the least the structure and environment of the cell membrane [13] and the whole cell configuration. In cell–attached mode, the micropipette is brought into contact with the cell membrane and a tight seal is formed by suction through the micropipette nozzle. This way possible leakage of current to the environment of the cell is eliminated. Suction is normally released once a firm seal has formed, so that the exchange of ions between the inside of the micropipette and the outside can occur only through the number of channels which are confined in the membrane patch under study. Figure 8.6c shows two examples of a good and a bad quality seal. A bad quality seal is resulting in higher noise levels in the measurement of current. A good quality seal has a resistance of hundreds of MOhms to 1GOhm.

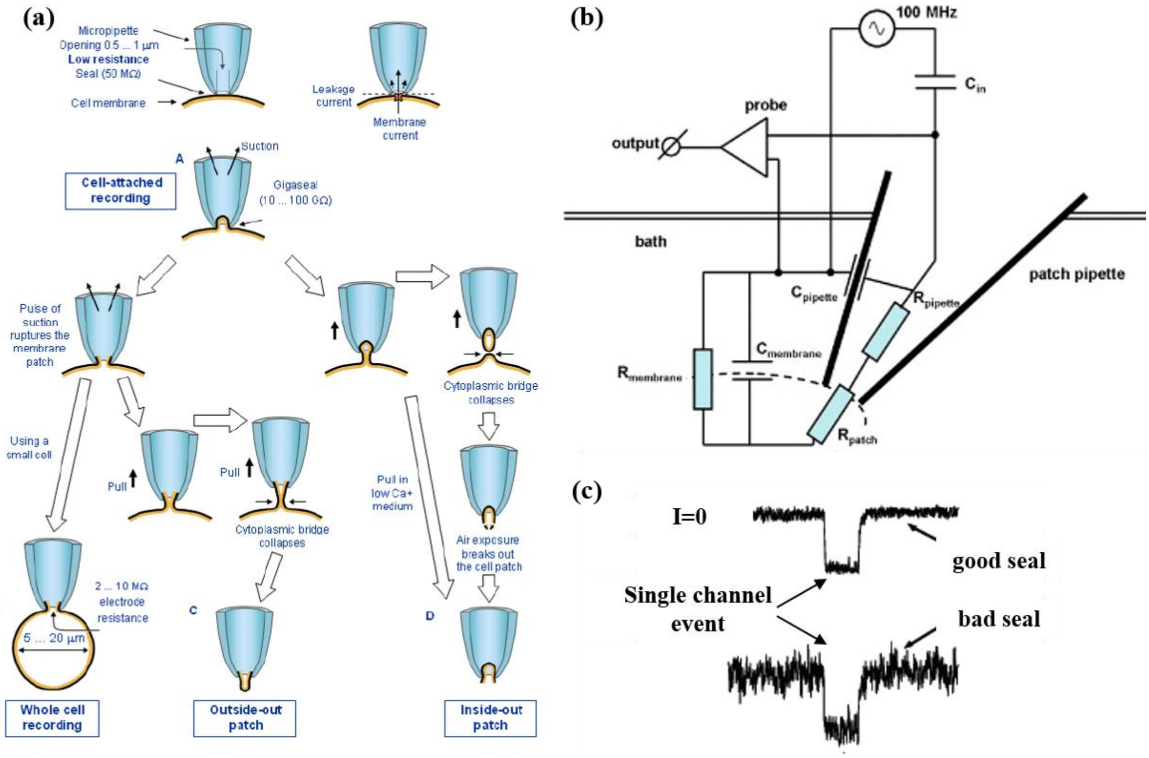

Fig. 8. 6 (a) The four different configurations of patch clamping technique [13]. (b) Equivalent circuit of patch clamping setup [147]. (c) Examples of a good and a bad quality seal. Noise arises from the amount of leakage current to the environment [148].

8.3.2 Cell culturing

As described in chapter 5, the samples prior to their plating with neural cells are coated with a layer of Parylene-C in a thickness of approximately 5μm. Parylene-C is also mildly treated with O_2 plasma to become hydrophilic and aid the adhesion of coating proteins, important for the cell viability. The samples are then put under a sterile laminar hood, where they are sterilised for 30 min with 70% (v/v) ethanol, followed by extensive rinsing with sterile deionized water, drying and additional 30 min sterilization with a germicidal lamp. Neuronal cells isolated from hippocampi of rat embryos were used as described in [149]. Before seeding of the cells, the surface of the samples is coated for 2 hours at room temperature with 20 μg/ml poly-L-Lysine to improve cell adhesion. The density of the neural cells on the plating is approximately 75000 cells/cm^2, with slight differences due to the presence of epoxy inside the cell culturing chamber. The neuronal cultures are monitored from seeding over a 10-day period to assess a good morphology according to what is expected in culture [150]. Successful cultures are ready for patch-clamping between DIV (*Days In Vitro*) 12 and DIV 15 after plating. Figure 8.7 illustrates examples of neural cell networks developed successfully on the micro-fabricated samples, at different stages of culture.

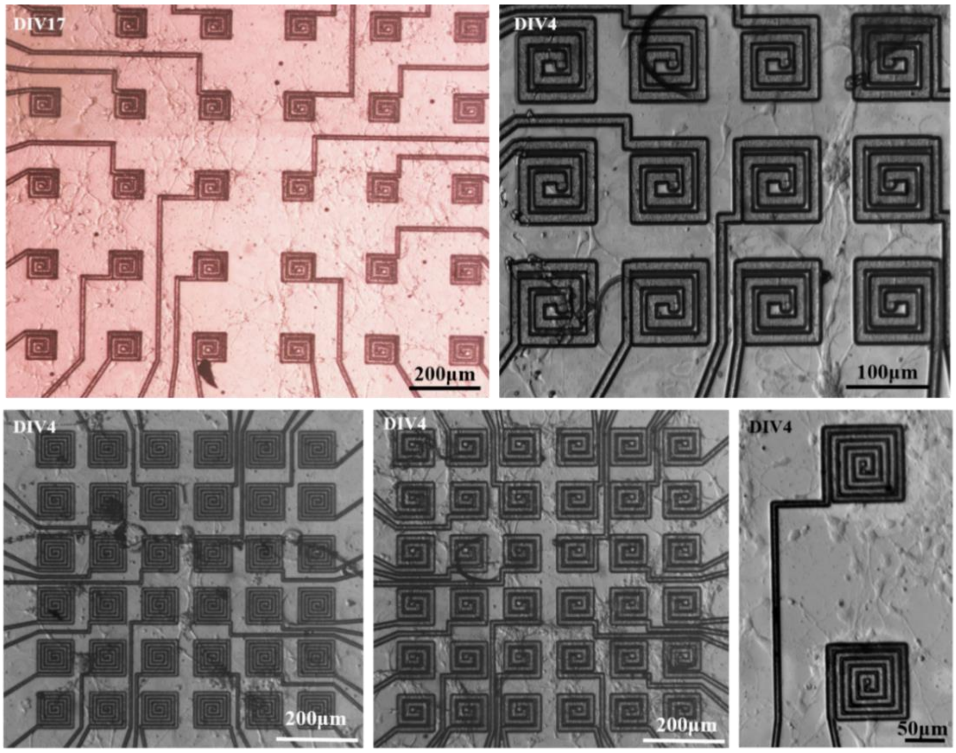

Fig. 8. 7 Examples of successful cell culture in different devices. Neuron populations are organised in networks of increased complexity as they grow healthy.

8.3.3 Bio-experimental procedure

The setup used to activate the micro-coil is similar to that used in the magnetic beads trapping demonstration, presented in section 8.1. Patch-Clamp recordings were performed using an Axopatch 200B amplifier (Molecular Devices, USA) connected to the PC through a BNC-2110

Shielded Connector Block (National Instruments Corp, Austin, TX, USA) along with a PCI6259 PCI Card (National Instruments Corp, Austin, TX, USA). WinWCP (Strathclyde Electrophysiology Software, University of Strathclyde, Glasgow, UK) was used for data acquisition. Micropipettes were pulled from borosilicate glass capillaries (Sutter Instruments Corp., Novato, CA, USA) using a P-97 Flaming/Brown Micropipette Puller (Sutter Instruments Corp., Novato, CA, USA). Intracellular pipette solution and extracellular solution used during the experiments were respectively (in mM): 6.0 KCl, 120 K gluconate, 10 HEPES, 3.0 EGTA, 5 MgATP, 20 Sucrose (adjusted to pH 7.3 with 1N KOH); 135.0 NaCl, 5.4 KCl, 1.0 MgCl2, 1.8 CaCl2, 10.0 Glucose, 5.0 HEPES (adjusted to pH 7.4 with 1N NaOH). The resistance of the micropipettes in extracellular solution, when filled with intracellular solution, ranged from 2.5 to 3.5 MΩ. Figure 8.8 presents the setup used while figure 8.9 shows an example of a neural cell patched at the soma with a seal resistance of 120MΩ. The soma lays just next to the micro-coil, while part of the cell (axonal and dendritic arborisation) is over the micro-coil geometry. The cells tested either is cell-attached or whole cell patch clamp configurations.

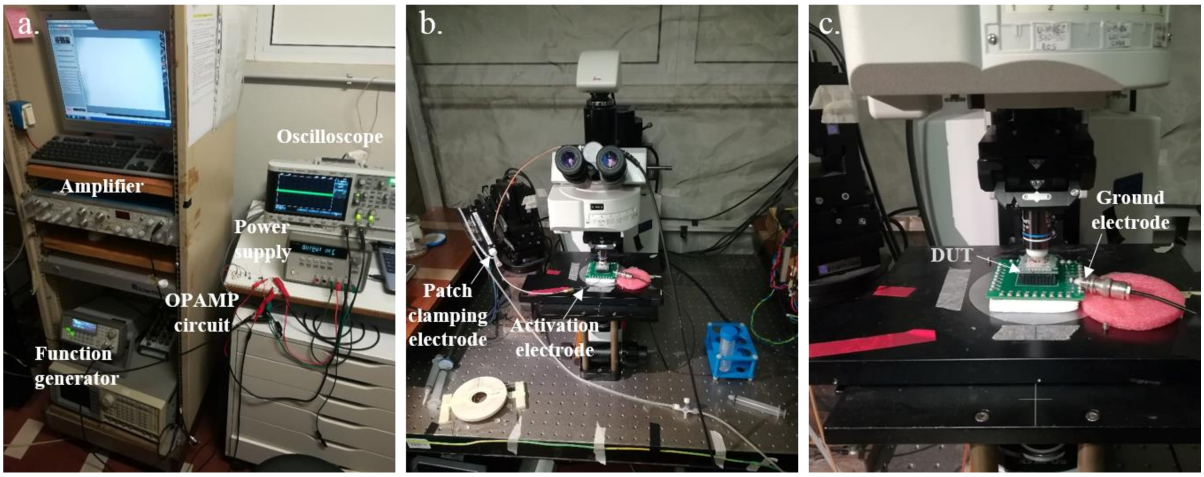

Fig. 8. 8 Activation and patch clamping setup needed in biological validation experiment. (a) **Electrical equipment for the individual address of the micro-coils and the amplifier used to amplify the recorder signal.** (b) **Patch clamping electrode and optical microscope.** (c) **The device under test (DUT) mounted on the PCB platform during testing.**

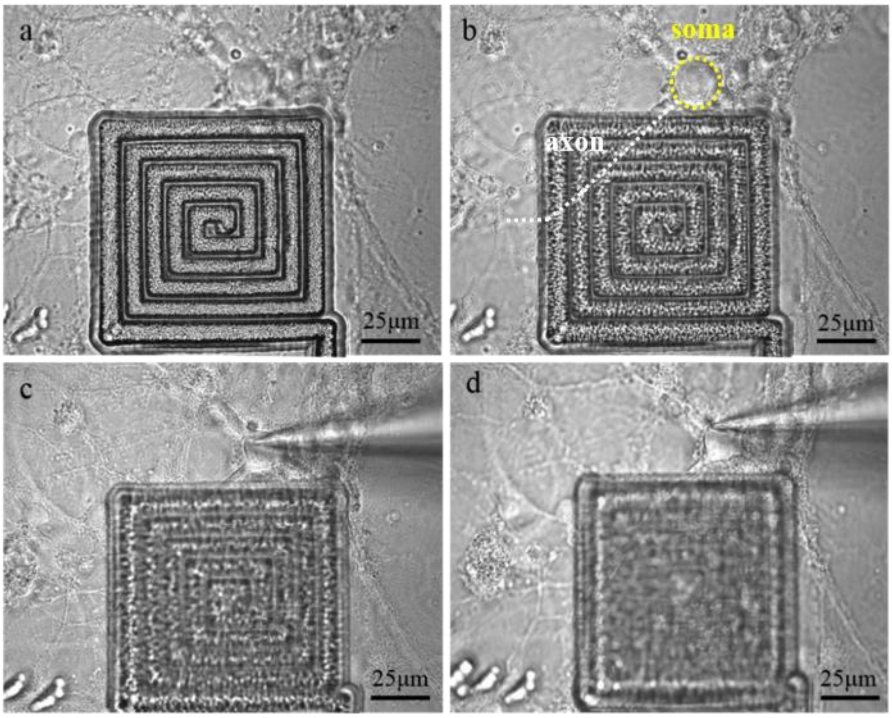

Fig. 8. 9 Example of patch clamping on a properly developed neuron on top of a micro-coil geometry. Images (a-d) at different level of focus: from the micro-coil to the cell.

As magnetic stimulation has not previously reported in hippocampal neuronal cells cultures, the identification of the protocols which lead to cellular activation was not a straightforward procedure. Different parameters such as the frequency and the amplitude of the applied signal had to be tested. Also different manners of delivering the stimulus, continuously or burst of pulses, may affect differently the cell. In every cell tested, the first attempt was to try a free run of gradually increasing in amplitude signal. Signal at this point was delivered continuously to the micro-coil and both sinusoidal and pulses waveforms were tried. Since no action potential was recorded the aforementioned activation parameters were tested. A good starting point for defining possible successful activation protocols was based on two studies, where magnetic stimulation was tested on more robust neural networks, in neural slices or in vivo [1], [3]. Based on these studies, a number of protocols was organised which was saved and run consecutively on all cells tested, in an attempt to automatize the procedure as much as possible. Organising the testing options in an efficient way was important since the lifetime of a patched cell is limited to approximately 20-30minutes. The type of stimulus for which neuronal activity was observed, is depicted on figure 8.10a and consists of a full sinusoidal pulse at 3kHz repeated at a frequency f_r, which on the experiment was set 10Hz, 100Hz or 1kHz. The amplitude of the applied voltage in the micro-coil was controlled dynamically for every protocol and started from lower values in every case moving gradually to the maximum possible current a micro-coil could hold. The micro-coil geometry for which cell activity was observed (in whole cell configuration with 1GOhm seal) is the one on figure 8.9 with a side length of 100μm, metal track width 9μm and thickness 2μm, which based on the electrothermal characterization is expected to have a deterioration limit at a current amplitude >100mA. In the first attempt, activation was attempted on a cell at its resting conditions but neuronal activity was not observed in this case either. Thus it was decided to depolarise the cell, a procedure which sets the resting voltage of the membrane closer to the threshold of activation. Four different depolarisation levels were tried, defined by the depolarisation current 10, 100, 400 and 600pA, with 600pA representing the closer setting of transmembrane potential to threshold. For all depolarisation cases a cell response was observed. Figure 8.10b shows two examples of action potential recordings, while in both cases stimuli artifacts are also obvious at the repetition rate of each case.

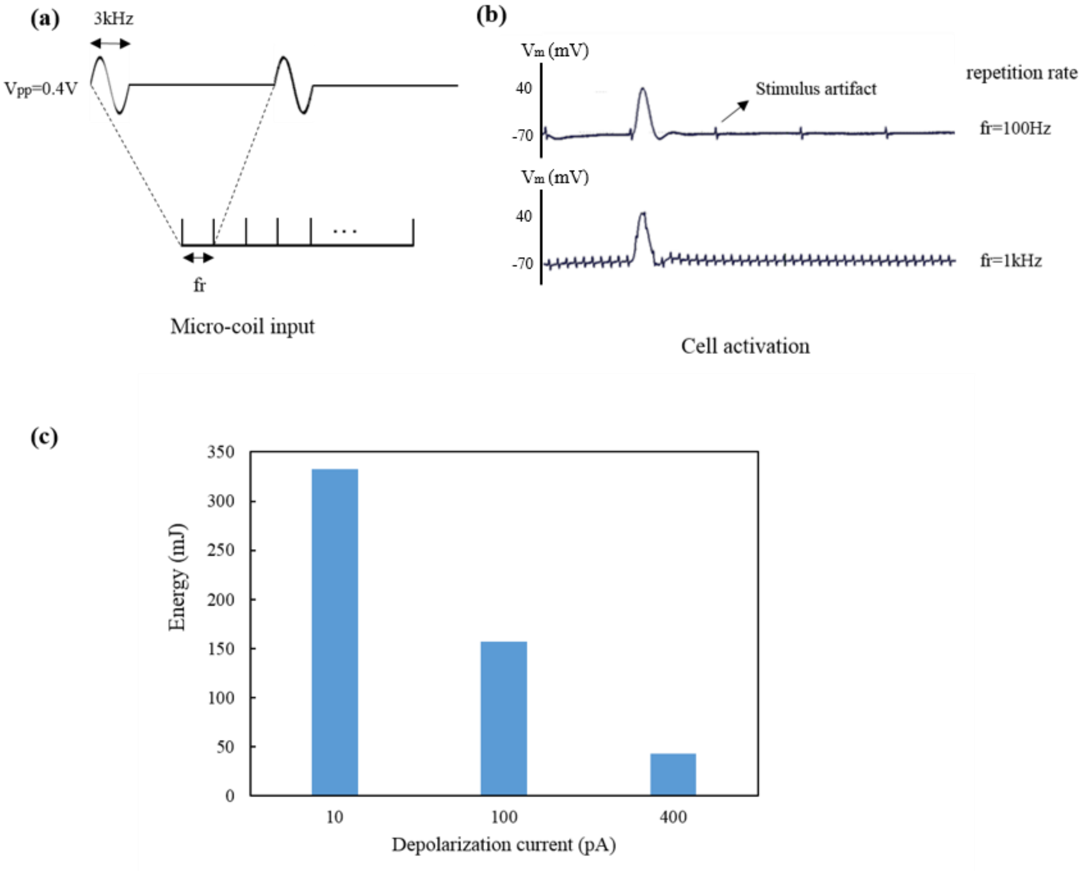

Fig. 8. 10 (a) Schematic representation of stimulus input signal to micro-coil. (b) Examples of action potential recordings at different stimulus repetition rates. (c) The energy offered to the system until observation of an action potential for three depolarisation currents: 10pA, 100pA and 400pA.

The repetition rate of 1kHz, was studied the most and it was further observed that the smaller the depolarisation, the more time was needed for the cell to respond with an action potential. The time from the initial turning on of the micro-coil up to the point where an action potential was observed is determined and translated into the energy offered to the system. In all experiments the micro-coil signal amplitude was set to 0.4V peak to peak. Figure 8.10c summarises the energy calculation for each depolarisation level. The depolarisation of 600pA was excluded from the calculations as cell was very sensitive not only to the stimulus but also to network interactions and cell activity which was very strong. The energy footprint of the device (assuming the 1kHz cycle) is on the range of existing magnetic stimulation attempt with commercially available sub-millimetre scale solenoids, but still significantly higher in comparison to alternative electric stimulation technologies [3]. Finally, the post processing of the recorded data shows that in some cases neuronal activity continued to be present for some time after the micro-coil input signal went off and specifically, the higher the depolarisation the more time was needed for the cell to return to rest.

8.3.4 Discussion

Analysis of the data recorded indicate that micro-coil can elicit neural activity in a neuronal cell, for all the cases of depolarisation tested. Moreover, there seems to be an interplay between the extent of depolarisation and the energy offered to the system until activity is recorded. However, neuronal activity was not observed at resting cell condition which indicates that further optimisation of the procedure is needed.

The bio-experiment brought to the foreground many different aspects for optimisation. A challenge faced during patch clamping was the difficulty to distinguish the cells when lying on top of a micro-coil. The complexity of both the structures and the cell morphologies in combination with the lack of contrast on the observation through the optical microscope prove to be an insurmountable obstacle in the patch clamping of such cells. In contrast, cells found in between of coil geometries in an array were preferred, especially if part of their branching was located above a micro-coil geometry. This issue certainly sets out of study the most important areas of an array, in terms of micro-magnetic stimulation efficiency, where the asymmetry of the induced electric field is the strongest. A possible solution would be to use a patterned Parylene-C layer, functionalised with O_2 treatment, to attract neural adhesion only on the hydrophilic areas.

Further optimisation of the overall fabrication procedure is needed in order to improve the yield of successful samples for testing. Significant difficulties with the viability of neural cells on the surface of Parylene-C surface were faced. More specifically, observation of failed samples indicate that there could be an opening in the Parylene-C film, arising either during fabrication, cleaning or culturing. A possible opening exposes the toxic epoxy leading cells to detach from the substrate material and die. The reason behind this deterioration on the quality of the polymeric membrane was not possible to identify despite several attempts. The primary focus was on increasing the Parylene-C thickness to be sure that possible porosity of the deposited film is eliminated. A second idea was to avoid any cleaning agent material, which could be harsh for the Parylene-C film. Samples were expected to be re-used after a cleaning procedure, however in almost 70% of the cases this was not feasible. This possibility that 1% Tickopur R33 (Bandelin) used as cleaning agent after the experiment could be harsh for the Parylene-C film was supported by the fact that samples became non-functional every time after their first plating and cleaning. In order to avoid toxicity issues and improve cell viability, the toxic epoxy beneath the Parylene-C layer, was decided not to be replaced, as it acted as a marker of possible cracks in the insulating coating. In other words, the unwanted toxic effects arising from the use of the epoxy became a helpful indication to distinguish samples with a good quality Parylene-C coating, which can accurately (no leakage from the insulator) be chosen for testing of magnetic stimulation. Despite the several trials, the standardisation of the fabrication procedure and/or methods of treatment of the finalised sample are still far from optimum. Further optimisation might include the substitute of Parylene-C by another insulating and bio-compatible polymeric material, such as PDMS.

Finally, an important factor which deserves a separate study is related to the mechanisms behind cellular activation. As described in chapter 2, a localised temperature gradient can act as well as a stimulus and elicit neuronal activity. The fact that the micro-coils face losses due to Joule heating, might indicate that the mechanism of stimulation is thermal. A way to support that magnetic stimulation is the mechanism behind cell activation, is to study cells in the vicinity of a micro-coil with different orientation with respect to its position. Magnetic stimulation efficiency is expected to be orientation dependant. This type of testing in vitro can be achieved with tissue slices, where neural morphologies are developed in a three dimensional manner, rather than in a cell culture where all cell morphologies are developed in a planar configuration.

8.5 Summary

The focus of chapter 8 was on a series of experiments used to assess the functionality of the fabricated micro-arrays. Specifically, the trapping of magnetic nanoparticles was achieved indicating the spatial resolution of the magnetic field profiles above the micro-coils. The experiments with the magnetic nanoparticles, indicated also the problematic behaviour of the denser arrays with micro-coils fabricated at a minimum fabricated distance of 25μm. Moreover, using a transformer equivalent characterization method the inductive coupling between neighbouring coils was measured at the case of minimum separation distance. The inductive measurements were performed both for a sinusoidal signal and for a pulsed one. The latter is much of an interest as in the actual bio-experiment the activation signal would be delivered in a pulsed manner. The activation setup developed to activate the micro-coils is described, with a special note on the optimisation methods of power transfer from the input source to the low resistive mirco-inductors. Finally, the process of biological validation is presented in detail, from the successful cell culturing on the samples to the patch clamp recordings and the conditions which led to cellular activity response. The chapter finally discusses the challenges met in the bio-experiment and further optimisation methods of the whole procedure.

Chapter 9

Conclusions and Future Work

9.1 Overview of the accomplished work

This research study focused on the miniaturization of TMS principle in the microscale. The idea was to develop a 2-D micro-magnetic neuro-stimulating platform for in vitro applications, which consists of 36 electromagnets in a planar array configuration. The micro-coils in the array are individually addressable to create highly localized and dense magnetic field distributions, acting as a magnetic equivalent of microelectrode arrays developed for neural cell stimulation applications. The contactless manner of stimulation, the elimination of electrode-tissue degradation phenomena and the fact that the electromagnets were be totally insulated with a bio-inert material, without significantly losing their efficiency are some of the most important advantages of the method. This approach also overcomes the biofouling related issues which limit the functionality of micro-electrode arrays. On the other hand, the spatial resolutions cannot be as high as in micro-electrode arrays due to limitations of the inductive behavior of the electromagnets. The proposed device could serve as a recording component, however it has not been optimized for this application during this research study. The main challenge of this novel non-invasive neuro-stimulation tool is that micro-coils need to hold certain current capacity, so as to induce an electric field strong enough to stimulate cells, as cells need to reach their threshold potential in order to fire.

Throughout this study all the steps towards the design and construction of a micro-magnetic platform were presented. The realization of a planar 6x6 array of micro-coils is chosen in order cover a wide area in a cell cultures. The micro-coils in the arrays are creating magnetic flux density profiles with a spatial resolution equivalent to the micro-coil size. Besides the fabrication development, different experiments were performed to characterize the behaviour of the micro-arrays, such as electrical characterization, electrothermal testing and magnetic nanoparticle trapping.

Chapters 2 and 3 present the literature review for this study. Chapter 2 gives the important details regarding the electrophysiology of neural cell and clearly shapes the biophysical framework of this study. It also focuses on different mechanisms and techniques to achieve neural stimulation. Chapter 3 focuses only on magnetic stimulation and the mechanism of this method from macroscale to microscale. It summarizes the recent developments in micro-scale magnetic stimulation technologies. It finally presents, the-state-of-the-art in the fabrication of planar micro-inductors.

Chapter 4 presents a simulation study using COMSOL Multiphysics focusing on the electromagnetic and electrothermal behavior of micro-coil geometries. At another point, it discusses important considerations related to micro-fabrication and presents the design of the photolithographic masks.

Chapter 5 summarizes all the micro-fabrication techniques used to obtain planar inductor on Si wafers. Also describes in detail the encapsulation of the micro-chip into a biocompatible platform. The material chosen is Parylene-C which is a bio-inert material with excellent insulation properties. Finally the PCB designed to individually access the micro-inductors is presented.

Chapter 6 focuses on the electromagnetic and electrothermal benchmarking of the devices. An impedance frequency sweep is performed to monitor the expected behavior from the inductors. The inductors have small resistive values (≈10 Ohms) at lower frequencies, while at higher MHz frequencies, where their reactance increases, the impedance reaches approximately 200 Ohms. Impedance is further analysed to inductance, resistance and quality factor and a relative comparison between different geometries is presented. Also the influence of the coating layer and the thickness of the electroplated material are studied with the same methods of characterization. A second very important scope of this chapter, was a study of the electrothermal phenomena, such as Joule heating and electromigration, which lead to the degradation of the micro-coils and limit their durability. The limits in the maximum current capacity that specific geometries could hold without being affected are extracted and presented. As expected, micro-coils with smaller metal track cross-sections show failure points at lower currents. The smallest cross-section tested was $3.42\mu m^2$ and the failure current corresponds to 24mA. On the other hand, cross-sections larger than $10.62\mu m^2$ do present any failure within the range of the 100mA tested. Also a comparison of the median time of failure of each sample, due to electromigration, is presented.

In Chapter 7 a biorealistic study and testing of the proposed device was performed. Simulations with a finite element method (FEM) software and modeling with NEURON software, are used as a validation method of the capabilities of the platforms. Additionally, the testing of the micro-coil with a phantom gel, which mimics the electric properties of brain tissue, is presented, as a first step towards the bio-experiment. The electric currents induced in the phantom gel during the activation of the micro-coils are measured and compared with thresholds in literature. Both studies support that the micro-coils can elicit activity in a cell morphology or tissue.

Finally, Chapter 8 summarizes successful demonstration of the functionality of the arrays. Magnetic nanoparticle trapping shows the spatial localization of magnetic field created in the vicinity of the micro-coils. These experiments, became the starting point to further inductive measurements between adjacent coils in the same array, in an attempt to quantify the inductive coupling. These measurements led to the exclusion from biological testing of the micro-arrays with separation distance of 25μm, as the interaction between neighbouring micro-coils was maximized and disrupted the response of a single micro-coil. Last but not least, the biological testing with hippocampi neural cells extracted from rat embryos is described in detail. Information of the process followed in the samples before and during the cell culturing was given and the methods and results from the biological experiment of magnetic stimulation in vitro were presented. The cell behavior was recorded with patch clamping techniques. Based on these finding, there is an interplay between the depolarisation level and the energy that is offered to the system to record activity. The findings are preliminary, but encouraging for the functionality of the platforms. To conclude, the further optimization of the substrates to overcome present limitations and eliminate the problematic development of the cells on the substrates was discussed.

9.2 Contributions

This research sets up the scheme for an alternative method to control the stimulation of neural cells in vitro having at the same time as a main advantage the lack of direct contact between the electrode and cell medium. The main contributions of this work lay in the following areas:

- The proposal and design of a novel device for two dimensional magnetic stimulation in vitro. A full description of the fabrication procedure was presented both for the fabrication of the planar micro-coil geometries on a chip and for the further encapsulation of the chip into a biocompatible platform. Figure 9.1 summarizes the recent approaches to micro-magnetic stimulation and highlights the advantage of the prototyped devices. Firstly, it is the smallest fabricated device for magnetic stimulation with a spatial resolution of 50μm or 100μm, depending on the type of coil chosen. This is translated into a very good resolution and control of the activation area in comparison to other studies. Up to now, the majority of the studies were using commercially available inductors for magnetic stimulation, introducing limitations relevant to their big size. At the same time, the two dimensional array assures that this device could potentially cover the wider area of interest (large effective area).

- The construction of a phantom gel mimicking the brain tissue electric properties for low frequency applications and the benchmarking of the samples with the use of the composed phantom.
- The electrothermal study as a novel approach to study the deterioration of the electromagnets under a bio-realistic activation scheme.
- Testing the response of neural cell populations to microscale magnetic stimulation was the first time that somebody witnessed neural activity in cell cultured developed morphologies, even with the assistance of a preferable depolarization voltage.

Year	Proposed device	Application	Resolution	Work
2012	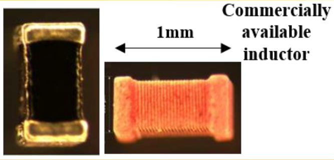	In vitro	Limited by inductor's size ≈1mm	*Bonmassar, G. et al.,* Nat.Commun. [9]
2013	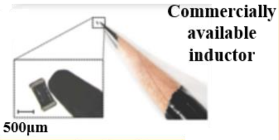	In vivo	Limited by inductor's size ≈1mm	*Park, H. J. et al.*. Nat. Commun. [11]
2015	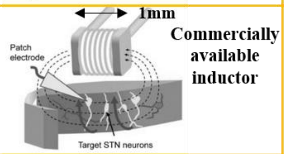	In vitro	Limited by inductor's size ≈1mm	*S. W. Lee and S. I. Fried*, IEEE Trans. Neural Syst. Rehabil. Eng. [10]
2016	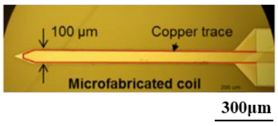	In vitro & In vivo	100μm	*S. W. Lee et al.*, Sci. Adv. [97]
2017	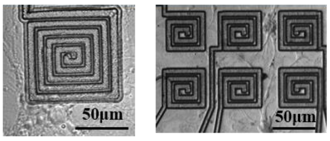	In vitro	50μm or 100μm (With effective area: from 425μm x 425μm to 1600μm x1600μm)	*Rizou et al.*, BioCas 2016 [143] *Rizou et al.*, BP&EX [144]

Fig. 9. 1 Recent studies of micro-magnetic stimulation tested in neural cells and their relevant information. **[151], [152]**

9.3 Future ideas and applications

There is a vast variety of future orientations for the further enhancement of the capabilities of the micro-coil platform. A number of possible directions are presented below.

- Further optimisation in the biocompatible packaging to improve the viability of the cells and make samples re-usable. The optimisation could be based on the use of alternative biocompatible materials, such as PDMS.
- Additional biological characterisation experiments are needed to assess and optimise the functionality of the devices. Further testing would indicate activation protocols which might be more efficient and lead to activation even without depolarisation of the cell.
- The design of the chip could be transferred to flexible substrates, finding possible applications in the field of implantable bio-devices. A magnetic equivalent of a micro-electrode array could be developed as a powerful implantable neuro-stimulating tool. New approaches on neuroprosthetic devices attract significant attention from pharmaceutical companies which have set new goals and develop the new generation of medicine, the so called electroceuticals.
- Another future alternative could be the development of a hybrid microelectronic /microfluidic system that would contain the designed micro-coil array chip and a microfluidic channel fabricated on top of the chip. The micro-coils would generate local magnetic fields for both control of the motions of magnetically-tagged neural cell and stimulation, while the microfluidic channel would provide a biocompatible environment for the maintenance of the biological cells.
- The possible future fabrication process could also include structures with transparent materials, in order to make the chips also compatible with backlight microscopes.

Appendix 1

Publication record

Parts of this research work have been published and presented as listed below:

Peer reviewed Journal:

- M. E. Rizou and T. Prodromakis, “Magnetic stimulation in the microscale: the development of a 6x6 array of micro-coils for stimulation of excitable cells in vitro” , *Biomed. Phys. Eng. Express*, Dec. 2017, vol4, no 2, pp 025016.
- M. E. Rizou and T. Prodromakis, “Electrothermal deterioration factors in gold planar inductors designed for microscale bio-applications”, *Microelectron. Eng*, Oct. 2018, vol 197, pp 61-66.

Reviewed Conference Papers:

- M. E. Rizou and T. Prodromakis, “A planar micro-magnetic platform for stimulation of neural cells in vitro,” *Proc. 2016 IEEE Biomed. Circuits Syst. Conf. BioCAS 2016*, pp. 34–37, 2017.

Conference Contributions:

- “Magnetic stimulation in the microscale: the development of a 6x6 array of micro-coils for stimulation of excitable cells in vitro”, M.E. Rizou, T. Prodromakis, Biofabrication Conference, Winston-Salem, NC, USA, 2016. (Oral presentation)

Appendix 2

Fabrication of the phantom solution

Based on the study [137], the same protocol for fabricating a gel that simulates the electric permittivity and conductivity of brain tissue has been used. A difference to the original recipe, is that the amount of HEC was increased by four times in order to achieve a more semi-solid consistency of the gel. As it is mentioned on [137], this is not affecting the electric properties of the gel. The recipe used to compose the phantom is described below. The table with the ingredients is also attached here for convenience.

Table A2.1 The ingredients needed for the fabrication of the brain tissue phantom solution. All quantities are given at percentage by weight.

	% by weight
Sugar	54.5
Water	39.2
HEC	3.9
Salt (NaCl)	2.4
Bacteriacide	0.1

Fabricating procedure of phantom gel:

1. All the ingredients are weighted accurately.
2. In a beaker, water is heated to 40^{o}C.
3. The amount of NaCl and bacteriacide (Quaternium 15) are added while stirring.
4. Sugar is added while stirring at a low speed to prevent bubble formation in the solution.
5. When the solution has a uniform temperature the gel agent hydroxyethylcellulose (HEC) is added.
6. The solution is removed from heat and stirring is continued until it thickens.
7. Finally, the mixture is left to cool to room temperature.

The fabricated gel is showed in figure A2.1.

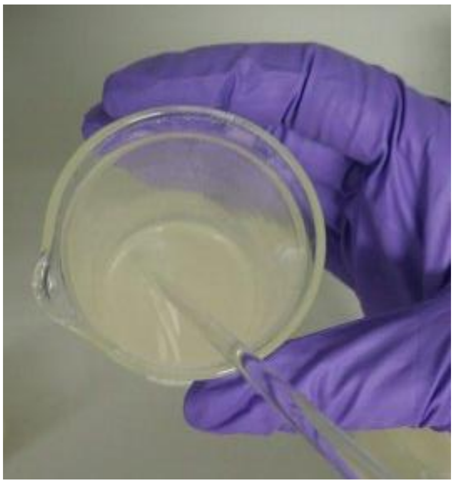

Fig. A2. 1 The composed phantom solution which mimics the electric properties of neural tissue.

Appendix 3

Database of electric properties of human tissue

The values of electric permittivity and conductivity of the neural layer in COMSOL software, were chosen based on a web application/database [107]–[109], which calculates the dielectric properties of human body tissue in a frequency range from 10Hz-100GHz. The results are for two different values for neural tissue that correspond to grey and white matter. In an attempt to be as closer to reality as possible, the mean value of grey and white matter values was used, depending on the frequency under study. As it has already mentioned, another approach could be the use of water's electric permittivity and conductivity in the layer that represents the neuron in COMSOL, as the main ingredient of neural cells is water. However, this approach was avoided as it would lead to an even rougher estimation. The following graphs describe the behaviour of electric permittivity and conductivity in grey and white matter, over the whole frequency range. For more information, an online application is available [153], where the results of Gabriel et al have been used and are ready to be exported dynamically.

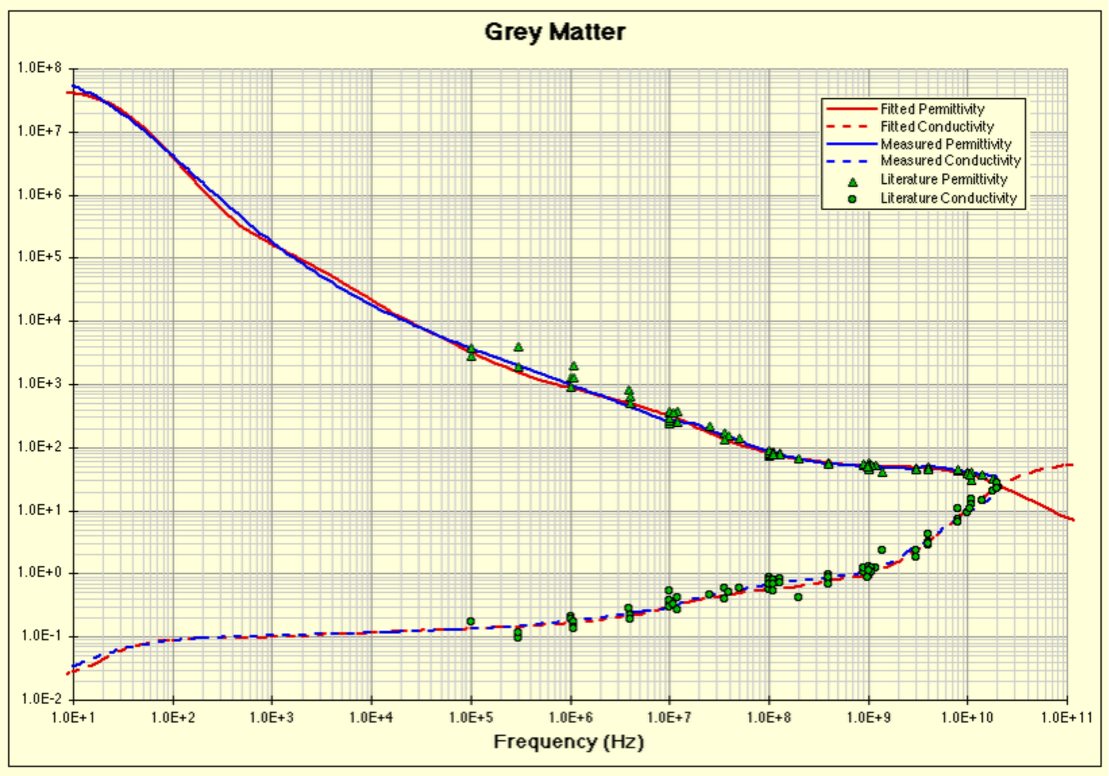

Fig. A3. 1 The dependence of electric permittivity and electric conductivity of grey matter in frequency.

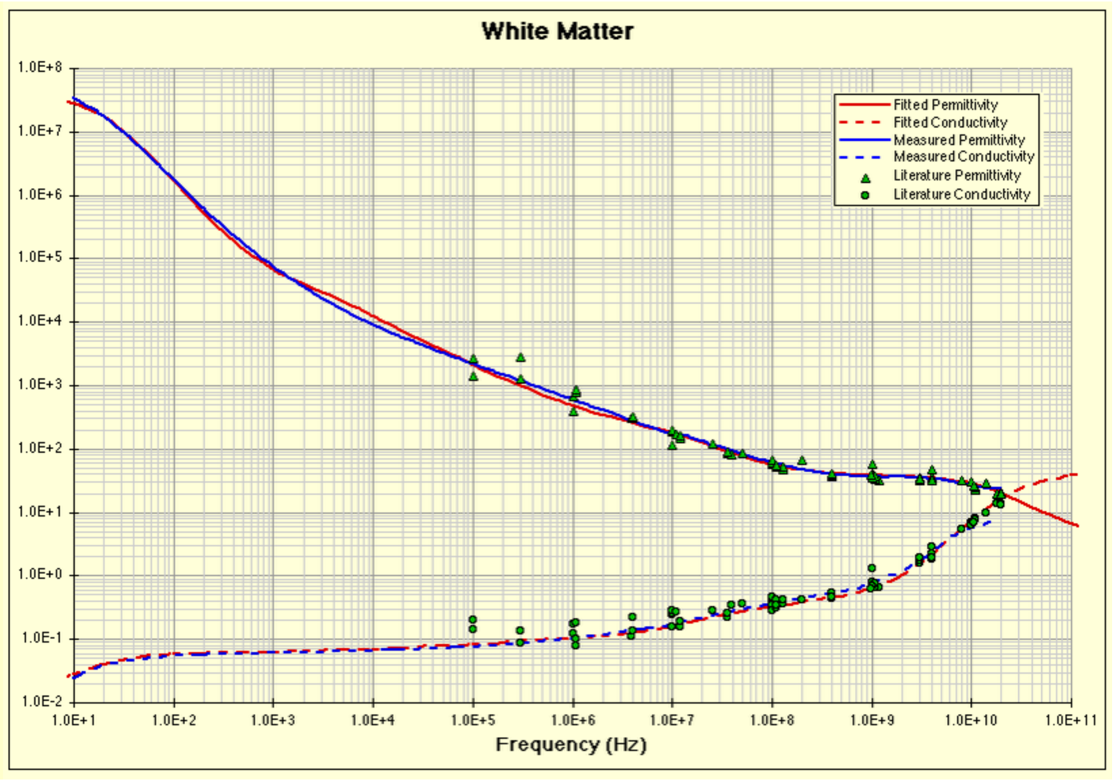

Fig. A3. 2 The dependence of electric permittivity and electric conductivity of white matter in frequency.

Appendix 4

Magnetic stimulation of cardiac cells in vitro

Within the framework of this study, magnetic stimulation was attempted with another type of excitable cells. In collaboration with Prof. Cesare Terracciano (Faculty of Medicine, Hammersmith Hospital, Imperial College London) magnetic stimulation was tested on neonatal rat ventricular myocytes (NRVM). The motivation behind this study was based firstly on the fact that there are no relevant studies in literature regarding the magnetic stimulation of cardiac cells. Moreover, the cell culturing of cardiac cells demands less time and could give a confirmation of the biological suitability of the samples and a quicker standardization protocol, which includes the cleaning procedures, the type of sterilisation and the plating of adhesion proteins on top of the O_2 treated Parylene-C surface layer. Finally, the whole circuit developed for the activation of the micro-inductors in the biological experiment could be tested and optimised prior to the neuronal testing in Italy.

The standardisation protocols for this type of cells was straightforward. After two attempts of cell plating collagen was plated as an adhesion protein and finally successfully grow cardiac cell populations on Parylene-C. Neonatal cardiomyocytes turned out to be a lot more tolerant to the materials used in the sample and more specifically to the bio-compatible and hydrophilic surface layer of Parylene-C which was expected by similar studies of cardiomyocyte cell culturing [154], [155]. The cleaning and sterilization protocol has the following steps:

- Sterilisation of the cell culture chamber with ethanol for 10 mins.
- Wash area three times with purified water.
- Coating of Parylene-C surface film with collagen (dissolved in acetic acid) for 1 min.
- Wash in water for 1.5 hours.
- Sterilisation with UV light for 1 hour.
- Plating of the cells in the medium.

The cardiac cell activity was assessed with a fluorescent microscope and specifically with the monitoring of Ca^{2+} concentrations in the cell medium. Figure A4.1 shows the fluorescent microscope in the setup during the biological testing. The magnetic stimulation testing on the preliminary attempts was not successful. A significant problem faced was related to the method of activity assessment. Specifically, the network interactions in the culture of neonatal cardiomyocytes was quite strong and it was difficult to distinguish between the network activity and a possible activity triggered by the device. Better results, could be achieved with adult cardiomyocytes which usually present less significant network communication. Furthermore, magnetic stimulation has not been studied in cardiac cells and the activation protocols in this case are an unexplored region of possibilities. Attempts with different testing signals were similar to the biological experiment with neural cells, but no activity was observed. Finally, it is useful to highlight that NVRM are normally electrically field stimulated at 1 Hz using a significantly high voltage of 20V in the cell medium with a volume of approximately 0.2cm^2 (size of cell culturing chamber). This is an indication of possible high energy requirements that need to be offered to the system to observe activity. If this is the case, then the micro-scale inductors cannot induce an important electric field to elicit cellular activity. Further testing is needed to better understand and optimise magnetic stimulation in cardiac cell populations.

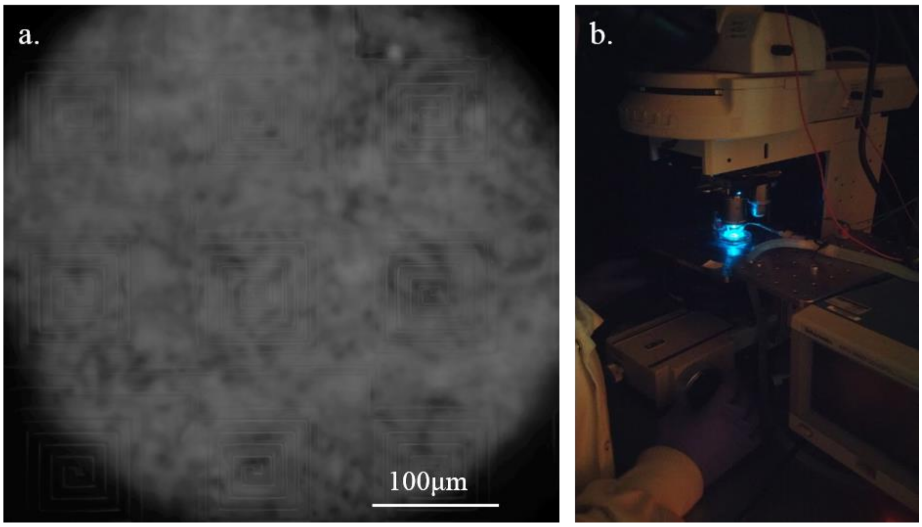

Fig. A4. 1 Testing magnetic stimulation in cardiac cells. (a) Cardiac cells developed on the planar micro-coil arrays. (b) The fluorescent microscope in the setup is used to monitor the activity of NVRM.

References

[1] S. W. Lee, F. Fallegger, B. D. F. Casse, and S. I. Fried, “Implantable microcoils for intracortical magnetic stimulation,” *Sci. Adv.*, vol. 2, no. 12, pp. e1600889–e1600889, 2016.

[2] G. Bonmassar, S. W. Lee, D. K. Freeman, P. Miloslav, S. I. Fried, and J. T. Gale, “Microscopic magnetic stimulation of neural tissue,” *Nat. Commun.*, vol. 3, no. May, p. 921, Jan. 2012.

[3] S. W. Lee and S. I. Fried, “Suppression of Subthalamic Nucleus Activity by Micromagnetic Stimulation,” *IEEE Trans. Neural Syst. Rehabil. Eng.*, vol. 23, no. 1, pp. 116–127, 2015.

[4] H. J. Park, G. Bonmassar, J. A. Kaltenbach, A. G. Machado, N. F. Manzoor, and J. T. Gale, “Activation of the central nervous system induced by micro-magnetic stimulation.,” *Nat. Commun.*, vol. 4, p. 2463, Jan. 2013.

[5] S. W. Lee, F. Fallegger, B. D. F. Casse, and S. I. Fried, “Implantable microcoils for intracortical magnetic stimulation,” *Sci. Adv.*, vol. 2, no. 12, pp. e1600889–e1600889, 2016.

[6] A. T. Barker, R. Jalinous, and I. L. Freeston, “Non-Invasive Magnetic Stimulation of Human Motor Cortex,” *The Lancet*, vol. 325, no. 8437. pp. 1106–1107, May-1985.

[7] L. L. Herrmann, K. P. Ebmeier, L. L. Hermann, and K. P. Ebmeier, “Transcranial magnetic stimulation,” *Psychiatry*, vol. 5, no. 6, pp. 204–207, 2006.

[8] S. Reardon, “Electroceuticals spark interest.,” *Nature*, p. 1982, 2014.

[9] “COMSOL Multiphysics.” [Online]. Available: https://www.comsol.com/. [Accessed: 05-Jun-2018].

[10] “NEURON coding,” 2016. [Online]. Available: www.neuron.yale.edu/neuron. [Accessed: 25-Jun-2018].

[11] “Neural cell anatomy.” [Online]. Available: https://askabiologist.asu.edu/neuron-anatomy. [Accessed: 25-Oct-2018].

[12] T. H. Bullock, “Initiation of nerve impulses in receptor and central neurons,” *Rev. Mod. Phys.*, vol. 31, no. 2, 1959.

[13] J. Malmivuo and R. Plonsey, *Bioelectromagnetism: principles and applications of bioelectric and biomagnetic fields*. 1995.

[14] J. V. Tranquillo, *Quantitative Neurophysiology*, vol. 3, no. 1. 2009.

[15] A. L. Hodgkin and A. F. Huxley, “A quantitative description of membrane current and its application to conduction and excitation in nerve,” *Bull. Math. Biol.*, vol. 52, no. 1–2, pp. 25–71, 1990.

[16] M. S. Breedlove and N. V. Watson, *Biological Psycology*, 7th ed. Sinauer Associates, 2013.

[17] F. Rattay, “Ways to approximate current-distance relations for electrically stimulated fibers.,” *J. Theor. Biol.*, vol. 125, no. 3, pp. 339–349, 1987.

[18] F. Evans and R. Plonsey, “Simulation of comparative thresholds for neural and cardiac tissue,” *18th Annu. Int. Conf. IEEE Eng. Med. Biol. Soc. 1996.*, pp. 321–322, 1997.

[19] A. B. Frazier, D. P. O’Brien, and M. G. Allen, “Two dimensional metallic microelectrode arrays for extracellular stimulation and recording of neurons,” in *Proceedings IEEE Micro Electro Mechanical Systems*, 1993, pp. 195–200.

[20] E. Fernández *et al.*, “Acute human brain responses to intracortical microelectrode arrays: challenges and future prospects.,” *Front. Neuroeng.*, vol. 7, no. July, p. 24, Jan. 2014.

[21] B. V. Zemelman, G. A. Lee, M. Ng, and G. Miesenböck, “Selective photostimulation of genetically chARGed neurons,” *Neuron*, vol. 33, no. 1, pp. 15–22, 2002.

[22] M. Häusser, “Optogenetics: the age of light,” *Nat. Methods*, vol. 11, no. 10, pp. 1012–1014, Sep. 2014.

[23] H. Huang, S. Delikanli, H. Zeng, D. M. Ferkey, and A. Pralle, “Remote control of ion channels and neurons through magnetic-field heating of nanoparticles,” *Nat. Nanotechnol.*, vol. 5, no. 8, pp. 602–606, 2010.

[24] M. G. Shapiro, K. Homma, S. Villarreal, C.-P. Richter, and F. Bezanilla, “Infrared light excites cells by changing their electrical capacitance,” *Nat. Commun.*, vol. 3, p. 736, 2012.

[25] L. R. Gavrilov, “Use of focused ultrasound for stimulation of nerve structures,” *Ultrasonics*, vol. 22, no. 3, pp. 132–138, May 1984.

[26] S. J. Norton, “Can ultrasound be used to stimulate nerve tissue?,” *Biomed. Eng. Online*, vol. 2, pp. 1–9, 2003.

[27] C. J. Wright, J. Rothwell, and N. Saffari, “Ultrasonic stimulation of peripheral nervous tissue: An investigation into mechanisms,” *J. Phys. Conf. Ser.*, vol. 581, no. 1, pp. 0–12, 2015.

[28] D. Seo *et al.*, “Wireless Recording in the Peripheral Nervous System with Ultrasonic Neural Dust,” *Neuron*, vol. 91, no. 3, pp. 529–539, 2016.

[29] C. A. Thomas, P. A. Springer, G. E. Loeb, Y. Berwald-Netter, and L. M. Okun, “A miniature mictroelectrode array to monitor the bioelectric activity of cultured cell.” .

[30] F. Hofmann and H. Bading, “Long term recordings with microelectrode arrays: studies of transcription-dependent neuronal plasticity and axonal regeneration.,” *J. Physiol. Paris*, vol. 99, no. 2–3, pp. 125–32, 2006.

[31] F. Lanté, M.-C. de Jésus Ferreira, J. Guiramand, M. Récasens, and M. Vignes, “Low-frequency stimulation induces a new form of LTP, metabotropic glutamate (mGlu5) receptor- and PKA-dependent, in the CA1 area of the rat hippocampus.,” *Hippocampus*, vol. 16, no. 4, pp. 345–60, Jan. 2006.

[32] J. Cang, R. C. Rentería, M. Kaneko, X. Liu, D. R. Copenhagen, and M. P. Stryker, “Development of precise maps in visual cortex requires patterned spontaneous activity in the retina.,” *Neuron*, vol. 48, no. 5, pp. 797–809, Dec. 2005.

[33] S. J. Aton, C. S. Colwell, A. J. Harmar, J. Waschek, and E. D. Herzog, “Vasoactive intestinal polypeptide mediates circadian rhythmicity and synchrony in mammalian clock neurons.,” *Nat. Neurosci.*, vol. 8, no. 4, pp. 476–83, Apr. 2005.

[34] A. Buccarello, M. Azzarito, F. Michoud, S. P. Lacour, and J. P. Kucera, "Uniaxial strain of cultured mouse and rat cardiomyocyte strands slows conduction more when its axis is parallel to impulse propagation than when it is perpendicular," *Acta Physiol.*, no. September 2017, p. e13026, 2018.

[35] R. Zeitler, P. Fromherz, and G. Zeck, "Extracellular voltage noise probes the interface between retina and silicon chip," *Appl. Phys. Lett.*, vol. 99, no. 26, p. 263702, 2011.

[36] I. R. Minev *et al.*, "Electronic dura mater for long-term multimodal neural interfaces," *Science (80-.).*, vol. 347, no. 6218, pp. 159–163, 2015.

[37] J. Bloch, S. P. Lacour, and G. Courtine, "Electronic dura mater meddling in the central nervous system," *JAMA Neurol.*, vol. 74, no. 4, pp. 470–475, 2017.

[38] "MIT Neurobiology Group." [Online]. Available: https://mcgovern.mit.edu/. [Accessed: 25-Jun-2017].

[39] N. Grossman *et al.*, "Multi-site optical excitation using ChR2 and micro-LED array.," *J. Neural Eng.*, vol. 7, no. 1, p. 16004, Feb. 2010.

[40] F. Michoud *et al.*, "Optical cuff for optogenetic control of the peripheral nervous system," *J. Neural Eng.*, vol. 15, no. 1, p. 015002, Feb. 2018.

[41] E. S. Boyden, F. Zhang, E. Bamberg, G. Nagel, and K. Deisseroth, "Millisecond-timescale, genetically targeted optical control of neural activity.," *Nat. Neurosci.*, vol. 8, no. 9, pp. 1263–8, Sep. 2005.

[42] N. Grossman *et al.*, "Photostimulator for optogenetic retinal prosthesis," *2009 4th Int. IEEE/EMBS Conf. Neural Eng.*, pp. 68–71, Apr. 2009.

[43] M. G. Shapiro, M. F. Priest, P. H. Siegel, and F. Bezanilla, "Thermal mechanisms of millimeter wave stimulation of excitable cells.," *Biophys. J.*, vol. 104, no. 12, pp. 2622–8, Jun. 2013.

[44] H. Huang, S. Delikanli, H. Zeng, D. M. Ferkey, and A. Pralle, "Remote control of ion channels and neurons through magnetic-field heating of nanoparticles," *Nat. Nanotechnol.*, vol. 5, no. 8, pp. 602–6, Aug. 2010.

[45] F. Reverter, T. Prodromakis, Y. Liu, P. Georgiou, K. Nikolic, and T. Constandinou, "Design considerations for a CMOS Lab-on-Chip microheater array to facilitate the in vitro thermal stimulation of neurons," *IEEE Int. Symp. Circuits Syst.*, pp. 630–633, Jun. 2014.

[46] M. G. Shapiro, K. Homma, S. Villarreal, C.-P. Richter, and F. Bezanilla, "Infrared light excites cells by changing their electrical capacitance.," *Nat. Commun.*, vol. 3, p. 736, Jan. 2012.

[47] R. Chen, G. Romero, M. G. Christiansen, A. Mohr, and P. Anikeeva, "Wireless magnetothermal deep brain stimulation.," *Science*, vol. 347, no. 6229, pp. 1477–80, 2015.

[48] B. McNamara, J. L. Ray, O. J. Arthurs, and S. Boniface, "Transcranial magnetic stimulation for depression and other psychiatric disorders," *Psychol. Med.*, vol. 31, no. 07, pp. 1141–1146, 2001.

[49] M. S. George, Z. Nahas, S. H. Lisanby, T. Schlaepfer, F. A. Kozel, and B. D. Greenberg, "Transcranial magnetic stimulation.," *Neurosurg. Clin. N. Am.*, vol. 14, no. 2, pp. 283–

301, Apr. 2003.

[50] J. Mäkelä, "Navigated transcranial magnetic stimulation in clinical practice and research Navigated transcranial magnetic stimulation in clinical practice and research," *Int. J. Bioelectromagn.*, vol. 17, no. December, pp. 7–12, 2015.

[51] B. L. Walter and J. L. Vitek, "Surgical treatment for Parkinson's disease.," *Lancet. Neurol.*, vol. 3, no. 12, pp. 719–28, 2004.

[52] E. B. Montgomery and J. T. Gale, "Mechanisms of action of deep brain stimulation (DBS)," *Neurosci. Biobehav. Rev.*, vol. 32, no. 3, pp. 388–407, 2008.

[53] A. Machado, H. H. Fernandez, and M. Deogaonkar, "Deep brain stimulation: What can patients expect from it?," *Cleve. Clin. J. Med.*, vol. 79, no. 2, pp. 113–120, 2012.

[54] J. L. Vitek, M. R. Delong, P. A. Starr, M. I. Hariz, and L. V. Metman, "Intraoperative neurophysiology in DBS for dystonia.," *Mov. Disord.*, vol. 26 Suppl 1, no. November 2010, pp. 35–40, 2011.

[55] J.-P. Lefaucheur, "Transcranial magnetic stimulation in the management of pain," *Suppl. Clin. Neurophysiol.*, vol. 57, pp. 737–748, Jan. 2004.

[56] and A. M. EB Plow, A Pascual-Leone, "Brain Stimulation in the Treatment of Chronic Neuropathic and Non-Cancerous Pain," *J. Pain*, vol. 13, no. 5, pp. 411–424, 2013.

[57] M. S. George *et al.*, "Daily repetitive transcranial magnetic stimulation (rTMS) improves mood in depression.," *Neurore*, vol. 6, no. Oct, pp. 1853–1856, 1995.

[58] E. M. Wassermann and T. Zimmermann, "Transcranial magnetic brain stimulation: Therapeutic promises and scientific gaps," *Pharmacol. Ther.*, vol. 133, no. 1, pp. 98–107, 2012.

[59] M. Kobayashi and A. Pascual-Leone, "Transcranial magnetic stimulation in neurology," *Lancet Neurol.*, vol. 2, no. 3, pp. 145–156, 2003.

[60] T. Wagner, A. Valero-Cabre, and A. Pascual-Leone, "Noninvasive Human Brain Stimulation," *Annu. Rev. Biomed. Eng.*, vol. 9, no. 1, pp. 527–565, 2007.

[61] J. Ruohonen, J. Virtanen, and R. J. Ilmoniemi, "Coil optimization for magnetic brain stimulation.," *Ann. Biomed. Eng.*, vol. 25, no. 5, pp. 840–849, 1997.

[62] H. Tischler *et al.*, "Mini-coil for magnetic stimulation in the behaving primate," *J. Neurosci. Methods*, vol. 194, no. 2, pp. 242–251, 2011.

[63] T. Pashut *et al.*, "Mechanisms of magnetic stimulation of central nervous system neurons.," *PLoS Comput. Biol.*, vol. 7, no. 3, p. e1002022, Mar. 2011.

[64] D. Suárez-Bagnasco, R. Armentano-Feijoo, and R. Suárez-Ántola, "The excitation functional for magnetic stimulation of fibers," *2010 Annu. Int. Conf. IEEE Eng. Med. Biol. Soc. EMBC'10*, pp. 4829–4833, 2010.

[65] P. S. Tofts, "The distribution of induced currents in magnetic stimulation of the nervous system.," *Phys. Med. Biol.*, vol. 35, pp. 1119–1128, 1990.

[66] K. Davey and C. M. Epstein, "Magnetic stimulation coil and circuit design," *IEEE Trans. Biomed. Eng.*, vol. 47, no. 11, pp. 1493–1499, 2000.

[67] S. Ueno, T. Tashiro, and K. Harada, "Localized stimulation of neural tissues in the brain

by means of a paired configuration of time-varying magnetic fields," *J. Appl. Phys.*, vol. 64, no. 10, p. 5862, 1988.

[68] B. J. Roth and P. J. Basser, "A Model of the Stimulation of a Nerve Fiber by Electromagnetic Induction A Model of the Stimulation of a Nerve Fiber by Electromagnetic Induction," vol. 37, no. 6, 1990.

[69] D. Accoto, M. T. Francomano, a. Rainer, M. Trombetta, P. M. Rossini, and E. Guglielmelli, "An implantable neural interface with electromagnetic stimulation capabilities," *Med. Hypotheses*, vol. 81, no. 2, pp. 322–327, 2013.

[70] J. Ruohonen and R. J. Ilmoniemi, "Focusing and targeting of magnetic brain stimulation using multiple coils," *Med. Biol. Eng. Comput.*, vol. 36, no. 3, pp. 297–301, 1998.

[71] J. Jeong, S. W. Lee, K. S. Min, and S. J. Kim, "A novel multilayered planar coil based on biocompatible liquid crystal polymer for chronic implantation," *Sensors Actuators A Phys.*, vol. 197, pp. 38–46, 2013.

[72] E. Basham, Zhi Yang, and Wentai Liu, "Circuit and coil design for in-vitro magnetic neural stimulation systems.," *IEEE Trans. Biomed. Circuits Syst.*, vol. 3, no. 5, pp. 321–31, Oct. 2009.

[73] T. G. Constandinou, P. Georgiou, T. Prodromakis, and C. Toumazou, "A CMOS-based lab-on-chip array for the combined magnetic stimulation and opto-chemical sensing of neural tissue," in *12th International Workshop on Cellular Nanoscale Networks and their Applications (CNNA 2010)*, 2010, pp. 1–6.

[74] D. Accoto, M. T. Francomano, a Rainer, M. Trombetta, P. M. Rossini, and E. Guglielmelli, "An implantable neural interface with electromagnetic stimulation capabilities.," *Med. Hypotheses*, vol. 81, no. 2, pp. 322–7, Aug. 2013.

[75] T. Saxena *et al.*, "The impact of chronic blood-brain barrier breach on intracortical electrode function," *Biomaterials*, vol. 34, no. 20, pp. 4703–4713, 2013.

[76] A. Canales *et al.*, "Multifunctional fibers for simultaneous optical, electrical and chemical interrogation of neural circuits in vivo," *Nat. Biotechnol.*, vol. 33, no. 3, pp. 277–284, 2015.

[77] E. T. Kim, C. Kim, S. W. Lee, J. M. Seo, H. Chun, and S. J. Kim, "Feasibility of microelectrode array (MEA) based on silicone-polyimide hybrid for retina prosthesis," *Investig. Ophthalmol. Vis. Sci.*, vol. 50, no. 9, pp. 4337–4341, 2009.

[78] S. H. Bae *et al.*, "In vitro biocompatibility of various polymer-based microelectrode arrays for retinal prosthesis," *Investig. Ophthalmol. Vis. Sci.*, vol. 53, no. 6, pp. 2653–2657, 2012.

[79] B. J. Kim, B. Chen, M. Gupta, and E. Meng, "Formation of three-dimensional Parylene C structures via thermoforming," *J. Micromechanics Microengineering*, vol. 24, no. 6, 2014.

[80] S. W. Lee, J. M. Seo, S. Ha, E. T. Kim, H. Chung, and S. J. Kim, "Development of microelectrode arrays for artificial retinal implants using liquid crystal polymers," *Investig. Ophthalmol. Vis. Sci.*, vol. 50, no. 12, pp. 5859–5866, 2009.

[81] J. Jeong, S. Shin, G. G. J. Lee, T. M. Gwon, J. H. Park, and S. J. Kim, "Advancements in fabrication process of microelectrode array for a retinal prosthesis using Liquid

Crystal Polymer (LCP)," *35th Annu. Int. Conf. IEEE EMBS*, vol. 2013, pp. 5295–8, 2013.

[82] A. Koivuniemi, S. J. Wilks, A. J. Woolley, and K. J. Otto, "Multimodal, longitudinal assessment of intracortical microstimulation," *Prog. Brain Res.*, vol. 194, pp. 131–144, Jan. 2011.

[83] V. S. Polikov, P. A. Tresco, and W. M. Reichert, "Response of brain tissue to chronically implanted neural electrodes," *J. Neurosci. Methods*, vol. 148, no. 1, pp. 1–18, 2005.

[84] S. F. Cogan, "Neural Stimulation and Recording Electrodes," *Annu. Rev. Biomed. Eng.*, vol. 10, no. 1, pp. 275–309, 2008.

[85] S. F. Cogan *et al.*, "Tissue damage thresholds during therapeutic electrical stimulation," *J. Neural Eng.*, vol. 13, no. 2, 2017.

[86] S. W. Lee and S. I. Fried, "The response of L5 pyramidal neurons of the PFC to magnetic stimulation from a micro-coil," in *IEEE Eng Med Biol Soc 2014*, 2014, pp. 6125–6128.

[87] S. W. Lee and S. I. Fried, "Magnetic Control of Cortical Pyramidal Neuron Activity Using a Micro-Coil," no. 617, pp. 22–24, 2015.

[88] S. W. Lee and S. I. Fried, "Enhanced Control of Cortical Pyramidal Neurons with Micromagnetic Stimulation," *IEEE Trans. Neural Syst. Rehabil. Eng.*, vol. 25, no. 9, pp. 1375–1386, 2017.

[89] D. K. Freeman *et al.*, "A sub-millimeter, inductively powered neural stimulator," *Front. Neurosci.*, vol. 11, no. NOV, pp. 1–12, 2017.

[90] K. Chong and Y. H. Xie, "High-performance on-chip transformers," *IEEE Electron Device Lett.*, vol. 26, no. 8, pp. 557–559, 2005.

[91] H. Jiang, Z. Li, and N. C. Tien, "Reducing Silicon-Substrate Parasitics of on-Chip Transformers," *15th IEEE Int. Conf. Micro Electro Mech. Syst.*, pp. 649–652, 2002.

[92] Y. Jeong, H. Doh, S. Jung, D. S. W. Park, and J. B. Lee, "CMOS VCO & LNA implemented by air-suspended on-chip RF MEMS LC," in *The 47th IEEE International Midwest Symposium on Circuits and Systems*, 2004, vol. 1, pp. 373–376.

[93] M. Rais-Zadeh and F. Ayazi, "Characterization of high- *Q* spiral inductors on thick insulator-on-silicon," *J. Micromechanics Microengineering*, vol. 15, no. 11, pp. 2105–2112, 2005.

[94] C. L. Chua, K. Van Schuylenbergh, J.-P. Lu, and D. K. Fork, "High-Q RF coils on silicon integrated circuits," *MEMS Components Appl. Ind. Automob. Aerospace, Commun. II,* vol. 4981, no. 650, p. 150, 2003.

[95] S. Tumanski, "Induction coil sensors-a review," *Meas. Sci. Technol.*, vol. 18, no. 3, pp. R31–R46, 2007.

[96] C. Massin *et al.*, "Planar microcoil-based microfluidic NMR probes," *J. Magn. Reson.*, vol. 164, no. 2, pp. 242–255, 2003.

[97] C. Massin, G. Boero, F. Vincent, J. Abenhaim, P.-A. Besse, and R. S. Popovic, "High-Q factor RF planar microcoils for micro-scale NMR spectroscopy," *Sensors Actuators A Phys.*, vol. 98, no. June 2001, pp. 280–288, 2002.

[98] C. R. Neagu, H. V. Jansen, A. Smith, J. G. E. Gardeniers, and M. C. Elwenspoek,

"Characterization of a planar microcoil for implantable microsystems," *Sensors Actuators A Phys.*, vol. 62, no. 1–3, pp. 599–611, 1997.

[99] Y.-M. Choi, J. J. Gorman, N. G. Dagalakis, S. H. Yang, Y. Kim, and J. M. Yoo, "A high-bandwidth electromagnetic MEMS motion stage for scanning applications," *J. Micromechanics Microengineering*, vol. 22, p. 105012, 2012.

[100] C. H. Ahn and M. G. Allen, "Micromachined planar inductors on silicon wafers for MEMS applications," *IEEE Trans. Ind. Electron.*, vol. 45, no. 6, pp. 866–876, 1998.

[101] J. Moulin, M. Woytasik, E. Martincic, E. Dufour-Gergam, U. P. Xi, and O. Cedex, "Copper planar microcoils applied to magnetic actuation," in *DTIP of MEMS & MOEMS 2007*, 2007.

[102] M. Ohnmacht, V. Seidemann, and S. Büttgenbach, "Microcoils and microrelays - an optimized multilayer fabrication process," *Sensors Actuators, A Phys.*, vol. 83, pp. 124–129, 2000.

[103] E. Haddad *et al.*, "Modeling, Fabrication, and Characterization of Planar Inductors on YIG Substrates," *Adv. Mater. Res.*, vol. 324, pp. 294–297, 2011.

[104] M. Woytasik *et al.*, "Two- and three-dimensional microcoil fabrication process for three-axis magnetic sensors on flexible substrates," *Sensors Actuators A Phys.*, vol. 132, no. 1, pp. 2–7, 2006.

[105] C. L. Chua, D. K. Fork, K. Van Schuylenbergh, and J.-P. Lu, "High-Q RF coils on silicon integrated circuits," *MEMS Components Appl. Ind. Automob. Aerospace, Commun. II*, vol. 4981, no. 650, p. 150, 2003.

[106] J. Moulin, M. Woytasik, J.-P. Grandchamp, E. Dufour-Gergam, and A. Bosseboeuf, "High current densities in copper microcoils: influence of substrate on failure mode," in *DTIP of MEMS & MOEMS 2006*, 2006, no. April.

[107] C. Gabriel, C. Gabriel, S. Gabriel, S. Gabriel, E. Corthout, and E. Corthout, "The dielectric properties of biological tissues: I. Literature survey.," *Phys. Med. Biol.*, vol. 41, no. 11, pp. 2231–49, 1996.

[108] S. Gabriel, R. W. Lau, and C. Gabriel, "The dielectric properties of biological tissues: II. Measurements in the frequency range 10 Hz to 20 GHz.," *Phys. Med. Biol.*, vol. 41, no. 11, pp. 2251–2269, 1996.

[109] S. Gabriel, R. W. Lau, and C. Gabriel, "The dielectric properties of biological tissues: III. Parametric models for the dielectric spectrum of tissues.," *Phys. Med. Biol.*, vol. 41, no. 11, pp. 2271–2293, 1996.

[110] D. Durand, A. S. Ferguson, and T. Dalbasti, "Effect of Surface Boundary on Neuronal Magnetic Stimulation," vol. 19, no. I, pp. 58–64, 1992.

[111] H. Lee, Y. Liu, R. M. Westervelt, and D. Ham, "IC/microfluidic hybrid system for magnetic manipulation of biological cells," *Solid-State Circuits, IEEE*, vol. 41, no. 6, pp. 1471–1480, 2006.

[112] H. Lee, Y. Liu, D. Ham, and R. M. Westervelt, "Integrated cell manipulation system-CMOS/microfluidic hybrid," *Lab Chip*, vol. 7, no. 3, pp. 331–7, Mar. 2007.

[113] C. S. Lee, H. Lee, and R. M. Westervelt, "Microelectromagnets for the control of magnetic nanoparticles," *Appl. Phys. Lett.*, vol. 79, no. 20, p. 3308, 2001.

[114] P. J. Maccabee, V. E. Amassian, L. P. Eberle, and R. Q. Cracco, “Magnetic coil stimulation of straight and bent amphibian and mammalian peripheral nerve in vitro: locus of excitation.,” *J. Physiol.*, vol. 460, pp. 201–19, 1993.

[115] “Autolab software.” [Online]. Available: http://www.metrohm-autolab.com/Products/Echem/Software/Software.html. [Accessed: 05-Jun-2018].

[116] Agilent Technologies, *Agilent Impedance Measurement Handbook: A guide to measurement technology and techniques*, 4th ed. USA: Agilent Technologies, 2009.

[117] W. R. Hunter, “Self-consistent solutions for allowed interconnect current density-part I: Implications for technology evolution,” *IEEE Trans. Electron Devices*, vol. 44, no. 2, pp. 304–309, 1997.

[118] P. K. Chatterjee *et al.*, “Trends for Deep Submicron,” in *Proc. IRPS*, 1995, no. Ldd, pp. 1–11.

[119] T. Y. Chiang, K. Banerjee, and K. C. Saraswat, “Analytical thermal model for multilevel VLSI interconnects incorporating via effect,” *IEEE Electron Device Lett.*, vol. 23, no. 1, pp. 31–33, 2002.

[120] S. Kilgore, C. Gaw, and H. Henry, “Electromigration of electroplated gold interconnects,” *MRS Proc.*, vol. 863, no. January, pp. 1–6, 2005.

[121] B. K. Liew, N. W. Cheung, and C. Hu, “Projecting Interconnect Electromigration Lifetime for Arbitrary Current Waveforms,” *IEEE Transactions on Electron Devices*, vol. 37, no. 5. pp. 1343–1351, 1990.

[122] S. Rzepka, K. Banerjee, E. Meusel, and C. H. C. Hu, “Characterization of self-heating in advanced VLSI interconnect\nlines based on thermal finite element simulation,” *IEEE Trans. Components, Packag. Manuf. Technol. Part A*, vol. 21, no. 3, pp. 406–411, 1998.

[123] K. Banerjee, A. Mehrotra, A. Sangiovanni-Vincentelli, and C. Hu, “On thermal effects in deep sub-micron VLSI interconnects,” in *Proceedings 1999 Design Automation Conference (Cat. No. 99CH36361)*, 1999, pp. 885–891.

[124] J. Black, “Electromigration—A brief survey and some recent results,” *Electron Devices, IEEE Trans.*, vol. 16, no. 4, pp. 338–347, 1969.

[125] A. Gangulee and F. M. d’Heurle, “The activation energy for electromigration and grain-boundary self-diffusion in gold,” *Scr. Metall.*, vol. 7, no. 10, pp. 1027–1030, Oct. 1973.

[126] N. T. Carnevale and M. L. Hines, *The NEURON Book*. New York, NY: Cambridge University Press, 2009.

[127] F. Rattay and M. Aberham, “Modeling Axon Membranes for Functional Electrical Stimulation,” *IEEE Trans. Biomed. Eng.*, vol. 40, no. 12, pp. 1201–1209, 1993.

[128] a Hodgkin and A. Huxley, “A quantitative description of membrane current and its application to conduction and excitation in nerve,” *Bull. Math. Biol.*, vol. 52, no. 1–2, pp. 25–71, 1952.

[129] D. J. Tyler, K. H. Polasek, and M. A. Schiefer, “Peripheral Nerve Interfaces,” *Nerves Nerve Inj.*, pp. 1033–1054, Jan. 2015.

[130] S. Srikantan, D. M. Durand, and E. N. Warman, “Effects of Induced Electric Fields on

Finite Neuronal Structures : A Simulation Study," vol. 40, no. 92, 1993.

[131] K. Davey, L. Luo, and D. A. Ross, "Toward Functional Magnetic Stimulation (FMS) Theory and Experiment," vol. 41, no. 11, pp. 1024–1030, 1994.

[132] K. Davey and M. Riehl, "Designing transcranial magnetic stimulation systems," *IEEE Trans. Magn.*, vol. 41, no. 3, pp. 1142–1148, Mar. 2005.

[133] T. Pashut *et al.*, "Mechanisms of Magnetic Stimulation of Central Nervous System Neurons," *PLoS Comput. Biol.*, vol. 7, no. 3, p. e1002022, 2011.

[134] S. Rangasamy, S. Olfers, B. Gerald, A. Hilbert, S. Svejda, and V. Narayanan, "Reduced neuronal size and mTOR pathway activity in the Mecp2 A140V Rett syndrome mouse model," *F1000Research*, vol. 5, no. 0, p. 2269, 2016.

[135] R. Deepthi, R. Bhargavi, K. Jagadeesh, and M. S. Vijaya, "Rheometric Studies on Agarose Gel- A Brain Mimic Material," *Sastech*, vol. 9, no. 2, pp. 27–30, 2010.

[136] C. K. Chou, G. W. Chen, a W. Guy, and K. H. Luk, "Formulas for preparing phantom muscle tissue at various radiofrequencies.," *Bioelectromagnetics*, vol. 5, no. 4, pp. 435–441, 1984.

[137] G. Hartsgrove, A. Kraszewski, and A. Surowiec, "Simulated biological materials for electromagnetic radiation absorption studies.," *Bioelectromagnetics*, vol. 8, no. 1, pp. 29–36, 1987.

[138] K. Katashima *et al.*, "In vitro assessment of factors affecting the apparent diffusion coefficient of Jurkat cells using bio-phantoms.," *Acta Med. Okayama*, vol. 67, no. 6, pp. 359–67, 2013.

[139] M. Lazebnik, E. L. Madsen, G. R. Frank, and S. C. Hagness, "Tissue-mimicking phantom materials for narrowband and ultrawideband microwave applications," *Phys. Med. Biol.*, vol. 50, no. 18, pp. 4245–4258, 2005.

[140] A. T. Mobashsher and A. M. Abbosh, "Artificial Human Phantoms : Human proxy in testing microwave apparatus that have electromagnetic interaction with the human body," *IEEE Microw. Mag.*, vol. 16, no. 6, pp. 42–62, 2015.

[141] S. Begley, "Electromagnetic properties of materials: Characterization at microwave frequencies and beyond," *Agil. Webinar*, 2010.

[142] Agilent Technologies, "Solutions for Measuring Permittivity and Permeability with LCR Meters and Impedance Analyzers," 2014.

[143] B. Gustafsson and E. Jankowska, "Direct and indirect activation of nerve cells by electrical pulses applied extracellularly.," *J. Physiol.*, vol. 258, no. 1, pp. 33–61, 1976.

[144] H. Lee, A. M. Purdon, V. Chu, and R. M. Westervelt, "Controlled Assembly of Magnetic Nanoparticles from Magnetotactic Bacteria Using Microelectromagnets Arrays," *Nano Lett.*, vol. 4, no. 5, pp. 995–998, May 2004.

[145] E. Neher and B. Sakmann, "Single-channel currents recorded from membrane of denervated frog muscle fibres," *Nature*, vol. 260, no. 5554, pp. 799–802, 1976.

[146] E. Neher and A. Marty, "Discrete changes of cell membrane capacitance observed under conditions of enhanced secretion in bovine adrenal chromaffin cells.," *Proc. Natl. Acad. Sci.*, vol. 79, no. 21, pp. 6712–6716, 1982.

[147] A. Vaziri and M. B. Plenio, "Quantum coherence in ion channels: Resonances, transport and verification," *New J. Phys.*, vol. 12, pp. 0–18, 2010.

[148] C. Molecular Devices Corporation, 3280 Whipple Road, Union City, "The Axon CNS Guide: The Axon CNS Guide to Electrophysiology & Biophysics Laboratory Techniques," no. Second edition, p. 298, 2006.

[149] M. Maschietto, S. Girardi, M. Dal Maschio, M. Scorzeto, and S. Vassanelli, "Sodium channel β2 subunit promotes filopodia-like processes and expansion of the dendritic tree in developing rat hippocampal neurons," *Front. Cell. Neurosci.*, vol. 7, no. January, 2013.

[150] C. G. Dotti, C. a Sullivan, and G. a Banker, "The establishment of polarity by hippocampal neurons in culture.," *J. Neurosci.*, vol. 8, no. 4, pp. 1454–1468, 1988.

[151] M. E. Rizou and T. Prodromakis, "A planar micro-magnetic platform for stimulation of neural cells in vitro," *Proc. - 2016 IEEE Biomed. Circuits Syst. Conf. BioCAS 2016*, pp. 34–37, 2017.

[152] M. E. Rizou and T. Prodromakis, "Magnetic stimulation in the microscale: the development of a 6x6 array of micro-coils for stimulation of excitable cells in vitro," *Biomed. Phys. Eng. Express*, vol. 2, 2017.

[153] "Dielectric properties of grey and white matter." [Online]. Available: http://niremf.ifac.cnr.it/docs/DIELECTRIC/home.html. [Accessed: 05-Jun-2018].

[154] I. Marei, A. Chester, I. Carubelli, T. Prodromakis, T. Trantidou, and M. H. Yacoub, "Assessment of Parylene C Thin Films for Heart Valve Tissue Engineering," *Tissue Eng. Part A*, vol. 21, no. 19–20, pp. 2504–2514, 2015.

[155] T. Trantidou, E. J. Humphrey, C. Poulet, J. Gorelik, T. Prodromakis, and C. M. Terracciano, "Surface Chemistry and Microtopography of Parylene C Films Control the Morphology and Microtubule Density of Cardiac Myocytes," *Tissue Eng. Part C Methods*, vol. 22, no. 5, pp. 464–472, 2016.